UNIVERSITY OF CALIFORNIA SAN DIEGO

Investigating and exploring acoustofludics in Li batteries and beyond

A dissertation submitted in partial satisfaction of the
requirements for the degree
Doctor of Philosophy

in

Materials Science and Engineering

by

An Huang

Committee in charge:

Professor James Friend, Chair
Professor Prabhakar Bandaru
Professor Ping Liu
Professor Yu-Hwa Lo
Professor Sheng Xu

2020

The dissertation of An Huang is approved, and it is acceptable in quality and form for publication on microfilm and electronically:

_____

_____

_____

_____

_____
Chair

University of California San Diego

2020

DEDICATION

To my parents: Ying-che Huang and Li-ju Liu, Dr. Rey-der Lou and Ming-hsiang Chiu.

To my supportive and loving husband, Dr. Cheng-kai Luo.

TABLE OF CONTENTS

LIST OF FIGURES

LIST OF TABLES

ACKNOWLEDGEMENTS

First of all, I would like to express my sincere gratitude to my principle investigator, Prof. James Friend, for his continued guidance, supports, discussions, and motivations. I am sincerely honored to have the opportunity to work with him. I could not have imagined having a better advisor and mentor for my Ph.D study.

Moreover, I would like to express my appreciation to my dissertation committee members, Prof. Ping Liu, Prof. Bandaru Parbhakar, Prof. Yu-Hwa Luo, and Prof. Sheng Xu for their precious time and guidance.

Moreover, I would like to acknowledge my collaborators and co-authors in UC San Diego. Dr. Haodong Liu, Dr. Amihai Horesh, Dr. Oscar Mena, Shuai Zheng, Gopesh Tilvawala, Jiaying Wang, William Connacher, Naiqing Zhang, and Jiyang Mei for the fruitful discussions and brainstorming on problem-solving. I am also thankful to all of my lab mates, visiting scholars, and visiting professors from Medically Advanced Device Laboratory (MADLab) for the useful discussions.

Furthermore, I would like to extend my thankful to my collaborators, Prof. Mikhail Shapiro, and Dr. Avinoam Bar-Zion from Caltech, Dr. Vincent Leung, Mr. Mark Stambaugh, Sravya Alluri, Aditi Jain from Qualcommn institute, Dr. Ofer Manor from Technion, Dr. Phillip Kyriakakis from UCSD Bioengineering, Anushi E Rajapaksa from Royal Children's Hospital for their valuable discussions and inputs to the projects.

My sincere thanks also goes to Prof. Vish Krishnan and Prof. Amy Nguyen-Chyung from UCSD Rady school, who led me into the mini-MBA and Lab to Market courses as

well as guiding me to explore into Entrepreneurship.

I would like to acknowledge the financial supports from Energy Efficiency and Renewable Energy, Office of Vehicle Technologies of the U.S. Department of Energy (DE-EE0008363), funding from UCSD Office of Innovation and Commercialization, and institute for the global entrepreneur to support me throughout the Ph.D study.

For the last but not least, my deepest gratitude goes to my parents Ying-che Huang, Li-ju Liu, Rey-der Lou, and Ming-hsiang Chiu for their never-ending support. I specially thank to my husband, Cheng-kai Luo, for his endless love, support and encouragement during my Ph.D.

Chapter 2, in part, is a reprint of materials appears in Lab on Chip 2018. Connacher, William, Zhang, Naiqing; Huang, An; Mei, Jiyang; Zhang, Shuai; Gopesh, Tilvawala; Friend, James. The dissertation author was the co-primary investigator and author of this paper.

Chapter 4, in full, is a reprint of material appears in Advanced Materials 2020. Huang, An; Liu, Haodong; Manor, Ofer; Liu, Ping, Friend, James., Advanced Materials 2020. The dissertation author was the primary investigator and author of this paper.

Chapter 5, in part, is a reprint of material that is in preparation for submission 2020. Huang, An; Liu, Haodong; Liu, Ping, Friend, James. The dissertation author was the primary investigator and author of this paper.

Chapter 6, in part, is a reprint of material that is in preparation for submission 2020. Huang, An; Connacher, William; Stamburg, Mark; Zhang, Shuai; Zhang, Naiqing; Mei, Jiyang; Jian, Aditi; Alluri, Sravya; Leung, Vincent; Rajapaksa, Anushi; Friend, James.

The dissertation author was the co-primary investigator and author of this paper.

Chapter 7 in full, is a reprint of material appears in Applied Physics Letters 2018. Huang, An; Miansari, Morteza; Friend, James., Applied Physics Letters 2018. The dissertation author was the primary investigator and author of this paper.

Chapter 8 in full, is a reprint of material appears in Advanced Functional Materials 2020. Zhang, Shuai; Huang, An; Bar-Zion, Avinoam; Wang, Jiaying; Mena, Oscar; Shapiro, Mikhail; Friend, James., Advanced Functional Materials 2020. The dissertation author was the primary investigator and author of this paper.

VITA

2007-2012	B. S. in Materials Science and Engineering, Tatung university
2013-2014	M. S. in Materials Science and Engineering, University of California San Diego
2015-2020	Ph. D. in Materials Science and Engineering, University of California San Diego

PUBLICATIONS

A. Huang, H. Liu, O. Manor, P. Liu, and J. Friend "Lithium-Metal Batteries: Enabling Rapid Charging Lithium Metal Batteries via Surface Acoustic Wave-Driven Electrolyte Flow", Advanced Materials, 2020, 32, 2070108.

S. Zhang*, A. Huang*, A. Bar-Zion, J. Wang, O. Vazquez Mena, M. Shapiro, J. Friend, "The Vibration Behavior of Sub-Micrometer Gas Vesicles in Response to Acoustic Excitation Determined via Laser Doppler Vibrometry", Advanced functional Materials", 2020, 30, 200239. (* equilly contributed first authors)

W. Connacher, N. Zhang, A. Huang, J. Mei, S. Zhang, T. Gopesh, J. Friend, "Micro/nano acoustofluidics: materials, phenomena, design, devices, and applications" Lab on Chip, 2018, 18, 1952.

A. Huang, M. Miansari, J. Friend, "Driving useful morphological changes in magnetic nanoparticle structures through the application of acoustic waves and magnetic fields" Applied Physics Letters, 2020, 113, 034103.

A. Huang, W. Connacher, M. Stambaugh, N. Zhang, S. Zhang, J. Mei, A. Jain, S. Alluri, V. Leung, A. E Rajapaksa,and James Friend "Practical Microcircuits for Handheld Acoustofluidics", under review.

J. Friend, A. Huang, P. Liu, H. Liu, "Chemistry Agnostic Prevention of Ion Depletion and Dendrite Formation in a Liquid Electrolyte", US Patent field 62/882,450.

J. Friend and A. Huang "Acoustic wave based dendrite prevention for rechargeable batteries", US patent 16331741.

A. Huang, H. Liu, P. Liu, J. Friend "Enabling Fast Charging Lithium Ion Battery with Surface Acoustic Wave Device", IEEE IUS (2020) , Las Vegas

A. Huang, H. Liu, P. Liu, J. Friend, "Enabling rapid charging lithium-metal based rechargeable batteries through suppression of dendrite growth and ion depletion in the electrolyte via surface acoustic wave-driven mixing", Materials Research Society (2019), Boston, USA.

S. Zhang , A. Huang, A. Bar-Zion, J. Wang, O. Vazquez Mena, M. Shapiro, J. Friend, "The Vibration Behavior of Submicron Gas Vesicles in Response to Acoustic Excitation as Determined via Laser Doppler Vibrometry", Materials Research Society (2019), Boston, USA.

A. Huang, H. Liu, P. Liu, J. Friend, "Rapid charging made practical in lithium batteries via integrated surface acoustic wave turbulent electrolyte mixing to overcome diffusion-limoted charging", Advanced Automotive Battery Conference (2018), San Diego, USA.

A. Huang, H. Liu, P. Liu, J. Friend "Prevent lithium dendrite formation in rechargeable batteries through surface acoustic waves", IEEE International Ultrasonics Symposium (2017), Washiongton DC, USA.

A. Huang, M. Miansari, J. Friend, "Driving morphological changes in magnetic nanoparticle structures through the application of acoustic waves and magnetic fields", Applied Physics Society meeting (2016), New Orleans, USA.

A. Huang, M. Miansari, J. Friend "Fast dimensional transition of magnetite nanoparticles self-assembly through external magnetic force and surface acoustic wave", Acoustofludics Meeting (2016), Copenhagen, Denmark.

ABSTRACT OF THE DISSERTATION

Investigating and exploring acoustofludics in Li batteries and beyond

by

An Huang

Doctor of Philosophy in Materials Science and Engineering

University of California San Diego, 2020

Professor James Friend, Chair

Surface acoustic wave devices (SAW) offer extraordinary power density to efficient manipulate the fluid motion surround it. The SAW generated from the piezoelectric lithium niobate substrate is transmitted into the liquid as an intense sound beam that is progressively attenuated by the fluid's viscosity as it propagates. This attenuation is not lost, rather, it gives rise to a flux in the fluid's momentum in a narrow (100μm) sound beam along the direction of the sound propagation. The sound propagates at an angle from the substrates, called Rayleigh angle, that is dependent on the characteristics of the fluid and

the piezoelectric substrate. The fluid momentum grows as the sound attenuates, causing fluid transport, called acoustic streaming. Uniquely, they generate locally extreme accelerations of 10^8 to 10^{10} m/s^2, driving acoustic streaming-driven fluid flow up to 1 m/s, and imparting acoustic forces upon objects present in the fluid down to the micro or nano sized scales.

On the other hand, the major drawback of lithium batteries is its diffusion limitation, which limits its power density and energy density. However, both of the parameters are critical for the success of battery applications, especially with the ever growing demands for the electronic devices and electric vehicles: the current high energy batteries with graphite anodes and metal oxides cathodes are unable to achieve the fast charge goals without adversely impact the performance and safety of a battery. A novel mechanical approach oppose to the traditional chemical approaches is therefore required to fundamentally enhance the properties inside a battery.

In my PhD dissertation, the major focus is to integrate a SAW into a Li battery based on the assumption of the acoustic streaming fluid can enhance the Li^+ ions diffusion rates and further improve the battery performances, especially its energy density at high charge rates, cycle life, and safety. The dissertation starts with the design with consideration of the theories from both acoustofludics and electrochemistry, to the analysis of cell performances and electrodes degradation analysis. A closed form mathematical model were proposed to describe the phenomenon.

Furthermore, I also explored the applications of SAW into different areas. The self-assembled magnetic particles was achieved by the balanced forces between magnetic forces

and acoustic force was introduced. Moreover, the vibration behaviour of sub-micron sized gas vesicles under the acoustic vibration was investigated, giving insights to harmonic responses and non-linear buckling behaviours.

Chapter 1

Motivation and Dissertation outline

The Nobel Prize in Chemistry 2019 was awarded to John Goodenough, Stanley Whittingham, and Akira Yoshino for the development of lithium ion batteries (LIB). This has, according to the judges, "created an ideal condition towards the wireless and fossil fuel-free society" [10]. Following the invention and developments in the LIB space, we have a powerful, lightweight and rechargeable battery that is used in an ubiquitous manner. These developments have revolutionized the battery space, by increasing storage from sources such as solar and wind power, making this "the greatest benefit to humankind" [10]. The growing rechargeable battery industry is influenced by the three key factors that characterize in today's cities: population growth, city growth, and increased drive for green solutions.

It is shown that almost a third of the greenhouse emission comes from transportation, generating around 2000 Million Metric Tons of CO_2 equivalent every year [11, 12]. Even though the full electric vehicles concept has grown rapidly in the recent years, the gasoline

car is still dominant 90% of the car market in the USA [13]. The range anxiety still remains a barrier for purchase, as the biggest fear from a customer is to become stranded without power. The range anxiety is a combination of two aspects: driving distance and the recharge time. And therefore this drives the researchers and even Department of Energy to release a new program in 2018 to stimulate the development in both of the directions.

Lithium ion battery, one of the most popular battery chemistry, demonstrating great potential in accomplishing those aspects given by its intrinsic material properties. The major feature of lithium (Li) are: Li is the most lightweighted material and has the lowest redox potential (-3.04V versus the standard hydrogen electrode) [5]. Those features resulting into a battery with high voltage and high energy density. Recently, LIB has became the major power source for many electronic applications, from consumer electronics to electric vechiles, and to grid storage system. The major bottleneck of the lithium battery is the trade-off features of a battery between energy density, charge rate, cycle life, and cost. For example, energy density is a trade-off of charge rate; while cycle life is also another trade-off of charge rate; and the cost reduction may be a trade-off of energy density. And therefore, there is no such a battery that can accommodate all the important parameters together. One of the major reasons that attribute to the trade-off phenomenon is the diffusion limits of ions in a battery. To mitigate the diffusion limitation issues, most of the researches are focusing on chemical approaches. However, the progress is slow to meet the need from the market [14].

Surface acoustic wave (SAW) driven acoustic streaming is another topic that relates to adapting acoustic pressure to enhance the liquid transportation speed and increase

particles diffusion rates, especially in microfludics and nanofludics area [15]. It is shown that the particle acceleration can be as large as 10^8 ms^{-2} in a acoustofludics system. The large acceleration attributes to the enhancement of diffusion coefficient of the ions or particles in a fluids system. It is shown that the diffusion coefficient can be increased by two orders of the magnitude with the presence of the acoustic streaming, which greatly increase the mixing efficiency and decrease the required time for an application [16].

My Ph.D dissertation focuses on integrating a SAW device with a Li battery to overcome the diffusion limitation issues that originates from a traditional battery to enable a high energy density and high power density Li battery. The approach starts with exploring the idea with a single layered LMB with the integration of a SAW device. And the concept was extended to a multilayered LIB with a SAW device integrated. Furthermore, we developed a circuit to enable the cycling of the SAW integrate Li battery. This efforts was further found to be a solution to a long-standing acoustofludics field's problem: a "true" handheld circuit to enable the lab-on-chip concept. The later part of the dissertation branches out to the exploration of integrating SAW to another applications. It includes integrating SAW with magnetic force to induce magnetic particle self-assembly from 0-D particles to 2-D films, providing a practical, time-effective, and low cost solution for achieving a stable 2-D magnetic film. Further, we explored adopting acoustic energy and laser Doppler vibrometer to observe the vibration behaviour of the sub-micron sized gas vesicles. With the success understanding of the vibration behaviour of the gas vesicles, this provides an insight to the medical field to adopt them more effectively.

My Ph.D dissertation consists of nine chapters. **Chapter 1** discussed the problem

and the motivation of the proposed dissertation. **Chapter 2** gives a general introduction of the acoustofludics discipline, from piezoelectric materials to their applications in the acoustofludics fields. **Chapter 3** introduced Li batteries (Li metal battery and Li ion batteries), from battery components to their working mechanisms and the limitation of a Li battery. **Chapter 4** discussed the surface acoustic wave interacts with a single layered Li-metal battery. This chapter starts with the battery design, to the performance analysis, and ends with a closed-form mathematics model. **Chapter 5** further discussed the acoustic energy interaction to a multilayered Li-ion battery, the chapter focus on battery performance analysis and the post cycled battery analysis from imaging tools to neutron diffraction analysis. **Chapter 6** provides an engineering solution to enable a handheld circuit for the operation of a SAW integrate Li battery. The portable circuit was later found to have a significant impact to the acoustofludics field. The chapter starts with the design considerations to the performance comparison of using handheld circuit to the bench-top equipment with common acoustofludics applications. **Chapter 7** discussed an application that adapts the surface acoustic wave with the external magnetic forces to generate the dimensional change of 0-D magnetic particles to stable 2-D magnetic films. **Chapter 8** explored using acoustic wave to vibrate the submicron sized gas vesicles to observe their vibration behaviour and the non-linear buckling effects. Finally, the dissertation close at **Chapter 9**. This chapter summarize the dissertation and the future works.

Chapter 2

Acousotfludics

2.1 Microscale Acoustofluidics

Microfludics is a science and technology that provides a means to scale down chemical or biomedical analysis with both equipment size and time requirement for a chemical reaction or for a diagnosis device [17]. Generally speaking, it is an application of applying fluid physics at small scales with the size of the channels that are less than 1 mm and the quantity of the fluid are less than 1 mL [16]. The technology utilized special equipment to precise control small-scale fluids into a pre-designed channels, which fits into the targeted applications. The channels are craved in a polymer-based material that can resist the volume change due to water, clean edges to prevent particle agglomeration, and transparent for observation. The whole channel on the material is called a "chip", and the lab-on-chip concept is therefore called [18].

As the fluid dimensions shrinks down to microscales, their specific surface area is there-

fore increases [19]. In the microfludics application, three fluid phenomena are generated. The first phenomenon associates with mass and heat transfer, becoming more efficient than at the macroscale length due to the diffusion length scale is much smaller. Second of all, the fluid physics is dominate by viscosity and surface tension. Third, the surface effects become more significant as the specific surface area is increased.

The fluid flows is close to laminar flow without external actuation, fluids or particles mixing happens only due to the diffusion [20]. Diffusion is defined as the process of mixing molecules from a high concentration region to low concentration region through Brownian motion, result into a gradual mixing of a material. The diffusion coefficient (D) is defined mathematically by Fick's law: $j = -D\frac{d\varphi}{dx}$, where φ is the species concentration and x is the position of the species [21]. Moreover, the diffusion coefficient (D) can be derived from Einstein-Stokes equation: $D = \frac{kT}{6\pi\mu r}$, where k is Boltzmann constant, T is the absolute temperature, r is the radius of the particles, and μ is the viscosity of the medium. It is found that the diffusion coefficient for small molecules at room temperature is 10^{-8} to 10^{-9} $\mathrm{m^2 s^{-1}}$ [22].

However, the diffusion-based reactions are usually too slow for the real applications even though the diffusion distance is already smaller than the benchtop containers: $x^2 = 2Dt$, where t is the time for the particles to diffuse over a distance x [23]. And therefore, it is necessary to speed up the mixing efficiency. To generate effective mixing of the fluids, there are usually two methods to approach: passive mixers and active mixers [24, 25]. Passive mixers, where mixing is a result of fluid being passing through an architecture in the channel [26]. The architecture introduce chaotic advection or creates laminar shear

to induce fluid flow. One of the drawback is a relatively long channel length (>1 cm) is needed to lead the flow to reach a chaotic state [26].

On the other hand, active mixers rely on an external energy source to achieve mixing, such as magnetic [25] and acoustic force [27]. It is shown that the mixing efficiency is better than the passive case. Among the active mixers, one of an interesting approaches for active mixers is to adapt high-frequency acoustic wave to drive fluid flow through acoustic streaming [27]. The streaming comes from the second order fluid effect by the Reynolds stress, introduced from Navier-stoke equation, exerting in an attenuating sound beam, a pressure field that can generate fluid flow [16]. The Navier-Stokes equation, describing the relationship between the momentum flux, viscosity of the fluid, and forces that generated by pressure and is expressed as Eq. 2.1

$$\rho(\frac{\partial u}{\partial t} + u \cdot \nabla u) = -\nabla p + \mu(\nabla)^2 u + +(\frac{1}{3}\mu + \mu_b)\nabla(\nabla \cdot u) + f \tag{2.1}$$

where p is the hydrostatic pressure, μ is the shear viscosity, μ_b is the bulk or dilatational viscosity, f is the body forces, ρ is the density of the fluid, u is the fluid velocity. It is worth to mention that the $\rho(u \cdot \nabla)u$ is related to the Reynolds stress and is responsible for the acoustic streaming [16] that will be discussed in the later section .

Piezoelectric transducer is one of the source to generate sound wave. The piezoelectric effect allows the electric energy to convert into mechanical stress due to the piezoelectric material become electrically polarized during mechanical deformation [28]. Ultrasound transducers is one of the examples and have been used to manipulate particles, cells,

tissues in a liquid media. Moreover, lead zirconate titanate (PZT) disk [29], which is a polycrystalline ceramic piezoelectric transducer, has been used widely. PZT disk is a dynamic oscillator, its resonant modes is determined by its material property and geometry, especially to the thickness of the piezoelectric material, which is inverse proportional to the resonance frequency. Ideally, a PZT is operated as a uniform piston with more mode shapes and at higher harmonics, generating a more complex velocity distribution [30]. However, PZT is toxic [31], has significant excess lead oxide present along the grain boundaries [32], and facing regulations to eliminate from using. The efforts have been shown in eliminating lead while retaining good performance from polycrystalline ceramics, potassium sodium niobate (KNN) is one of the examples [33]. However, the granular nature of polycrystalline piezoelectrics limits their use to relatively low frequencies (1 kHz to 1 MHz) due to the finite size of the grains and domains within the material that strongly interact with the generation and propagation of acoustic waves at greater frequencies to generate heat [34].

To generate high frequency acoustic device while considering clean element and power efficiency at the same time, research has been tailored toward the piezoelectric material exploration and synthesis. Quartz [35], lithium tantalate (LT, $LiTaO_3$) [36] and lithium niobate (LN, $LiNbO_3$) [16], gallium arsenide (GaAs) [37], cadmium sulfide (CdS) [38], zinc oxide (ZnO) [39], annd lithium tetraborate ($Li_2B_4O_7$) [40] has been shown to generate surface acoustic wave to at least 100 MHz. The first SAW generation was demonstrated by White and Voltmer [35], adopting spatially periodic thin-film metal electrodes on a piezoelectric Y-cut, Z-propagating quartz substrate. This method is still dominate for today's electronic industry for signal processing at the frequency range from 10 MHz to 1 GHz

[41]. However, the coupling coefficient of quartz is low (0.2885 at Y-rotated Z-propagate direction quartz) for the application that requires to have surface travelling wave [35]. And therefore, it is required to improve the coupling coefficient for better SAW generation. It is found that the 131 ° Y-rotated X-propagate lithium niobite ($LiNbO_3$, LN) wafer shows the highest electromechanical coupling coefficient and lowest insertion loss [42, 43]. However, with the generation of the parasitic bulk wave, reducing its energy efficiency. The common bulk waves include leaky SAW (LSAW), love waves, Bleustein–Gulyaev waves, surface skimming bulk waves (SSBW), and surface transverse wave (STW) are generally categorized as psedo-SAW (PSAW) and are inefficient for the acoustofluidics application, mainly due to power efficiency and clean surface wave generation [44, 44].

It is later than found that the 127.86° Y-rotated X-propagate LN is the optimal for Rayleigh SAW generation as after careful design, it eliminates the bulk wave [45]. The pure SAW or Rayleigh SAW are confined within three to four wavelength from the surface of a piezoelectric material. Other cuts of LN have even higher electromechanical coupling coefficients, such as 36°, 41°, and 64° Y-rotated cuts [46, 47], but these produce spurious modes and beam steering that preclude them from applications requiring clean surface travelling wave. The electromechanical coupling coefficient is defined as $K^2 = 2\Delta$ v/v $= 2(v_f - v_m)/v_f$, where v_f is the wave velocity in the free substrate and v_m is the wave velocity measured along a short-circuited plane [48].

2.2 Electrode design

Most acoustofluidic devices use either thickness mode transducers or SAW devices that are photolithographically patterned the thin-film metal on the surface of a LN. One of the important design consideration is the thickness of the substrate as it determines the minimum frequency of the SAW. Most suppliers provide 500 μm thick wafers, limiting on the frequency suitable to form true Rayleigh SAW of about 40 MHz due to the wavelength of true SAW is within five wavelengths from the surface. Using frequencies below this value can cause the acoustic wave to penetrate all the way through the substrate to the other side forming, alongside Rayleigh SAW, spurious Lamb waves that can shed energy through the back side of the substrate into its mounting and affecting the wave propagation and device performance [49]. This phenomenon has been shown in the lab environment of strong fluid transport in 20 MHz shear-horizontal SAW (SH-SAW) devices that should show no fluid transport at all. Second is the electrode design.

The first and simplest IDTs [35] consisted of straight rectangular metal bars—referred to as fingers—deposited onto the surface of a piezoelectirc substrate, which were alternately connected on either end by bus bars as pictured in Figure 2.1. This structure creates an array of electric fields at alternating direction between the transducer finger pairs that in turn create alternating regions of compression and tension in the substrate. Each finger pair thus produces displacement in the substrate that oscillates with the electric field and radiates a SAW [35]. The periodicity of the finger pairs defines the wavelength of the resulting SAW (λ_{SAW}) such that distance from one finger to the next is $\lambda_{\mathrm{SAW}}/4$.

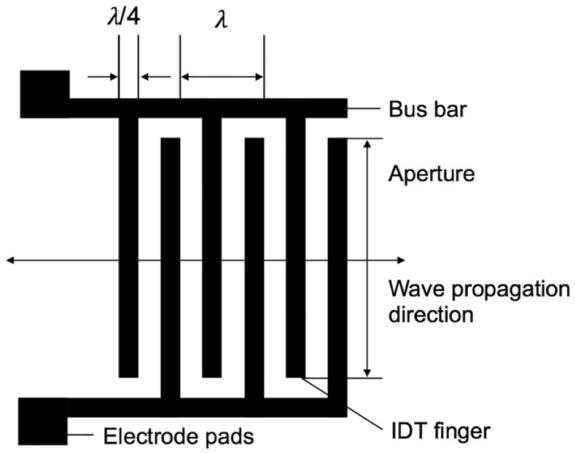

Figure 2.1: A SAW device consisting of comb-like interdigital transducers (IDT fingers), bus bars, and electrode pads on a piezoelectric substrate. The resulting traveling wave propagates as shown, which can be observed using a laser Doppler vibrometer.

The relationship of wavelength to the substrate properties can be defined as: $\lambda_{\text{SAW}} = \frac{2\pi V_R}{\omega}$, where $\omega/2\pi$ is the operation frequency, and V_R is the surface wave velocity, greatly depending on the material properties of the substrate, the propagation direction, and the thickness of the IDT [46]. For example, λ_{SAW} for 128 Y-roated X-propagate LN is 3992 m/s, while it is 3158 m/s for a ST-quartz [46].

On the other hand, the film thickness ratio, defined as h/λ_{SAW}, where h is the metalization thickness is commonly made to be less than 1% in order to reduce reflection of the SAWs from the IDT fingers [50, 51]. The relationship between the feature size (corresponding to finger periodicity) and the V_R implies that for a given feature size there is an optimal frequency which ensures constructive interference across the IDT. This corresponds to the resonant frequency of a SAW device, where the power density and surface displacement are maximized [52, 35]. As the SAW propagates through subsequent finger pairs, the wave is diffracted, creating a near-field region of largely parallel wavefronts known as the Fresnel

region. The far-field region, where SAW is broadly diffracted along major and minor lobes, is known as the Fraunhofer region. In order to minimize diffraction losses, the aperture of the IDT must be contained within the Fresnel region [53].

For design purposes, the Fresnel parameter (F) is defined [54]:

$$F = \frac{4\lambda_{SAW} D_F}{a^2} \tag{2.2}$$

where a is the aperture width and D_F is the distance from the IDT edge. To remain within the Fresnel region, the aperture should be selected such that $F < 1$ [15].

The efficiency of a SAW device is commonly linked to its quality factor (Q), which is defined as $Q = f_c/\triangle f$, where $\triangle f$ is the width of the resonant peak (measured via a laser Doppler vibrometer or a network analyzer). The quality factor is influenced by dielectric losses of the piezoelectric materials,loading effects, ohmic losses, and acoustic leakage to the substrate. Experimentally, the quality factor of a SAW device is around 3 dB [46, 51].

The number of finger pairs (N_p) of a SAW device is an important parameter partially due to it affects the quality factor [55]. The optimization of N_p is dependent on the coupling coefficient of the substrate ($v/2\triangle v$) and the arrangement of the IDT fingers. SAW amplitude increases with N_p up to a material dependent limit, but the bandwidth is reduced. Optimization of N_p is a complex procedure that is important in signal processing applications, but, when the primary concern is power, only practical limits are placed on N_p. For example, the bandwidth must be broad enough to berecognized by signal generation and frequency response analysis equipment. Optimization begins by defining

the electrical admittance ($Yt(\omega)$) of the IDT, which is dominated by capacitance (C_t) , conductance ($G_a(\omega)$), and susceptance ($B(\omega)$) as in Eq. 2.3.

$$Y_t(\omega) = G_a(\omega) + jB(\omega) + j(\omega)C_t \tag{2.3}$$

The RLC equivalent circuit therefore consists of three components in parallel. When a voltage (V) is applied to the transducer, the power (P_a) that is absorbed and produced are defined respectively as:

$$P_a = \frac{1}{2}G_a V^2 \tag{2.4}$$

$$P_s = \frac{1}{4}\omega\epsilon_\infty W N_p^2 \left(\frac{\triangle v}{v}\right)\left(\frac{sin(x)}{x}\right)^2 \tag{2.5}$$

where ϵ_∞ is the capacitance per period of a unit-aperture, single electrode transducer, which is dependent on the substrate. At a certain frequency, susceptance becomes negative and begins to counteract the capacitive term. When these terms cancel out, the admittance becomes real and directly corresponds to a resistive load. This occurs when the following equations are satisfied: $N_p = v\pi Q_t/2\triangle v$ and $\triangle f/f_c = 1/N_p$. Therefore, N_p=21 for a single electrode IDT with a bandwidth of 0.05, while $N_p = 26$ for the double electrode IDT with a bandwidth of 0.038 in 128° YX LN.

Other common IDT designs for the SAW device, such as slanted IDT, which generate a wide-band response filter. The maximum angle that can be achieved depends on the coupling coefficient of the substrate. For example, the limit for a Y-rotated Z-propagated

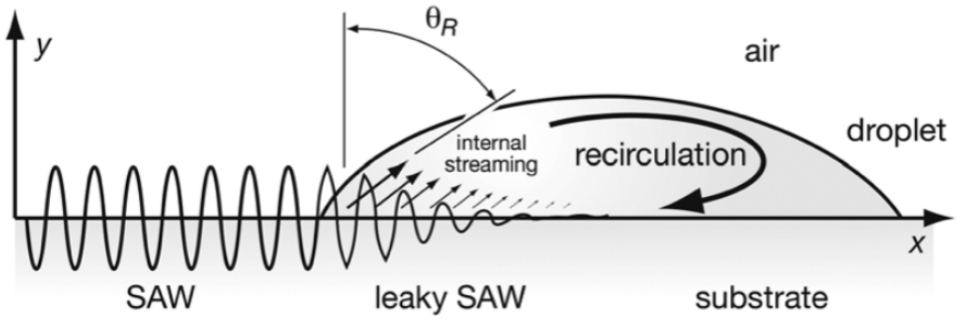

Figure 2.2: Sketch of a SAW acting on a small sessile drop. The acoustic energy is diffracted into the fluid at the Rayleigh angle, θ_R, leading to internal streaming in the small fluid volume, which drives recirculation. Reprinted from Li. et al. [1]

LN substrate is 7° due to beam steering losses [18]. Chirp IDT, has linear gradient in finger spacing that allows it to resonant at a wide range of frequencies, allowing the excitation of SAWs at different wavelengths by tuning the input signal [56]. One port or two ports resonator design, on the other hand, provide a integrate reflectors that can allocate the acoustic wave into one direction [57]. Focused IDT, results into SAW with higher intensity by laterally focusing the SAW energy towards the main axis of the IDT [58].

2.3 Acoustic wave travelling in liquid

Surface acoustic waves propagate upon single crystal piezoelectric substrates with weak attenuation at nanometer scale. Upon encountering a fluid on the surface, SAW leaks into the fluid, forming sound that propagates in the fluid and attenuate the SAW in the substrate (see Fig. 2.2). The mechanism of the acoustic energy attenuation is balanced by viscous attenuation and dilatative dissipation. This can be described in Eq. 2.6.

$$\frac{\partial W}{\partial t} + \cdot\Delta J = \rho_\circ v_\circ [b u_\circ \cdot \Delta u_\circ - u_\circ \cdot \Delta \times u_\circ] \tag{2.6}$$

where W is the acoustic energy density, J is the energy flow, $\Delta \times \Delta \times u_\circ$ describes the viscous attenuation, and $u_\circ \cdot u_\circ$ describes the dilatative dissipation.

SAWs leak radiation into the fluid inducing an acoustic pressure gradient change in the fluid system, which further leads to acoustic streaming [15]. The resulting longitude wave—referred to as leaky-SAW—travels through the liquid at the Rayleigh angle θ_R, which is defined as $\theta_R = sin^{-1}(v_l/v_s)$, where v_l and v_s represent the speed of sound in the liquid and solid, respectively. This phenomena is analogous to Snell's law for light and so the acoustic wave is said to refract into the fluid due to a change in acoustic impedance. For example, $\theta_R = 23°$ for the case of SAWs traveling from 128° Y-rotated X-propagate LN to water [59].

The length over which a Rayleigh wave decays by a factor of e due to the emission of leaky-SAW into the fluid is called its attenuation length, α^{-1} and is expressed as Eq. 2.7 [59]:

$$\alpha^{-1} = \frac{\rho_f c}{\rho_s V_R \lambda_{\mathrm{SAW}}} \tag{2.7}$$

where ρ_f and ρ_s are the densities of the fluid and the solid respectively, c is the speed of sound in the fluid media, $V_R = \lambda_{\mathrm{SAW}}\omega/2\pi$ is the Rayleigh wave phase velocity and λ_{SAW} is the SAW wavelength. The sound wave in the fluid, on the other hand, propagates

uniaxially at the Rayleigh angle [60]. The decay length of the sound in the fluid is β^{-1},

$$\beta^{-1} = \frac{\rho_f c^3}{4\pi^2 f_{\mathrm{SAW}}^2 \left(\frac{4}{3}\mu + \mu'\right)} \tag{2.8}$$

where f_{SAW} is the SAW frequency and μ and μ' are the shear and bulk viscosities of the fluid, respectively. Values of the attenuation length in the LN-water system were measured by Dentry *et al.* [52] and are listed in Table 2.3.

Table 2.1: Attenuation length of the SAW surface displacement at the LN-water interface, α^{-1} [Eq. 2.7], attenuation length of the sound in deionized water, β^{-1} [Eq. 2.8]

f_{SAW}(MHz)	α^{-1}(mm)	β^{-1} (mm)
19.7	2.4	120
54.2	0.87	16
122	0.39	3.1
240	0.19	0.80
490	0.097	0.19
936	0.046	0.052

Attenuation of the sound in the fluid induces a momentum flux, which is responsible for the formation of steady state fluid flow, called acoustic streaming [60]. Acoustic streaming can be crudely classified depending on the acoustic path length permitted in the fluid and the location of viscous attenuation. Schlichting streaming is the result of viscous shear attenuation near the solid–fluid boundary and Eckart streaming is the result of sound attenuation in the bulk of the fluid. Rayleigh streaming arises from Schlichting streaming. Further details on the types of streaming, their respective characteristics, and previous studies are summarized in Table 1 of the review by Friend and Yeo [15]. In cases where a free fluid surface is present, the nature of streaming and how it causes fluid transport is

slightly more complex.

SAW deliver sound into a liquid interphase at the Rayleigh angle, as long as the wave propagates from a region without the fluid to a region where the fluid is present. In general, the effect of the acoustic wave in the drop depends on the properties of the original wave in the substrate, the properties of the fluid, and the geometry of the drop. The effect of liquid deformation from a SAW can be break down into four regimes: mixing, translation, jetting, and atomization, majorly depend on the input power and frequency from a SAW device. Fig. 2.3(a) shows a droplet is deformed and elongated after a encounter a surface wave from a SAW device. Furthermore, Bussonniere et al. illuminated some of the physics by studying the oscillation, displacement, and contact line dynamics via a high speed camera, the results is shown in Fig. 2.3(b) [61]. They found that displacement of the rear and front contact lines alternately occur during each cycle. The oscillation speed is given by the product of the net drop displacement per oscillation cycle and the frequency of these oscillations. And, while the displacement is linear with the amplitude of drop deformation, the frequency is nonlinear with the amplitude due to hydrodynamic effects. The vertical oscillation could reasonably transition to jetting when inertia overcomes the capillary forces [62].

SAW induced liquid motion can also be found in droplet splitting from Colligen et al (Fig. 2.3)(c) [63]. A two part signal was required to produce first initiated internal rotation and then elongated the drop towards a necking event. Rotational flow due to the first part was critical to suppress jetting behavior allowing sufficient injection of momentum without ejecting the drop. From there a balance of capillary force and drainage due to necking

causes the drop to split. Moreover, when increase the amplitude of the SAW, droplet jetting can occur. Jetting occurs at a fluid-fluid interface when inertial pressure overcomes surface tension, which tends to maintain the interfacial shape. Weber number, We is a good metric for this balance; $W_e = \rho_f u^2 L_c/\gamma$, where L_c is the characteristic length, u is the fluid velocity, and γ is the surface tension. Viscosity, which intuitively should factor into this balance, is not present in Weber number, but is indirectly expressed via the fluid velocity. More viscous fluids will derive less inertia from a given stimulus. When fluid velocities are high enough to overcome surface tension, which increases for smaller fluid geometry, typically require a nozzle so that sufficient inertia can be generated. SAW is capable of producing very large surface accelerations, which translate into fluid velocity for a drop placed directly on the surface, thus eliminating the need for a nozzle [64]. Finally, when increase the SAW amplitude to the largest, atomization phenomenon occurs, where the sound wave induced the interfacial destabilization process and further atomized the liquid droplet as shown in Fig. 2.3(d) [65].

2.4 Particles behaviour in acoustofludics

Particle behavior in acoustofluidic systems is typically controlled by the following forces: direct and indirect (Bjerknes) acoustic radiation forces, viscous Stokes drag, van der Waals forces, electrostatics and electrodynamics forces. The latter two, van der Waals and electrically-driven forces, tend to be negligible in acoustofluidics, though there have been reports of combining these phenomena to achieve results not possible with acoustics

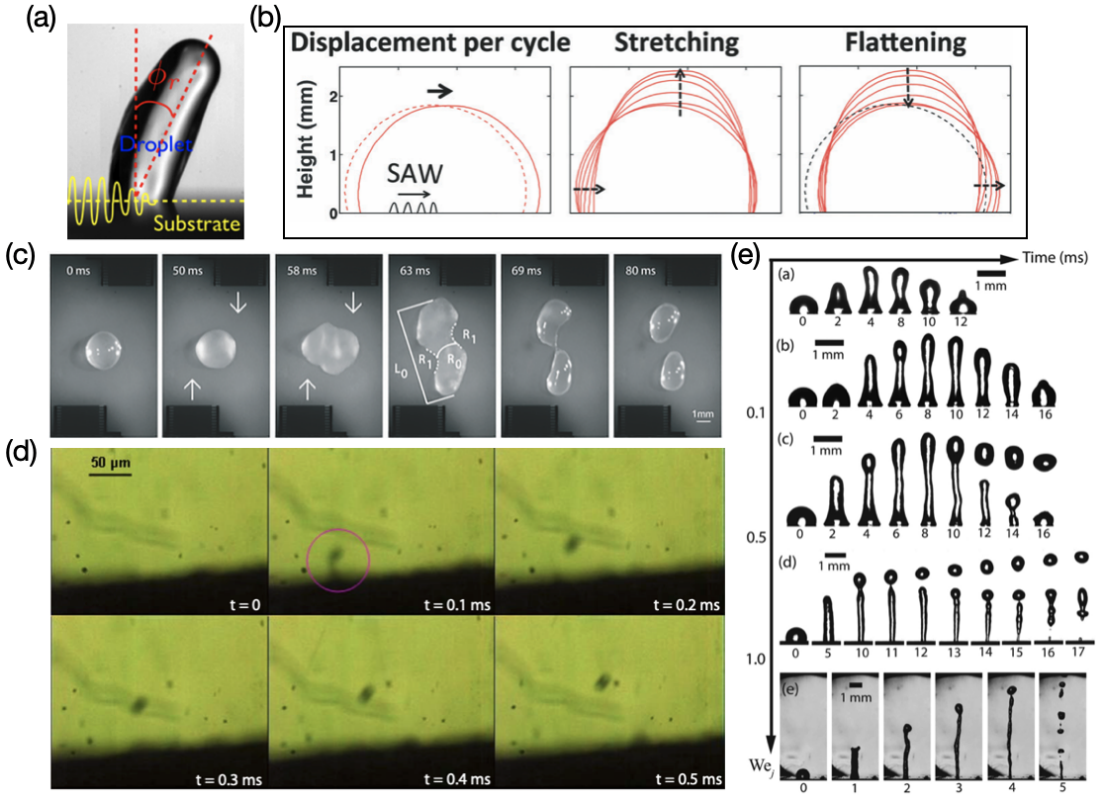

Figure 2.3: Surface acoustic wave induced deformation of a liquid droplet (a) An elongated water droplet which deformed at Rayleigh angle [61]. (b) Water droplet oscillation results into displacement of the rear contact line during stretching followed by displacement of the front contact line during flattering [62]. (c) A sequence of photographs depicting splitting event with counter-propagating SAW indicating by arrows [63] (d) Drop deformation and atomization above a hydrophilic LN substrate [64] (e)Jetting of water droplet with respect to the We number, from droplet elongation, pinch off a single droplet, and jet breakup to form multiple droplets [65].

alone. The direct SAW radiation force under a traveling wave was derived by King [66] and is expressed as:

$$F_{rt} = 2\pi\rho_0 A^2 \left(\frac{kr}{2}\right)^6 \left[\frac{1 + \frac{2}{9}\left(1 - \left(\frac{\rho_0}{\rho_p}\right)^2\right)}{2 + \left(\frac{\rho_0}{\rho_p}\right)^2}\right] \tag{2.9}$$

where r is the particle radius, $k = \omega/c$is the wavenumber, A is the complex velocity potential of the incident wave, ρ_0 is the liquid density, and ρ_p is the particle density. On the other hand, the radiation force under a standing wave is expressed as [66]:

$$F_{rs} = \left(\frac{\pi p_0^2 r^3 \beta_w}{2\lambda}\right)\left(\frac{5\rho_p - 2\rho_0}{2\rho_p + \rho_0} - \frac{\beta_c}{\beta_w}\right)(sin\,(2kx)) \tag{2.10}$$

where p_0 is the acoustic pressure, x is the position of the particle, λ is the wavelength of SAW, β_c and β_w are the compressibility of the particles and surrounding fluid, respectively. Notice that for a traveling wave F_{rs} is proportional to r^6 whereas, for a standing wave F_{rs} is proportional to r^3. However, in the real application, the surrounded fluid, particle compressibility and other important effects can greatly complicated the calculation and influence the results of the radiation forces.

Moreover, the stream-wise drag experienced by a particle of radius d can be approximated by the Stokes drag equation:

$$F_D = 6\pi\mu r v \tag{2.11}$$

where μ is the liquid viscosity and v is the velocity difference between the surrounding fluid and the particle.

Finally, the Bjerknes force, an interparticle force arising from the scattering of the incident acoustic wave, used to calculate the compressed particles or bubbles is defined as:

$$F_B = 4\pi r^6 \left[\frac{(\rho_p - \rho_0)^2 (3\cos^2\theta - 1)}{6\rho_0 r^4} V^2(X) - \frac{\omega^2 \rho_0 (\beta_p - \beta_0)^2}{9L^2} P^2(X) \right] \tag{2.12}$$

where $V(X)$ is the particle velocity amplitude, β_c is the particle compressibility, β_w is the liquid compressibility, L is the distance between two particles, and $P(X)$ is the acoustic pressure amplitude. The chapter 7 of this dissertation describe the relationship of the compressible magnetic particles under the external magnetic force and acoustic force.

Particle manipulation is one of the important applications for the SAW-induced fluid motion. Destgeer et al. found that the ring formation happens when the radiation force dominates drag force. They defined a constant k, where $k = \pi d_p c_f f_{LW}$, where d_p is the particle diameter, f_{LW} is the frequency of the Lamb waves, c_f is the speed of the sound in the fluid. When the $k > 1$, the radiation force dominates the drag force, and a ring is formed [2]. On the other hand, SAW was used to separate the particles inside a droplet by their sizes. Rogers et al. demonstrated using a 20 MHz SAW device to separate 2 μm particles and 30 μm particles. It is shown that the small particles (2 μm) for which the drag force dominates were concentrated in the bulk of the drop, while large particles (30 μm) for which radiation force dominates were driven to the periphery [3].

On the other hand, applying SAW to generate turbulence flow for mixing purpose

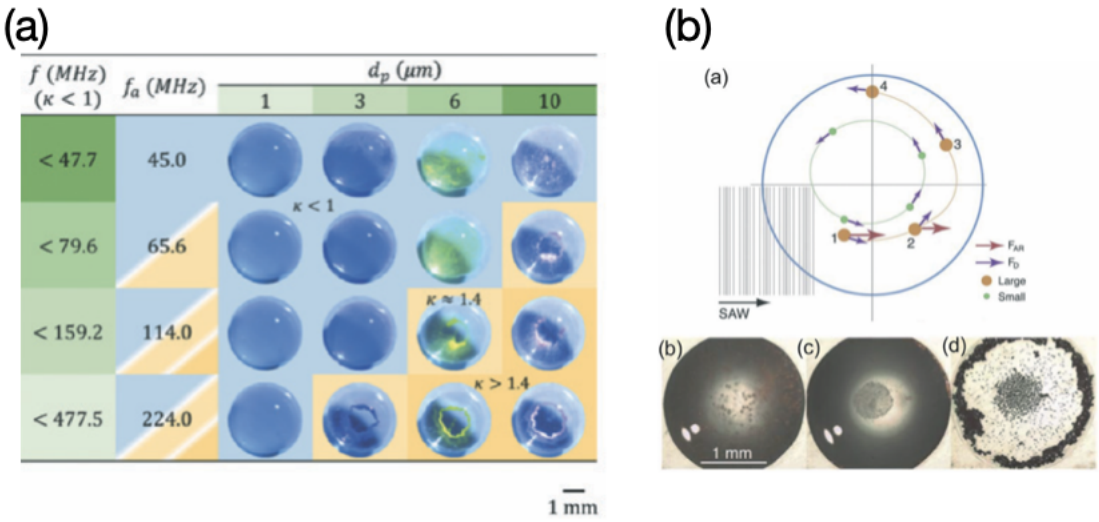

Figure 2.4: (a) SAW induced ring formation prediction based on the pre-determined conditions: force and droplet size. It is shown that when radiation force dominate the drag force, ring forms [2]. (b) SAW induced particle separation, forcing smaller particles to be at the periphery while the large particles are concentrated in the middle [3].

is also been shown. Cui et al. [4] applied high frequency 1.54 GHz SAW device to trigger the turbulent flow in a microfludics channel. The fast and homogeneous mixing was shown in Fig. 2.5(a). Moreover, TSAW can also be used for particle focusing, as demonstrated by Tan et al. A single IDT generates a SAW subsequently reflected from the opposite channel wall that generates a standing acoustic node within the channel if conditions are engineered correctly. Relatively weak SAW was used in Tan's work to focus particles in an initially homogeneous suspension into equally spaced nodal lines parallel to the channel with a separation of one-half the wavelength (see Fig. 2.5(b)) [67]. The dependence on wavelength allowed particles to be focused to different locations based on the applied frequency. Using focused SAW of higher frequency (up to 636 MHz), Collins and Ma recently demonstrated size-selective particle concentration—as small as

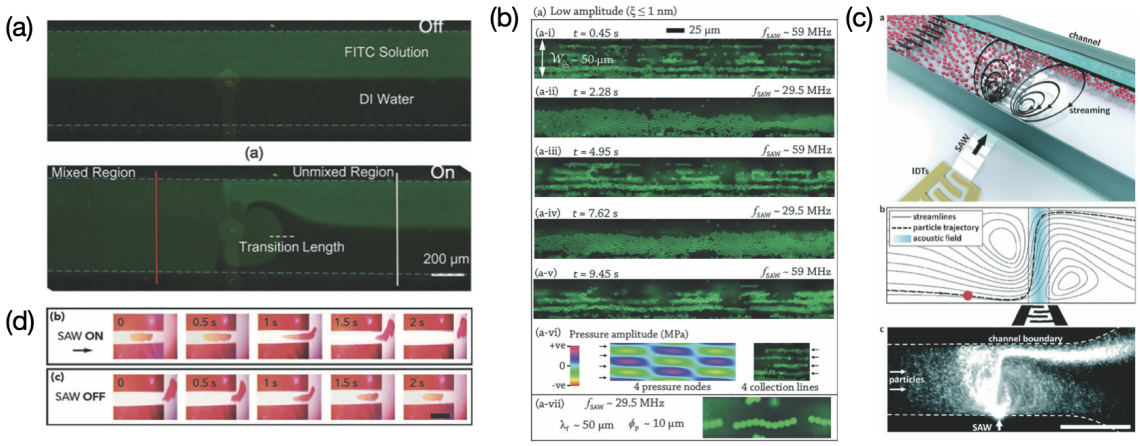

Figure 2.5: (a) Laminar flow and no mixing effect in the absence of acoustic waves. (b) Fast and uniform mixing of water and fluorescent dye in the presence of high frequency SAW within 1 ms [4]. (b) Time lapse images of TSAW focusing in a microchannel at amplitudes below 1 nm. Specific lines of focus could be selected by applied frequency and were quickly and easily switched, in this case between 29.5 MHz and 59 MHz [67]. (c) Shows adapting focused SAW to produce acoustic streaming to generate 300 nm particle mixing inside a microfludics channel [68]. (d) Manipulation of a liquid drop within the nanoslit based on SAW-driven acoustic streaming and capillary forces [69].

300 nm—via acoustic streaming. In one arrangement, streaming and radiation concentrate particles to one edge of a flow (see Fig. 2.5(c)) [68]. Note that size selective concentration in sessile drops has been demonstrated down to 200 nm. Finally, Minasari et al developed a room temperature LN/LN bonding technique and demonstrated a SAW-induced nanoslit platform for pumping nanoscale flows at up to 1 MPa, manipulating 10 fL droplet with overcoming the capillary force in the channel [69].

Chapter 2, in part, is a reprint of materials appears in Lab on Chip 2018. Connacher, William, Zhang, Naiqing; Huang, An; Mei, Jiyang; Zhang, Shuai; Gopesh, Tilvawala; Friend, James. The dissertation author was the co-primary investigator and author of this paper.

Chapter 3

Lithium battery

3.1 lithium battery

Lithium batteries are the smallest unit in a electrochemical energy storage systems, converting chemical energy to electrical energy and vise versa reversibly. Fig. 3.1 shows the essential components of a LIB, which are a cathode, anode, separator, and electrolyte [5]. The fundamental of a working LIB requires the anode and cathode to be oxidized or reduced at the same time depends on the charge or discharge processes. Typically, during a charge process, the Li ions that are inserted at the Li sites of a cathode structure are transported to the anode electrode through the electrolyte by passing through a separator in between the two electrodes. Before the Li ions intercalacte or deposit into or onto the anode, the ions pass through a solid electrolyte interphase (SEI) layer. Concurrently, the electrons are travel from the external connections from anode to the cathode, generating electric current. This process, due to the anode chemical potential is higher than cathode,

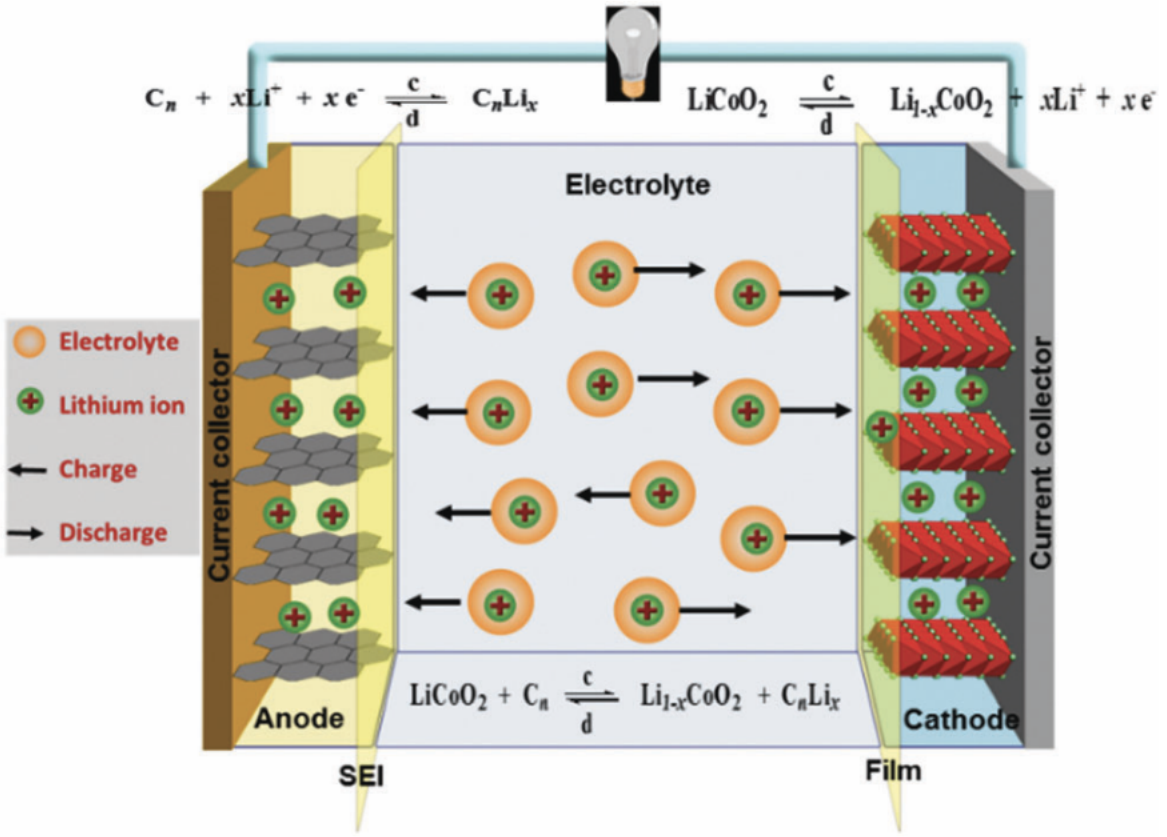

Figure 3.1: Schematic illustration of typical lithium ion battery, composed of an anode, cathode, separator, and electrolyte. [5]

the electrochemical energy is then stored. On the contrary, during the discharge process of a battery, the electron and Li ions are traveling in the reverse way of a charging. The electrochemical energy is then released to produce electric energy, and therefore, a electronic device is powered without a electric outlet.

3.2 Anode material

3.2.1 Graphite anode

Carbon based materials with a variety of compositions, morphologies, particle sizes have been used as the anode materials for LIB due to the proven safety, stability, high energy density, Li intercalacation/ extraction reversibility features. Among the different carbon based materials, graphite has been chosen to be one of the candidate anode as its safety, layered stability during the electrochemical reactions, long life cycle, and good conductivity. Moreover, the naturally abundant making it low cost and suitable for mass production. During the charging process, lithium ions are extracted from the graphite sheets and intercalacted into the cathode material (Eq.3.1)

$$LiC_6 \rightarrow C_6 + Li^+ + e^- \tag{3.1}$$

During the discharge process, lithium ions are intercalacted back to the graphite sheets as shown in Eq. 3.2, which is the reverse equation of the charge reaction.

$$C_6 + Li^+ + e^+ \rightarrow LiC_6 \tag{3.2}$$

However, graphite only permits the one lithium atom to intercalact with six carbon atoms, which turns into a stoichiometry of LiC_6 with a gravimetric capacity of 372 mAh/g. Owing to its 3–D structure nature, resulting into a moderate lithium diffusion rate of 10^{-7} to 10^{-9} cm^2 s^{-1}, which gave arise to the limitation toward a high power battery. To produce a

higher energy density and higher power density battery, many researches has investigated into different carbon materials. Graphene, consists of monolayer of carbon atoms into a 2–D graphite sheet. Graphene gas good electronic property, high charge carriers mobility, high intrinsic strength, high Young's modulus, and high surface area, making it a applicable as a battery electrode. The natural features resulting into a high energy density battery of 800–900 mAh/g [70]. However, the large irreversible capacity is the major drawback of the improvement it can generates.

Carbon nanotubes (CNTs), a hallow nanoscale cylinder cavity surrounds with flat graphite sheets, resulting into high surface area, high conductivity [71]. Depends on the manufacturing method or with additives, a CNTs can achieve a high power density such as to 5 C cycle rates with a good capacity of 600-1000 mAh/g. However, the long term cycle stability is one of the major issues [72].

Given by the easy to production, cycle stability, low hysteresis, and good energy density and power density, graphite is still the major consideration for the anode for the current LIB industry.

3.2.2 Lithium metal

Lithium metal (Li) is the ultimate Li choice for a LIBs due to it provides the unlimited Li source for a battery. Given by the intrinsic properties of a Li metal: low redox potential (-3.04 V vs. standard hydrogen electrode) and light weight, resulting into high theoretical capacity of 3860 mAh/g (approximate 10 times higher than the carbon-based electrode). More uniquely, the Li anode can further coupled with sulfur and oxygen electrodes, pro-

ducing a high energy density battery of 500 Wh/kg, which is double from the current LIB [73].

However, the decision in the 1980 s to abandon LMBs after years of research was in recognition of the difficult problem of dendrites forming on the Li metal anode during recharging as shown in Fig. 3.3 [7]. The dendrites will not only penetrate the separator and lead to serious safety issues but also will lead to low Coloumbic efficiency and a substantial reduction in charge capacity as they consume both Li and electrolyte.[74] These issues have long impeded commercialization of Li metal batteries (LMB) despite their otherwise overwhelming advantages.[75, 76] Dendrites tend to form as the charging current density becomes large (>1 mA/cm^2), leading to significant Li ion concentration gradients and an Li ion depletion layer adjacent the anode.[77, 78, 79, 80]

Dendrite mitigation in liquid electrolytes typically relies on chemistry, by adjusting the electrolyte composition [81, 82, 83, 84], concentration [85, 82], and additives [86], and by protecting the surface of the Li metal in LMBs[87, 88]. These approaches not only suppress the parasitic reactions between Li and electrolyte, but also provide uniform Li ion flux. Another approach is to form the Li into a three-dimensional scaffold structure [89, 90], improving the Li deposition morphology by even the electric field deposition by platting the Li inside the predetermined scaffold structure. Moreover, it is found that at elevated temperature (40°C or more), a final deposition morphology of Li chunks are formed due to a faster Li^+ diffusion rate [91, 92]. However, it is known that a faster degradation of cathode and electrolyte is associated at higher temperature. Even though these new approaches improve LMB cycling performance, they are still unable to address

adverse changes in the Li volume during standard cycling and performance problems at higher current densities (> 2 mA/cm^2).

That is to said, even though more efforts are required to fully solve the Li dendrite issues. It is still a very promising topic as the intrinsic property of Li is not replaceable. The properties offers a potential of high energy density and high power density battery, which are the essential for future electric vehicles.

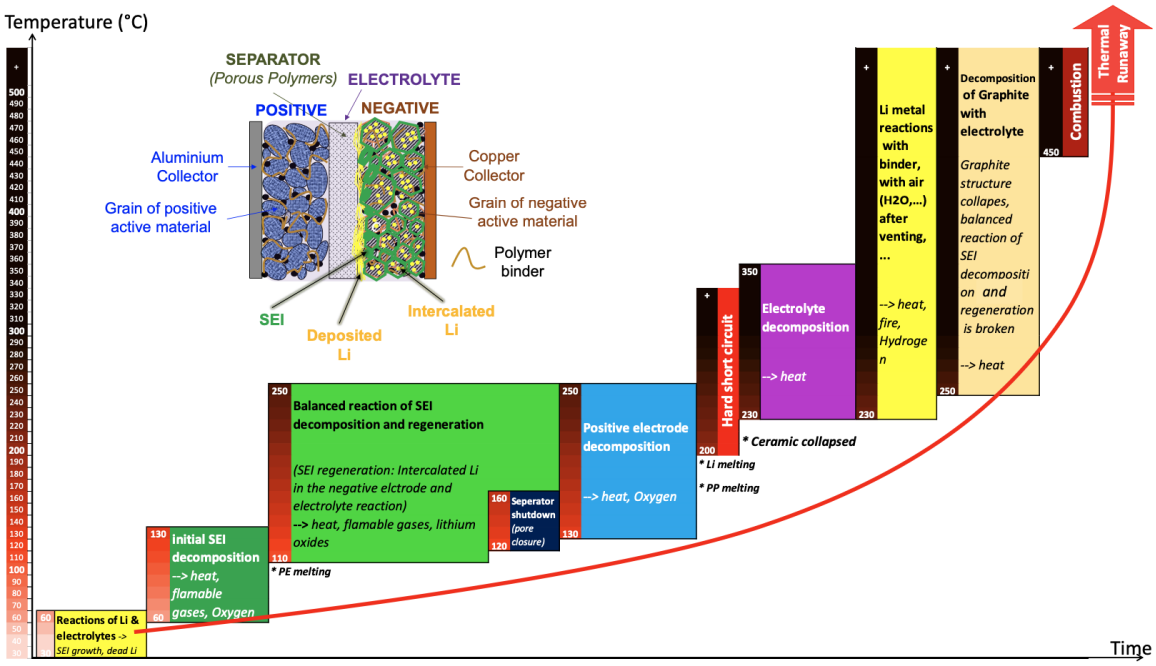

Figure 3.2: The chain reaction of thermal runaway at different stage with associated with the temperature of a battery change, here adopt an example of Ni-rich LIB [6].

3.3 Lithium platting and lithium dendrite

During the platting of Li metal, the potential that is driven is negative versus the Li potential. This cause the reduction of the Li ions to deposit on the anode surface [93].

In the ideal case, the Li deposition is homogeneous. However, this is not tend to be the case as the Li ion tends to deposit on the "hot spot" of a surface and made the deposition inhomogeneous [94]. The dendrite produce new SEI layer in every cycle, reducing the interface conductivity and battery capacity. Over the time, dendrite grows in the length, and finally penetrate the separator and cause the cell failure by the internal short circuits [7]. The scheme of the lithium dendrite growth is shown in 3.3.

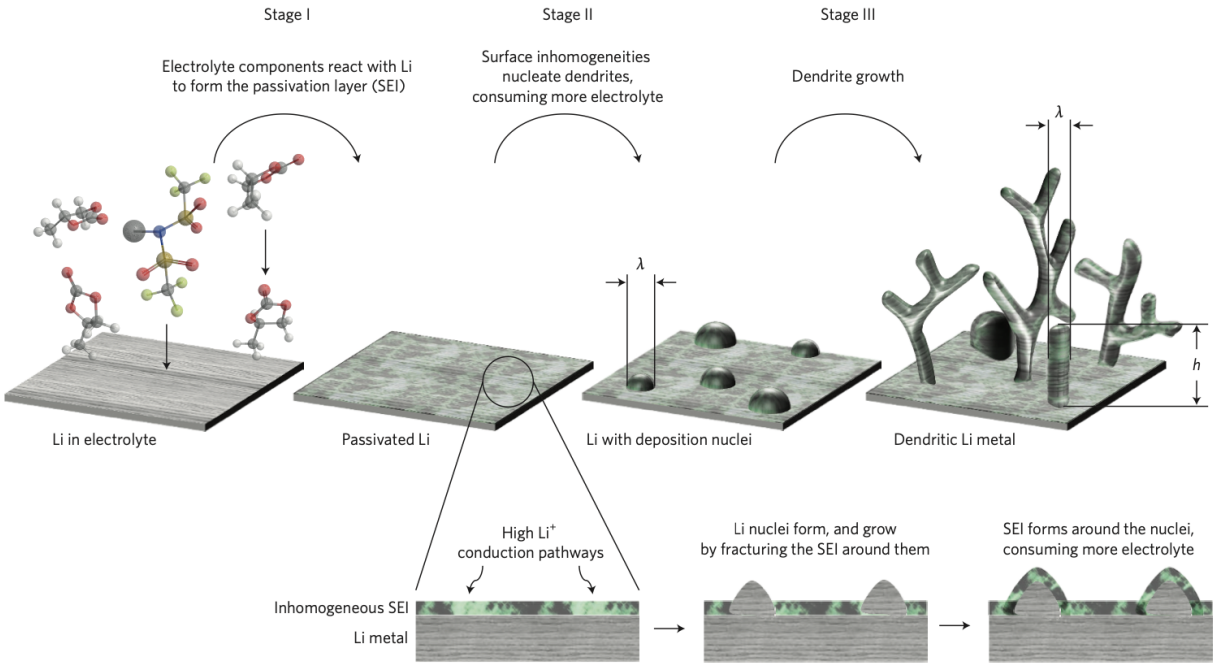

Figure 3.3: The growth of Li dendrite at different stage of the lithium deposition [7].

Li dendrite is not only happens in a LMB but also a LIB and it is considered as one of the most dangerous reactions as the metallic Li can deposit on the graphite surface and leading to the potential thermal runaway [95]. Lithium plating occurs when the rate of Li^+ reduction rate is mismatched with the Li intercalaction rate to the graphite electrode. The lithium platting is more severe at lower temperature Fig. 3.4(a), increased charge C-

rate Fig. 3.4(b), and increased state of charge Fig. 3.4(c). Moreover, the three factors are dependent with each others. Fig. 3.4(d) shows the Li deposition regions versus the no Li deposition regions with respects to the SOC, charge rate, and temperature. Finally, the Li deposition can be observed right after a battery is observed. Fig. 3.4(e) shows the results from a LIB cycled at same temperature but at different charge rates. It is shown that the lower the cycle rate, the morphology is closer to the pristine state (black graphite). However, with the increased cycle rate, for example, from 1 C rate, the morphology became light gray, indicating Li deposition on the graphite surface Fig. 3.4(e) [14].

3.3.1 Fast charging lithium battery

Charging at high rates has been shown to accelerate battery degradation, capacity fading, and safety issue. The main issue comes from the slow diffusion rate of the Li^+ at enhanced charge rates [96]. The electrolyte transport properties is the rate limiting factors that directly influence how fast a battery can be recharged. The ohmic voltage drop from fast charging or low temperature can results in hitting of the cut-off voltages earlier and therefore limited the deployable capacity [96]. Moreover, the Li^+ ions inevitably establish a concentration gradient during battery charging, becoming more severe at higher currents. At fast charging conditions, Li^+ ions can be depleted at very close to the anode, raising the further Li^+ intercalaction issues [97].

High-performance cells tend to use thin-layer or nanoparticle-based electrodes of eelctrochemically active media to minimize the diffusion distance [98]. The electrolyte is likewise tailored to improve the ionic conductivity and transport. Ion transport in the electrolyte

underpins the charging speed of the LIB. Furthermore, the capacity of an LIB is limited by the ohmic potential across the electrolyte as the cutoff voltage is prematurely achieved during charging. Fast charging depletes the Li^+ ions adjacent the anode as the their diffusion from the cathode and through the electrolyte via the separator is too slow to keep up, leading to a pronounced Li^+ concentration gradient, heating, and inhomogneous Li deposition and plating [99].

A major barrier to fast charging is the ionic conductivity of the electrolyte. A typical carbonate electrolyte in LIBs is $LiPF_6$ in ethylene carbonate (EC):dimethyl carbonate (DMC) at a weight ratio of 3:7, with an ionic conductivity of 8.5 mS-cm^{-1} with 1 M $LiPF_6$ salt, which is sufficient for low charge rates of 0.1– 1C. However, at high charge rates, $>$ 3C, at least 13 mS-cm^{-1} is necessary to avoid undesirable chemical reactions [100, 5]. Adding aliphatic esters—for example, methyl acetate (MA) or ethyl acetate (EA)—improves the ionic conductivity and overcomes this barrier while introducing another: decreasing the cycle life of the LIB through the formation of an undesirable solid electrolyte interphase (SEI) layer on the graphite anode [101, 102]. Formate, nitriles, and amides have also been considered [5], but poor compatibility with the LIB's cell chemistry reduces the Coulombic efficiency [5]. Notably, fluorethylene carbonate additive avoids these drawbacks, yet has one of its own: it is prone to defluorination by PF_5 produced from the $LiPF_6$ in the electrolyte [103].

Beyond chemistry, other means to increase the charge rate have been attempted. Exposure of the cathode to white light produces additional Mn^{4+} oxidation sites, improving charge transport [104]. External magnetic fields have been applied to produce electrolyte

flow via magnetohydrodynamics: a Lorentz force on the ions in the fluid electrolyte produces spiral-like flow, improving ion convection and helping to overcome the concentration gradient during fast charging. Unfortunately, magneto-hydrodynamics is extraordinarily inefficient [105].

3.4 Cathode material

Similar to the anodes, cathodes also need to possess excellent performances, such as structural stability, electrochemically compatible to the anodes, long life span, host lithium ions during cycling, small volume change. The first lithium ion cathode material is the lithium cobalt oxide ($LiCoO_2$), developed by Mizushima and Goodenough in 1980s and manufactured by Sony in 1990s [106]. $LiCoO_2$ is a layered lithium transition metal oxide with a layered rock-salt structure. Despite its achievements in the performance especially in the consumer electronics, a increase in the energy density is required for the electric vehicles requirement. The theoretical capacity of the $LiCoO_2$ is only 135 mAh/g, which is too low for today's high energy battery requirements. Due to the structure instability when more than 50% of the Li is extracted Moreover, the Co is toxic and expensive and shows safety concerns [107].

Later on, researchers adopted the similar radius elements such as Nickel (Ni) and Manganese (Mn), a successful example is lithium nickel manganese cobalt oxide (LiNi$-x$MnyCozO2, NMC). The first ratio that is proposed was $LiNi_{0.5}Mn_{0.5}O_2$ to completely removed Co. However, severe cycle life degradation was shown due to the Li/Ni disordered and results

into structure instability. Later on, the discover to the $LiNi_{0.5}Mn_{0.3}Co_{0.2}O_2$ (NMC532), $LiNi_{0.6}Mn_{0.2}Co_{0.2}O_2$ (NMC532), and $LiNi_{0.8}Mn_{0.1}Co_{0.1}O_2$ (NMC532) was been widely study. Generally, those new synthesis materials possess high energy density with high operation potential. Those materials follow a trend of the higher the Ni content, the higher the capacity can be released. However, the cycle life is shorter due to a faster material degradation [108].

Lithium excess layered is another type of the layered cathode materials. It also composed Li, Mn, Ni, and Co atoms and formed into the structure such as $(Li_2MnO_3)_x(LiMO_2)$, where M=Ni, Co, Mn. The working voltage can be 4 V and results into a high theoretical capacity of 250 mAh/g. The major drawback is the irreversible capacity at the first cycle, which is found out to originates from the lithium and oxygen loss. This issue is shown to mitigate by coating insulating materials on the surface, however, again it leads to the side reactions of the coated materials with the electrodes and electrolyte [108, 107].

Other types of the cathode materials, such as oxygen, sulfur has been a dream electrodes as they can provide ultra-high energy density. Moreover, they are cost-effective as they are both earth-abundant. However, the reversibility of the structure is one of the main issue that hinders them from full commercialization.

Fig. 3.5 summarized the current cathode capability and the future cathode direction. It is shown that the olivine $LiFePO_4$, layered $LiCoO_2$, and spinal $LiMn_2O_4$ are the commercial-graded materials. And the research are tailoring to either high voltage cathode materials or high theoretical capacity electrodes to generate a higher energy density battery system.

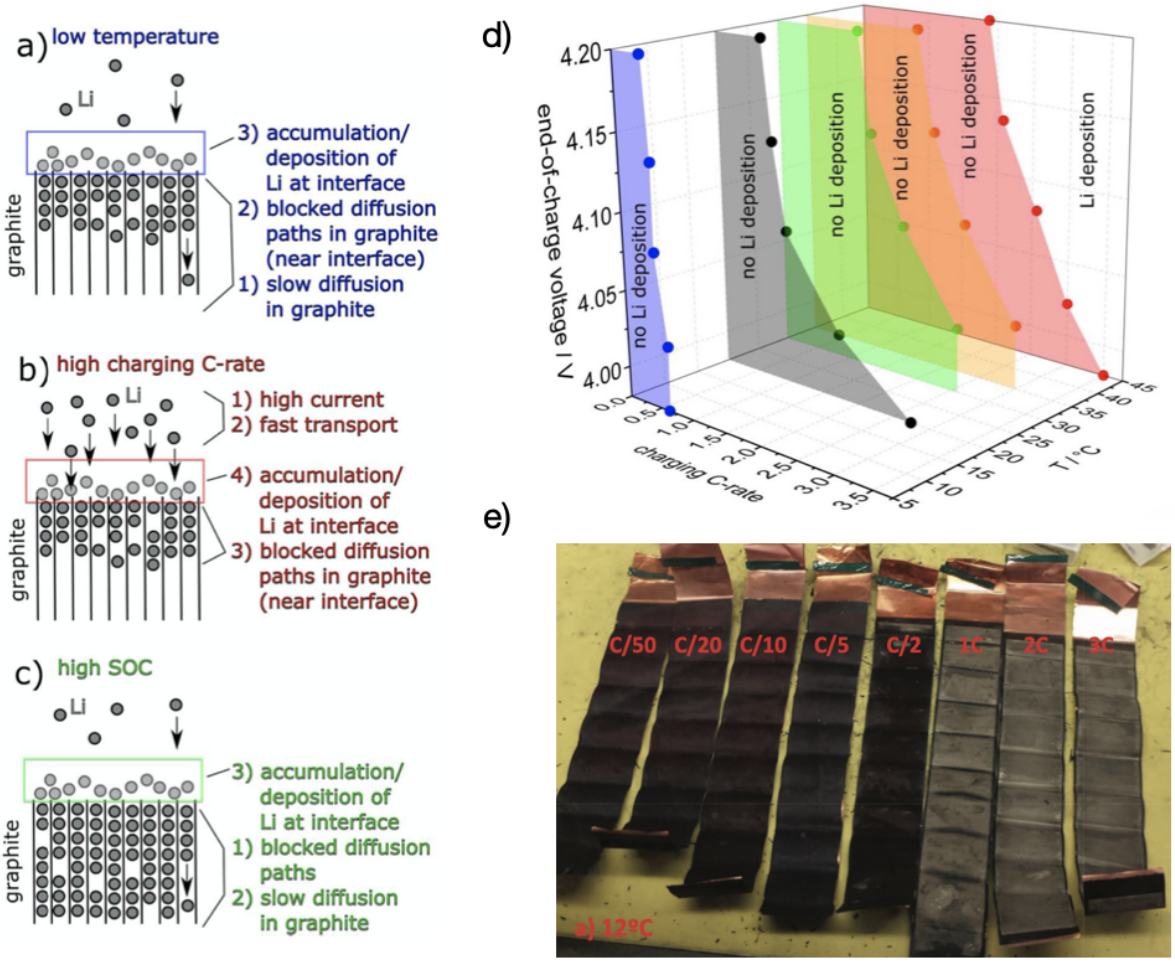

Figure 3.4: Cases that have higher chance to induce Li deposition on the graphite anode during charging (a) at low temperature, (b) at high charge C-rate, and (c) at high SOC [8]. (d) Moreover, the 3 factors are dependent with each others and the Li deposition areas can be plotted with the 3 factors. An example of Li deposition at increased charge rate at the same temperature [14].

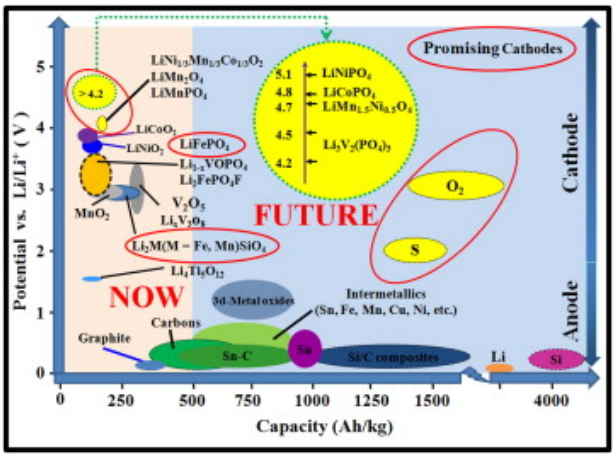

Figure 3.5: Electrode materials and corresponding electrochemical performances in the current LIB technologies. [9]

Chapter 4

Acoustic wave interaction with single layer lithium metal battery

4.1 Introduction

The rechargeable battery is the key to improving a broad swath of technology for society, from consumer and defense electronics, grid energy storage, and robotics to electric vehicles for sustainable transport. [73, 79] Properties in safety, rechargeability, specific capacity, and lifetime still need improvement: the best lithium ion battery today (240 Wh/kg) offers only six times the energy density of a lead-acid battery (40 Wh/kg) from 120 years ago.[109, 110, 111] As current state of the art Li-ion batteries (LIB) approach their theoretical limits by using lithiated graphite and meticulously engineered electrolytes, alternatives are sought to increase the energy density in batteries for emerging electronic devices.[112] Lithium metal (Li) is the ideal choice as an anode in Li metal

batteries (LMB) with a potential to deliver an energy density of 500 Wh/kg, at least double the current LIB. [73] The decision in the 1980s to abandon LMBs after years of research and adopt LIBs was in recognition of the difficult problem of dendrites forming on the Li metal anode during recharging. The dendrites will not only penetrate the separator and lead to serious safety issues but also will lead to low Coloumbic efficiency and a substantial reduction in charge capacity as they consume both Li and electrolyte.[74] These issues have long impeded commercialization of Li metal batteries (LMB) despite their otherwise overwhelming advantages.[75, 76] Dendrites tend to form as the charging current density becomes large (>1 mA/cm^2), leading to significant Li ion concentration gradients and an Li ion depletion layer adjacent the anode.[77, 78, 79, 80] Dendrite mitigation in liquid electrolytes typically relies on chemistry, by adjusting the electrolyte composition [81, 82, 83, 84], concentration [85, 82], and additives [86], and by protecting the surface of the Li metal in LMBs[87, 88]. These approaches not only suppress the parasitic reactions between Li and electrolyte, but also provide uniform Li ion flux. Another approach is to form the Li into a three-dimensional scaffold structure [89, 90], improving the Li deposition morphology by even the electric field deposition by platting the Li inside the predetermined scaffold structure. Moreover, it is found that at elevated temperature (40°C or more), a final deposition morphology of Li chunks are formed due to a faster Li^+ diffusion rate [91, 92]. However, it is known that a faster degradation of cathode and electrolyte is associated at higher temperature. Even though these new approaches improve LMB cycling performance, they are still unable to address adverse changes in the Li volume during standard cycling and performance problems at higher current densities (> 2 mA/cm^2).

Beyond chemistry, external magnetic force were also proposed to inhibit the continuous growth of the dendrite tip through magnetohydrodynamics principle [92, 113]. However, the energy consumption is high, while the performance is limited. Ultrasound has been used to drive acoustic streaming-driven fluid stirring and enhance the uniformity of ion distribution during traditional chemical vapor deposition.[114, 115] However, the ultrasonicators in these past works have always been large, inefficient, electrochemically incompatible, and very heavy—unsuitable for integration into a practical LMB. By contrast, surface acoustic wave (SAW) devices offer extraordinary power density in a fingernail-sized device, and are useful in drop handling, biological sensors, cell manipulation, and particle collection in microfluidics.[51, 1, 116, 117] Uniquely, they generate locally extreme accelerations of 10^8 to 10^{10} m/s^2, driving acoustic streaming-driven fluid flow at up to 1 m/s, and imparting acoustic forces upon objects present in the fluid, such as cells and micro to nano-scale particles.[15] SAW devices can be inexpensively produced through a standard ultraviolet photolithography and lift-off process to deposit interdigitated metallic electrodes onto a low-loss, single crystal piezoelectric Li niobate substrate, a commodity from decades of development and use in telecommunications.[50]

In this work, we expect to overcome the two underlying problems hampering rechargeable battery progress for over fifty years: protracted charging times and inadequate lifetime due to unfavorable morphological changes. We especially seek to avoid Li dendrites when metal deposition processes are employed in a carbonate-based electrolyte, EC/DEC, which is notorious [81] for Li dendrite formation and caused by ion depletion in the electrolyte adjacent the anode. A SAW-integrated LMB (SAW LMB) is therefore proposed,

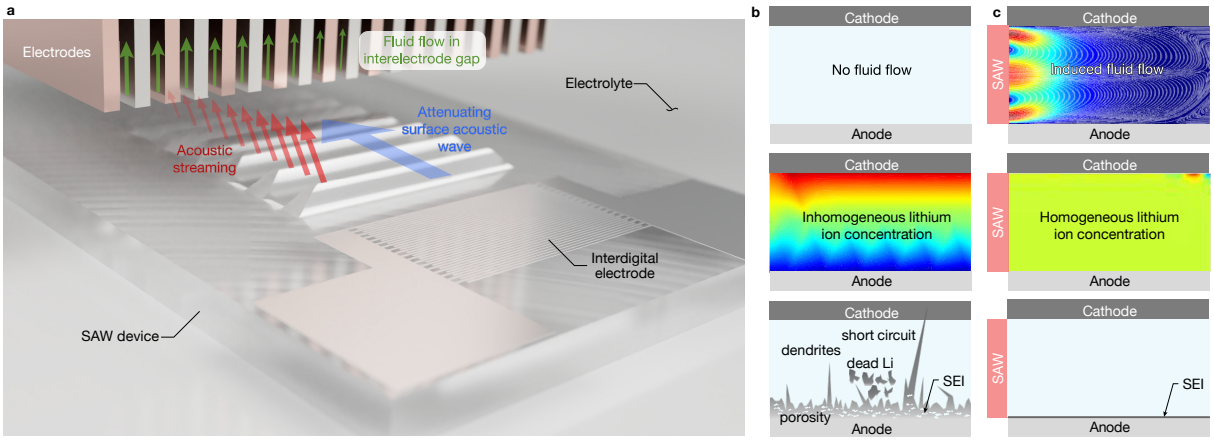

Figure 4.1: **A comparison of the working principles of traditional and SAW-driven Li metal batteries. a,** Illustration of how acoustic streaming drives electrolyte flow in the gap(s) between the electrode(s). A **b,** traditional LMB compared to **c,** SAW LMB based upon computations of the flow and ion distribution. For a traditional LMB, the stationary electrolyte permits high ion concentration gradients to appear during charging, producing Li dendrite formation, dead Li, Li metal volume expansion, uneven solid electrolyte interface (SEI) formation, and, eventually, short circuit of the cell. By contrast, in a SAW LMB, acoustic streaming recirculates the electrolyte, leading to a homogeneous ion distribution and uniform Li deposition during charging.

as shown in Fig. 4.1, as a new route to potentially overcome these longstanding problems. By driving sufficient flow of the electrolyte through the interelectrode gap, it becomes possible to prevent the formation of Li ion depletion regions, thus preventing dendrites, adverse heating, and electrolyte breakdown. The flow is driven by acoustic (fluid) streaming generated by the SAW device, significantly reducing the Li concentration gradient in the electrolyte—even during rapid charging—and uniform Li deposition is made possible. The power consumption of the SAW device is around 10 mWh/cm^2, relatively small in comparison to the charging itself, and in any case occurring when power consumption is acceptable: during charging. During LMB discharge, dendrites do not form, and so the SAW device may remain off. In what follows, we report the results of galvanostatic cycling

and post cycling analysis of prototype Li metal batteries to describe the beneficial effects of using SAW in them. Furthermore, we provide a closed-form model that both describes the underpinning physics and can be used to design the SAW device for a given battery configuration.

4.2 Experiment methods

4.2.1 Cell and SAW device fabrication

Copper (10 μm thick, MTI Corporation) was immersed in 1 M HCl followed by rinsing first with water and then with acetone to remove surface impurities and oxides before use as electrodes in all experiments. The Li (250 μm thick, MTI Corporation) was carefully scraped (245 μm thick after scraping) to remove any oxide layers before use as electrodes in all experiments. The lithium iron phosphate (LFP) electrode was prepared by first mixing LFP powder (MTI Corporation), polyvinylidene fluoride (Sigma Aldrich), and carbon black (C-preme LLC) in the mass ratio of LFP:PVDF:C= 75% : 10% : 15%; then made into a slurry by mixing with N-methyl-2-pyrrolidone (Sigma-Aldrich) as a solvent; pour-cast on Al foil; and finally dried in a vacuum oven for 12 hours. The areal capacity is around 1 mAh/cm^2. Commercial grade 1M solution of lithium hexafluorophosphate ($LiPF_6$) in a 1:1 (w/w) mixture of ethylene carbonate (EC) and diethyl carbonate (DEC) (BASF) was used as the electrolyte. Finally, a Celgard 480 separator was used between the cathode and anode.

The SAW device was fabricated through lift-off lithography to deposit twenty-eight

pairs of unweighted Au/Cr fingers and form an optimal[51] interdigital transducer (IDT) onto a 500 μm thick 127.68° Y-rotated, X-propagating cut lithium niobate substrate ($LiNbO_3$ (LN), Roditi).[15, 117] The SAW device was then coated with parylene C using chemical vapor deposition (PDS 2010 parylene coater system, Specialty Coating Systems) to prevent reactions with the electrolyte (see Suppl. Information). The baseline LMB and SAW-integrated LMB were assembled inside an argon-filled glovebox (MTI Corporation), where the moisture level and O_2 level were both ¡1 ppm. Both the baseline and SAW LMB cells were formed from perfluoroalkoxy alkane nuts, back and front ferrules, and main housings (PFA-820-6, Swagelock) in conjunction with current collectors (304 stainless steel rods, McMaster-Carr Supply Corporation), as illustrated in Fig. 4.2, to both seal the electrolyte and electrode from exposure to air and to safely test the cells.

4.2.2 Electrochemical measurement

Electrochemical studies were carried out in the Swagelock-based cell, placing the SAW device on one side within the housing and perpendicular to the electrode gap as shown in Fig. 4.2. The Coulombic efficiency measurements during Li plating and stripping were performed on Li‖Cu cells, where Cu serves as the working electrode and Li foil serves as the counter electrode. The Li was deposited on Cu at various current densities with a capacity of 1 mAh/cm^2. The deposited Li was then fully stripped to a cutoff voltage of 1 V. The Coulombic efficiency was defined as the amount of stripped Li divided by the amount of plated Li, and the average Coloumbic efficiency was calculated from this result for a range of current densities; the error bars denote the minimum and maximum

measured values.

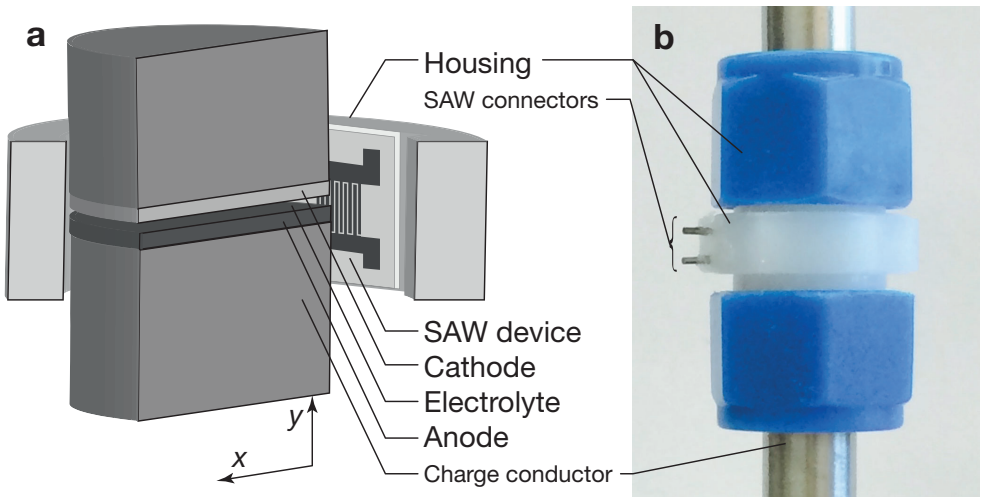

Figure 4.2: **Prototype Li metal battery configuration.** A **a** schematic cutaway and a **b** photo of an assembled prototype LMB, showing the placement of the SAW device to drive electrolyte recirculation. For scale, the charge conductors are 16 mm in diameter and the gap between the Li anode and $LiFePO_4$ cathode is 25 μm.

$LiFePO_4$ was used as the cathode while Li metal served as the counter electrode in full cells tested using standard galvanostatics. The charge and discharge currents were calculated based on the electrode size. For the baseline cell, the SAW device was present but was left off throughout testing. For the SAW-driven cell, the SAW device was turned on upon detection of the charging of the cell and was turned off during discharge. The charge-discharge cycling and the associated operation of the SAW device were automated during the experiments (LabVIEW), with a signal generator (SG–380, Stanford Research Systems) and amplifier (ZHL–1–2W, Mini-Circuits) used to drive the SAW device.

4.2.3 Morphological characterization

The cycled batteries were disassembled inside an argon-filled glovebox, the electrodes were collected, and the electrode samples were rinsed with dimethyl carbonate (Sigma-Aldrich) to remove the residual electrolyte on the surface of the electrode. The samples were then attached to a specimen holder (Ted Pella) using double-side carbon tape (Ted Pella) and sealed within an aluminized polyethylene bag inside the glovebox for transferring samples to the SEM. After transport to the SEM, the samples were quickly transferred from the bag to the scanning electron microscopy vacuum chamber (SEM Quanta 250, FEI Corp.) for imaging at 5 kV. The samples were exposed to air for less than three seconds.

4.3 Results and discussion

4.3.1 Li deposition onto copper in the presence of SAW

We first consider the Li deposition morphology on a copper (Cu) substrate using a carbonate based electrolyte of 1M $LiPF_6$ in ethylene carbonate/dietheryl carbonate (EC/DEC; Fig. 4.3). The carbonate electrolyte was chosen as our baseline electrolyte because it is known to be compatible with 4 V cathode materials and is capable of triggering dendrite formation at current densities of only 0.5 mA/cm^2 in an Li anode cell.[84, 118] The Li was electrochemically plated onto the Cu substrate at a current density of 1 mA/cm^2 (1 C) until the areal capacity reached 1 mAh/cm^2 for both baseline and SAW Li‖Cu cells (the deposition profile is shown in Fig. 4.3a). The voltage of the baseline cell continued

to decrease as Li was deposited, while the SAW cell exhibited a constant voltage near −0.1 V, indicating stable electrodeposition and perhaps homogeneous deposition [119]. Upon increasing the deposition current density to 6 mA/cm^2 (6 C) for cells with and without SAW (Fig. 4.3b), similar trends were observed. A more drastic drop in the deposition voltage was observed in the early stage of the deposition for the baseline cell, followed by a continued drop from -0.3 V at 0.1 mAh to -0.58 V at 1 mAh. In contrast, the SAW Li‖Cu cell showed a nearly identical voltage profile, becoming constant at -0.1 V. Notably, the baseline cell exhibited a deep voltage drop at the beginning of the 6 mA/cm^2 deposition (circled in Fig. 4.3b). This phenomenon has been seen before and is associated with the overpotential due to a heterogeneous nucleation barrier from the thermodynamic mismatch between Li and Cu,[120] and appears to be absent when using SAW.

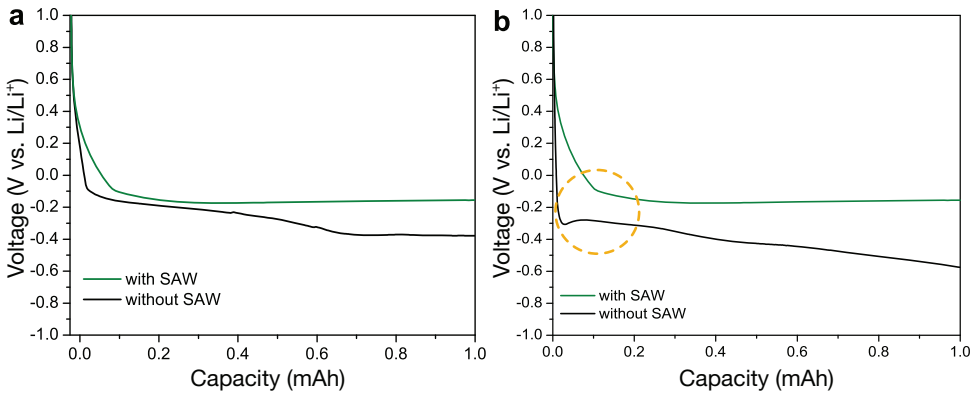

Figure 4.3: **First cycle deposition voltage profile of Li‖Cu batteries with and without SAW at 1 and 6 mA/cm^2 deposition rates to capacity of 1 mAh/cm^2. a,** comparison of the electrodeposition curves at deposition rate of 1 mA/cm^2 with (green) and without (black) SAW. **b,** comparison of the electrodeposition curves at 6 mA/cm^2 current densities with (green) and without (black) SAW.

The cycled cells were then disassembled and the electrodes were collected for scanning electron microscopy (SEM). When cycled at 1 mA/cm^2 current density, the presence of

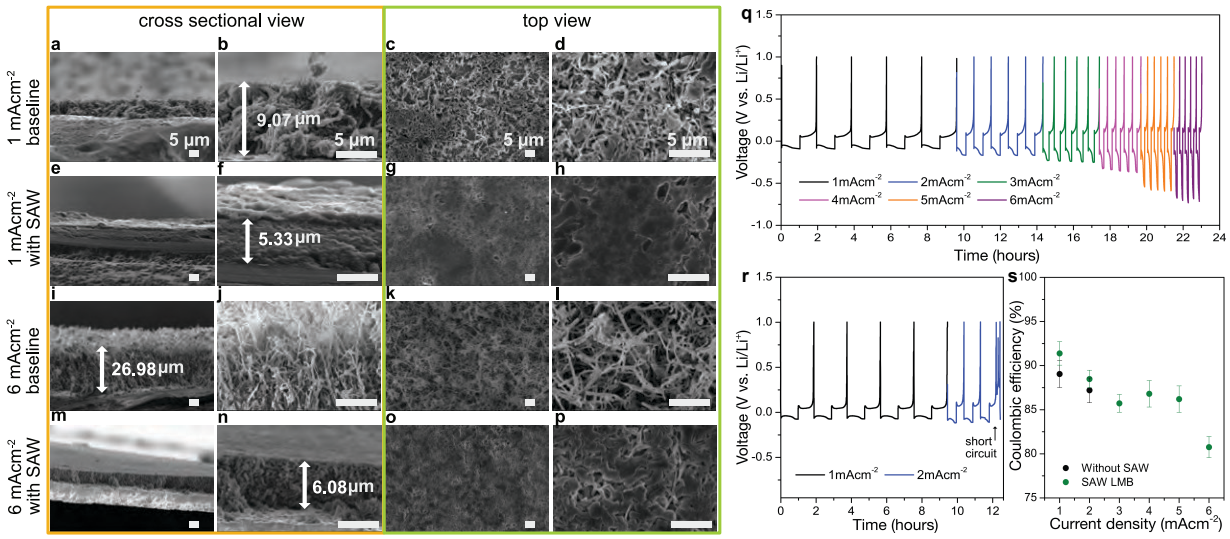

Figure 4.4: **SEM images of the Cu electrodes in the Li‖Cu system with and without SAW after the first deposition cycle.** Images of the Cu electrode after plating 1 mAh/cm^2 areal capacity of Li under 1 mA/cm^2. **a-d** the baseline Li‖Cu system shows substantially different morphology than **e-h** with SAW under the same conditions. Images of the Cu electrode after plating 1 mAh/cm^2 areal capacity under 6 mA/cm^2. **i-l** baseline and **m-p** SAW-driven Li‖Cu cell. Note the views among each column are at the same scale, with **a,b,e,f,i,j,m,n** cross-sections and **c,d,g,h,k,l,o,p** top views of the Cu electrode. Moreover, the comparison of Coulombic efficiency of Li‖Cu batteries with and without SAW at various deposition and stripping rates. The testing current densities incrementally progressed from 1 mA/cm^2 to 2, 3, 4, 5, and 6 mA/cm^2 until—in each case—the deposition reached areal capacity of 1 mAh/cm^2 and was stripped back to 1 V, producing an electrochemical profile of the Li‖Cu cell **q,** with SAW and **r,** without SAW. The **s,** average Coloumbic efficiency of the baseline (black dots) and SAW-driven Li‖Cu (green dots) are shown as a function of the current density.

SAW reduces the thickness of the deposited Li from 9.1 μm without SAW in the baseline cell to 5.3 μm with SAW. The thickness of the deposition is an indication of its density. A 4.85 μm thickness may theoretically be achieved if the deposition is completely dense without porosity or dendrites.[90] Based on these values, the porosities of the deposited Li are 46.7% and 8.5% for the baseline cell and SAW cell, respectively. The Li‖Cu cell produces better deposition behavior with SAW than without it. The top view images further support this conclusion, as the deposition morphology is dense and without dendrites for the SAW Li‖Cu cell (Fig. 4.4g and 4.4h) while porosity and dendrites are present in the baseline Li‖Cu cell (Fig. 4.4c and 4.4d).

We further examined the Li‖Cu cells' electrodes after Li deposition at a current density of 6 mA/cm^2. The Li deposition thickness in the baseline cell increased three-fold from 9.1 μm to 27 μm, giving an extremely high porosity of 82%, an indication of dendrite formation and loose deposition. [121] By comparison, the deposition thickness is far less when using SAW, 6 μm, with a much lower porosity of 19%. Though the porosity is certainly higher at 6 mA/cm^2 than 1 mA/cm^2, using SAW produces far better deposition behavior. Again, the top view images support this conclusion, with substantial porosity and dendrites in the cell without SAW (Fig. 4.4k, and 4.4l) and homogeneous "chunked" morphology with SAW (Fig. 4.4 and 4.4,p) known to result from homogeneous current distribution during deposition.[122]

Moreover, we investigated the deposition morphology of Li on Cu at a current density of 6 mA/cm^2 with different SAW power input: 40 mW ($<$ 100 mW for Fig. 4.4) and 500 mW ($>$ 100 mW). At a low SAW power input (40 mW), the thickness of 1 mAh/cm^2

is 8.75 μm (Fig. 4.5a,b). The deposition thickness is larger than the deposition thickness of 6.08 μm that is obtained at a SAW power of 100 mW (Fig. 4.4n). However, it is much thinner than the 27 μm thick Li deposition from the baseline cell (Fig. 4.4i). Moreover, the top view image shows that the morphology of the Li is a mixture of dendrite and chunk (Fig. 4.5c,d). The results indicate that when an insufficient power is applied, the effect of acoustic streaming to the Li^+ concentration gradient is limited. And therefore, resulting in a relatively looser Li deposition. On the other hand, at the SAW power input at 500 mW during the Li deposition, the Li deposition thickness is 7.5 μm (Fig. 4.5e,f), which is smaller than the thickness of the deposition at 40 mW (8.75 μm) but thicker than the Li deposition at 100 mW (6.08 μm). From the top view, it is shown that the deposition morphology is chunk-like structure (Fig. 4.5g,h).

We also examined the Coulombic efficiency of the Li‖Cu cell with the same carbonate electrolyte at different current densities, both with and without SAW (Fig. 4.4q and 4.4r). At 1 mA/cm^2 and 2 mA/cm^2, the average Coulombic efficiencies are 91.5% and 89% with SAW, nearly identical to the baseline cell without SAW, at 88% and 87%, respectively. However, at 2 mA/cm^2 the baseline cell exhibits signs of a short circuit with an unstable electrochemistry profile in the third cycle. By contrast, the SAW Li‖Cu cell continues to show good cycling performance even to the extremely high cycling rate of 6 mA/cm^2, maintaining >80% Coloumbic efficiency throughout.

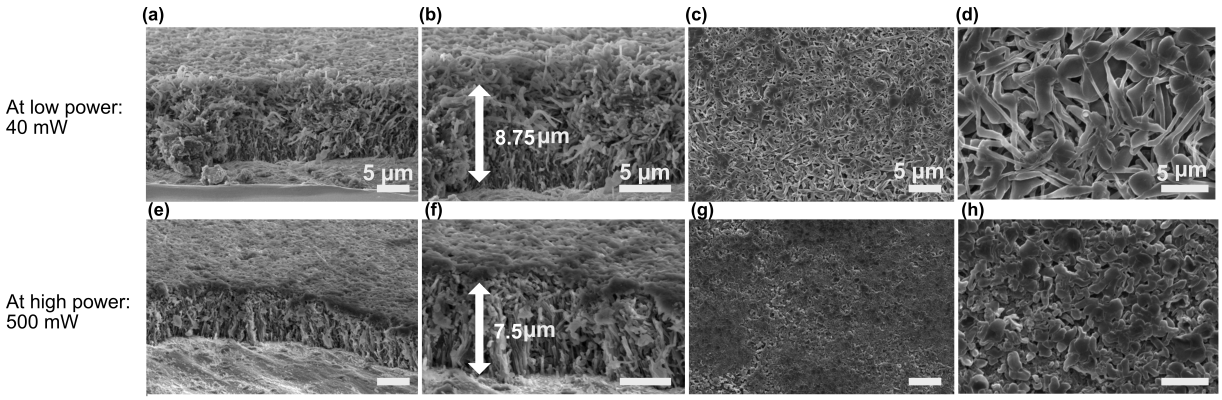

Figure 4.5: Deposition morphology of Li onto Cu at different power input from SAW. At low power input, 40 mW, the Li dendrite is shown. Similar to at high power input, 500mW, the Li dendrite is shown.

4.3.2 Effect of SAW-driven fluid flow on the high rate performance of Li‖$LiFePO_4$ batteries

We assembled a full Li‖$LiFePO_4$ (Li‖LFP) cell to investigate the practical aspects of integrating a SAW device into a battery, using LFP as the cathode with an areal capacity of 1 mAh/cm^2. The effect of SAW on the high charge rate capability of Li‖LFP cells is illustrated in Fig. 4.6 using 1M $LiPF_6$ in EC/DEC carbonate electrolyte at different current densities. Both charge and discharge are conducted at the same current density for this test. At a low current density of 0.5 mA/cm^2(0.5 C), both the baseline Li‖LFP cell and SAW Li‖LFP cell exhibit a discharge capacity of about 137 mAh/g, due to the small Li^+ concentration gradient present in the electrolyte at this current density, whether or not SAW is circulating the electrolyte. As the current density increases beyond 1 mA/cm^2 (1 C), however, a visible difference appears in the charge/discharge capacity due to the SAW. At 1 mA/cm^2, the capacity is 120 mAh/g without SAW, and 130 mAh/g with

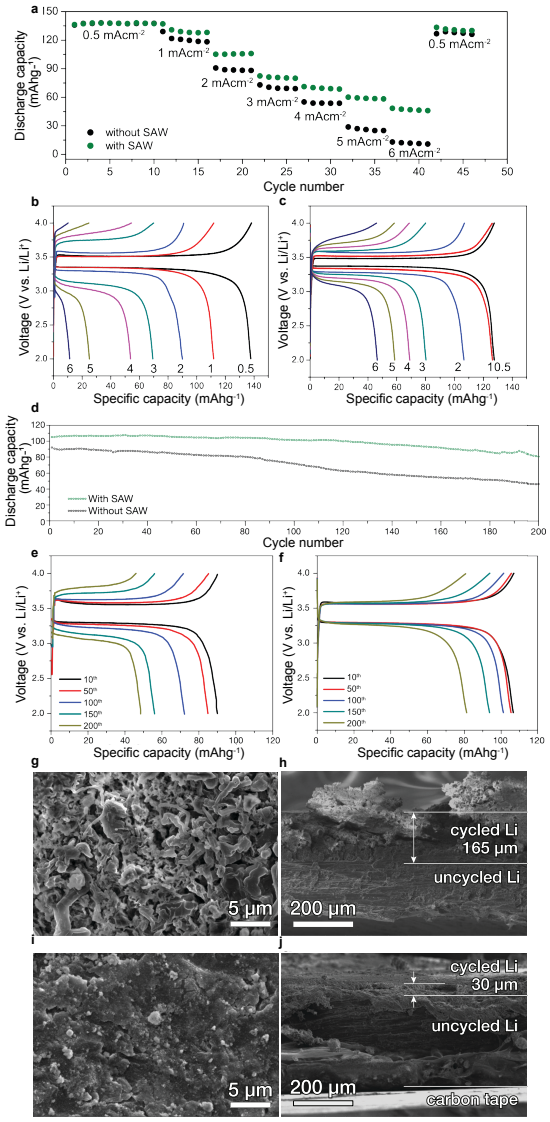

Figure 4.6: Electrochemical properties of baseline and SAW-driven Li‖$LiFePO_4$ cells at different cycle rates and long term cycleability. **a,** The discharge capacities of the baseline (black) and SAW-driven (green) Li‖$LiFePO_4$ cells are plotted versus the charge/discharge cycle at progressively greater current densities of 0.5, 1, 2, 3, 4, 5, and 6 mA/cm^2 (1 mA/cm^2 corresponds to 1 C)). The representative charge and discharge voltage profiles of Li‖$LiFePO_4$ cells are likewise shown for current densities of 0.5, 1, 2, 3, 4, 5, and 6 mA/cm^2 in the **b,** baseline and **c,** SAW Li‖$LiFePO_4$ cells. **d,** The discharge capacity of an Li‖LFP with (green) or without (black) SAW over 200 cycles at a current density of 2 mA/cm^2. The associated charge and discharge profiles of the **e,** baseline and **f,** SAW Li‖LFP cells are plotted at cycles 10, 50, 100, 150, and 200. Scanning electron microscopy of the morphology of Li in the Li‖LFP cell after 200 cycles. Extensive porosity and dendrites are present in a **g,** top view and **h,** cross sectional view of the Li anode from the SAW-absent Li‖LFP baseline cell, unlike the comparatively dense and smooth morphology of the Li anode from the SAW Li‖LFP cell (**i,** top view and **j,** cross sectional view).

SAW. Notably, 1 mA/cm^2 is reported as the critical current density that, upon exceeding, dendrites start to grow and the limitations of Li^+ ion diffusion begins to impact the battery's cycling performance.[110]

As the current density is further increased to 6 mA/cm^2(6 C), the discrepancy in capacity likewise grows due to the SAW. The baseline cell delivered only 11 mAh/g, retaining only 8% of its low-rate capacity, but using SAW in the cell provides a discharge capacity of 55 mAh/g, retaining 40% of its low-rate capacity. The SAW provides a five-fold increase in discharge capacity at 6 mA/cm^2 (6 C). Finally, each cell was returned to the starting current density of 0.5 mA/cm^2 (0.5 C), and the capacity was found to recover—indicating an absence of battery damage from the fast charge and discharge cycling. The SAW Li‖LFP generated a slightly higher capacity than the baseline Li‖LFP. Altogether, the drop in capacity at 6 mA/cm^2 (6 C) is mainly due to the limited Li^+ ion diffusion rate, producing a corresponding large Li ion concentration gradient. Without SAW, it is not possible to charge the Li‖LFP at high current densities. But with SAW, the discharge capacity is improved despite the high current density, perhaps due to improvement of the Li^+ ion diffusion and reduction of the associated ion concentration gradient via SAW-driven electrolyte recirculation.

The limitations in Li^+ diffusion can be shown in the charge and discharge profiles of the baseline Li‖LFP (Fig. 4.6b) and SAW Li‖LFP (Fig. 4.6c). At high cycle rates, the voltage hysteresis dramatically increased in the baseline Li‖LFP cell to 1.02 V at 6 mA/cm^2 (6 C) current density, 70% larger than the SAW Li‖LFP (0.59 V). The large voltage hysteresis is again an indication of the poor Li ion transportation in the baseline cell. Since the initial

voltage hysteresis is similar for the cell with or without SAW, the resistance otherwise present in the cell is likewise similar.

4.3.3 Full cell cycling of Li‖LFP with and without SAW

The long term cycling stability of the SAW Li‖LFP cells was investigated by applying a current density of 2 mA/cm^2 (2 C) for both charge and discharge over 200 cycles to Li‖LFP cells, using cut-off voltages of 2–4 V. The discharge capacity plotted in Fig. 4.6d–f indicates superior cycle performance with SAW in the Li‖LFP cell, with a greater discharge capacity throughout, from the initial to the 200$^{\text{th}}$ cycle. With SAW, the Li‖LFP offers 110 mAh/g of discharge capacity, modestly more than the 90 mAh/g of the baseline Li‖LFP without SAW. After 200 cycles, however, the SAW Li‖LFP cell retained 82% of its initial discharge capacity after 200 cycles, far more than the 51% capacity retained by the baseline Li‖LFP cell.

The effect of SAW is further apparent in a comparison between the individual charge and discharge voltage profiles of the baseline Li‖LFP in Fig. 4.6e and the SAW Li‖LFP cell in Fig. 4.6f. The baseline cell's polarization increases with the number of cycles, and there is a 63% increase in the polarization voltage from the 10$^{\text{th}}$ cycle (0.28 V) to the 200$^{\text{th}}$ cycle (0.77 V). The increase in polarization is an indication of dead Li and Li dendrite formation,[121] leading to a reduction in discharge capacity as cycles accumulate. However, with SAW, the polarization voltage increases less than 10% from 0.266 V at the 10$^{\text{th}}$ cycle to 0.298 V at the 200$^{\text{th}}$ cycle, indicating the achievement of stable cycle performance using SAW.

The cycled Li‖LFP cells were disassembled to examine the morphology of the Li anodes using scanning electron microscopy (SEM, Fig. 4.6g–j). The Li anode from the baseline cell exhibits porous morphology and dendritic growth in Fig. 4.6g,h. However, with SAW, the Li anode morphology is comparatively dense and smooth in Fig. 4.6i,j. Noting the total thickness of the pristine Li is 245 μm, this substantial difference may be quantified by measuring the thickness of the (porous) cycled Li and (dense) uncycled Li using Fig. 4.6i,j. The thickness of the uncycled Li is 145 μm without SAW, and is 225 μm with SAW. In the baseline Li‖LFP cell without SAW, 41% of the Li participates in the cycling. The thickness of the cycled Li increased from 100 μmm to 165 μm after 200 cycles without SAW, a 65% increase. By contrast, with SAW in the Li‖LFP cell, only 8% of the Li is cycled, and the cycled Li increased from 20 μm to 30 μm after 200 cycles, a 33% increase.

4.4 The mechanism responsible for SAW-driven battery performance improvement

The diffusion of Li^+ ions is crucial to the performance of Li batteries: its charge and discharge rate, capacity, and stability. Most batteries have quiescent electrolyte, with $\times$ $u = 0$ for the electrolyte velocity, leaving diffusion to migrate Li^+ ions across concentration gradients in the electrolyte and to the anode during charging (Fig. 4.1b).[123] Diffusion is inadequate in high-speed charging, and by generating flow in the electrolyte, SAW-driven acoustic streaming *augments* diffusion—in fact supplants it—in transport of Li^+ ions (Fig.4.1c), but the details require careful analysis summarized here and provided in

more detail in the Supplementary Information.

Past analyses typically employ spatially one-dimensional models,[123, 124] as the full problem is not easy to solve, even with a computer.[125] Here, we seek an immediately useful, closed-form result to both explain the physical phenomena and provide a tool for battery design incorporating SAW-driven electrolyte recirculation, examining how flow inhibits the early growth of small dendrites, as suggested by classic experimental work on impinging flow.[126]

We assume the cell is near its limiting current density, the worst case scenario for dendrite formation. We further assume that slight, sinusoidal morphological imperfections are present along the electrode—of wavelength λ and amplitude ϵ from the initial construction of the battery —forming "hotspots" that locally enhance the rate by which metal ions adsorb onto the electrode and allow for the initial growth of dendrites. With our electrolyte, the Reynolds number is $\mathrm{Re} = \rho u L/\mu \approx 0.2 - 2$, as a function of the density ρ, viscosity μ, and length scale L, indicating laminar, almost viscous, flow as one might expect from the dimensions of the structure, though the Li^+ ion convection is strong, potentially with an ion transport boundary layer of $\ell \approx 0.1 - 1$ μm thickness, as the diffusion coefficient[127] is ~10^{-9} m^2/s, due to the requirement that the leading order convective and diffusive components in the transport equations must become comparable in magnitude within the boundary layer, in turn satisfied by requiring that the corresponding Peclet number in the boundary layer is $\mathrm{Pe} = u_c \ell/D \approx 1$ in a simplified analysis assuming the electrolyte flows as a simple shear flow with characteristic velocity u_c. The small thickness of the boundary layer compared to the interelectrode gap, and the lack of excess pressure

therein supports—at least locally—our simple shear flow assumption. It is similar to a past successful approximation[128] of a parabolic velocity profile between flat and parallel electrodes as simple shear flow in the boundary layer near the electrodes.

By modeling the advective and diffusive transport of ions, both transverse and parallel to an electrode in the cell, as a two-dimensional convection-diffusion model as detailed in the Supplementary Information, we connect the acoustically-driven electrolyte flow in the cell to the ion distribution in the vicinity of these hotspots. The connection is made via an order-of-magnitude result that defines the Li ion adsorption onto the anode during charging:

$$\frac{-i}{\mathrm{Pe}^{1/3} D c_{\mathrm{bulk}}/\delta} = \frac{3^{1/3}(1-\epsilon)}{\Gamma(1/3)} \left(\frac{x}{\delta}\right)^{-1/3} + \epsilon \frac{\sqrt{\pi}(3/2)^{1/3}}{\Gamma(1/6)} (k\delta)^{1/3} \left(\sin(kx) - \sqrt{3}\cos(kx)\right) + \mathscr{O}[\epsilon], \tag{4.1}$$

The SAW-driven mechanism reducing dendrite growth and facilitating dense Li plating is counterintuitive. Acoustic streaming driven by SAW causes fluid flow in the interelectrode gap. During charging, the Li^+ ion flux is generally enhanced by the flow as indicated by the first of the two terms on the right-hand side of eqn. (4.1). However, this spatially ($x^{-1/3}$) decaying ion flux is perturbed by the second term on the right-hand side of eqn. (4.1), which represents the variation in ion flux due to the presence of localized hotspots that arise from the initial electrode roughness. The combined contribution of both terms indicates the key to eliminating the possibility of dendrite growth: the dominance of the first term over the second. We seek the critical length, x_{crit}, over which the spatially oscillatory behavior of the second term is suppressed by requiring the change in

ion absorption current, i, with respect to x, $d(-i)/dx > 0$. This avoids a sign change in the current and localized regions of enhanced ion flux—hotspots that will lead to dendrites and porous deposition. With some effort, the critical length $x_{\text{crit}} \approx \lambda\sqrt{\text{Pe}}/18$.

The effect of the flow via the Peclet number Pe is to produce a region of size x_{crit} over which nonuniform ion deposition is prevented. The size of this region depends upon the wavelength of the initial roughness, $\lambda = 200\mu$m, both an artificial construct to avoid lengthy computations in favor of useful, analysis-based design tools and a fair representation of as-supplied, pristine Li surface morphology. The Peclet number linearly depends upon the acoustic streaming flow, and this helps us define the characteristics required from the SAW device to ensure the critical length is at least equivalent to the battery size—$L_{\text{bat}} \sim 10$ mm in our case.

If we equate $x_{\text{crit}} \approx L_{\text{bat}}$, and substitute in the definition for the Peclet number, we may identify the necessary flow velocity required to avoid nonuniform ion deposition over a region equivalent to the size of the battery, $u_{c,\text{crit}} \approx D(18L_{\text{bat}}\lambda)/\ell \sim 0.1$ m/s in our system. This allows us to determine the SAW input power required[129] to suppress dendrites throughout, $P_{\text{crit}} = \rho\alpha w c u_{c,\text{crit}}^2 \sim 0.1$ W, where $\alpha = 455$ μm refers to the attenuation length of the SAW in the fluid-loaded LN substrate, $w \sim 10$ mm is the aperture or width of the SAW, $c = 1498$ m/s is the speed of sound in the electrolyte, and $\rho = 998$ kg/m^3 is the electrolyte density. We may also determine the ideal frequency to use for the SAW by equating the attenuation length of the acoustic wave, β, to the battery size, $\beta = L_{\text{bat}}$. This ensures locally generated acoustic streaming throughout the battery, helping to overcome the presence of the separator and still induce fluid flow over the entire

interelectrode gap. The frequency is $f_\beta = \sqrt{(\rho c_{\mathrm{SAW}}^3) / [4\pi^3 (\mu + \mu') L_{\mathrm{bat}}]} \sim 10^8$ Hz, the reason we choose 100 MHz in this study. The speed of the Rayleigh wave SAW in the LN substrate is $c_{\mathrm{SAW}} = 3900$ m/s and the dynamic and dilatational viscosities of the electrolyte are, respectively, $\mu = 1$ s-mPa and $\mu' = 3$ s-mPa. These values are consistent with our experimental observations in the ability to suppress nonuniform Li^+ ion deposition with SAW in prototype Li metal batteries.

The representation of electrolyte flow and ion transport

The steady mass transport of ions, assuming the electrical field in the battery is effectively screened by the high electrolyte concentration, is governed by

$$\mathbf{u} \cdot \nabla c = D \nabla^2 c, \tag{4.2}$$

where $c, \mathbf{u}, D$ are the ion concentration, velocity field, and the constant ion diffusion coefficient, respectively. To simplify the problem we further assume a 2D problem, in which the x coordinate is along the flow in the boundary layer and the y coordinate traverses the electrodes, which are assumed to be flat and parallel (prior to the physical growth of dendrites). We solve the problem subject to the mass conservation of metal ions in the electrolyte[124] and a harmonic variation in ion concentration along the surface of the Li electrode, which is associated with local ion depletion areas in the vicinity of hotspots for the growth of dendrites,

$$\frac{1}{A} \int \int_A c \, dA = c_{\mathrm{bulk}} \tag{4.3}$$

and

$$c = \epsilon c_{\text{bulk}} \left(1 + \cos(kx)\right) \text{ at } y = 0, \tag{4.4}$$

respectively, where A is the area between the electrodes along the x and y coordinates in a 2D view of the system, c_{bulk} is the concentration of Li ions in the electrolyte, ϵ is a small perturbation parameter of the excess ion depletion near hotspots with compare to the level of ion depletion away from hotspots, and k is a perturbation wavenumber of ion depletion, which physically may be taken to account for the density of the hotspots along the Li electrode with a corresponding wavelength of $2\pi/k$ that is associated with the characteristic separation between hotspots. Here, it also is associated with the physical roughness of the pristine Li anodes. The surface of the Li electrode is given at $y = 0$. In these expressions, localized minima along the Li electrodes are permitted, where the ion concentration fully vanishes and hence supports the hotspots. The velocity field in the boundary layer is taken to be $u = \beta y e_x$ and $v = 0 e_y$, where u and v are the components of the velocity field along the e^x and e^y unit vector directions associated with the x and y coordinates, respectively, and $\beta \approx u_c/\delta$ is the shear rate along the y coordinate, where δ is a characteristic length of the flow in the boundary layer. The current carried in large part by the ions is a function of the electrical potential difference between the electrodes.[130, 131]

A route to a closed-form model for the SAW-driven LMB Li^+ ion diffusion and deposition phenomena

Using the transformations $x \to \delta x,\ y \to \delta y,\ c \to c_{\text{bulk}}c,\ (u,v) \to u_c(u,v),\ L \to \delta L,\ k \to k\delta, h \to h/\delta$ we render the problem in eqns. 4.2, 4.3, and 4.4 dimensionless, giving,

$$u\partial_x c + v\partial_y c = \frac{1}{\text{Pe}}\left(\partial_{xx}c + \partial_{yy}c\right), \tag{4.5}$$

with the Peclet number defined as Pe=u_c/D; eqn. 4.5 is subject to

$$\frac{1}{A}\int\int_A c\ dA = 1 \tag{4.6}$$

$$c = \epsilon\left(1 + \cos(kx)\right) \text{ at } y = 0, \tag{4.7}$$

where we encounter two small parameters in this problem, i.e., $1/\text{Pe} \ll 1$ ($\text{Pe} = u_c\delta/D \gg 1$) in eqn. 4.5 and $\epsilon \ll 1$ in eqn. 4.7. We assume a simple shear flow in the vicinity of the Li electrode, so that $u = y$ and $v = 0$.

The system of equations 4.5–4.7 supports a transport boundary layer of ions and hence is associated with a singular asymptotic expansion of the concentration c in 1/Pe. We thus consider an outer concentration field far from the Li electrode, described by C, and an inner (boundary layer) concentration field near the electrode, described by c. In order to solve the inner (boundary layer) problem we rescale the coordinate y in the form $y = Y\text{Pe}^{-n}$, so that the leading order diffusive term satisfies convection. Both concentration fields must

satisfy $\lim_{y\to 0} C = \lim_{Y\to\infty} c$. We then expand the leading order concentration field in powers of ϵ according to the series expansion $C = C_0 + \epsilon C_1 + ...$ and $c = c_0 + \epsilon c_1 + ...$ as follows.

Leading order ($O(1)$) expansion To leading order, the problem in eqns. 4.5-4.7 in the outer field satisfies the system of equations

$$u\partial_x C_0 + v\partial_y C_0 = 0, \tag{4.8}$$

and

$$\frac{1}{A}\int\int_A C_0 \; dA = 1, \tag{4.9}$$

which gives the trivial solution $C_0 = 1$. In the inner (boundary layer) field, where we use the transformation $y = Y\mathrm{Pe}^{-n}$, the problem takes the leading order form,

$$Y\partial_x c_0 = \partial_{YY} C_0, \tag{4.10}$$

where $n = 1/3$, so that the leading order diffusive terms is satisfied by convection. The corresponding boundary conditions at the surface of the electrode and far away from the boundary layer (where the inner solution is matched to the outer solution) are then,

$$c_0 = 0 \text{ at } Y = 0, \quad \text{and} \quad c_0 = 1 \text{ at } Y \to \infty, \tag{4.11}$$

respectively. An analytical similarity solution to this problem is obtained by using the transformation $\zeta \equiv Y/x^{1/3}$. The boundary layer problem translates then to,

$$-\frac{\zeta^2}{3}\frac{dc_0}{d\zeta} = \frac{d^2c_0}{d\zeta^2}, \tag{4.12}$$

and

$$c_0 = 0 \text{ at } \zeta = 0, \quad c_0 = 1 \text{ at } \zeta \to \infty. \tag{4.13}$$

This system of equations is satisfied by

$$c_0 = \frac{3^{1/3}}{\Gamma(1/3)} \int_{\zeta'=0}^{\zeta} e^{-\zeta'^3/9} d\zeta', \tag{4.14}$$

where $\Gamma()$ is the Euler gamma function and $\Gamma(1/3) \approx 2.68$. Taking the y derivative of the leading order concentration near the surface of the Li electrode at $Y = \zeta = 0$ gives

$$\partial_y c_0|_{y=0} = \frac{dc_0}{d\zeta} \times \partial_y \zeta|_{y=\zeta=0} = \frac{3^{1/3}}{\Gamma(1/3)} \left(\frac{\mathrm{Pe}}{x}\right)^{1/3}. \tag{4.15}$$

Hence the dimensional flux of ions to the electrode is,

$$i_0 = -D\partial_y c_0|_{y=0} = -D\frac{3^{1/3}}{\Gamma(1/3)}\frac{c_{\mathrm{bulk}}}{\delta}\left(\frac{\mathrm{Pe}}{x/\delta}\right)^{1/3}, \tag{4.16}$$

where the negative sign infers that the flux is to the electrode. Thus, it is clear that the current generally increases when the Peclet number (the convective flow) increases and when the characteristic length scale of the flow decreases (shear rate increases) while

the surface of the electrode is flat and homogeneous. Moreover, the current decreases downstream since the convection of ions reduce the variations in ion concentration along this direction.

Second order ($\mathscr{O}[\epsilon]$) expansion Since C_0 is a constant, the next-order problem in eqns. 4.5–4.7 in the outer field satisfies the system of equations

$$u\partial_x C_1 + v\partial_y C_1 = 0, \tag{4.17}$$

$$\frac{1}{A}\int\int_A C_1 \, dA = 0, \tag{4.18}$$

which, again, gives the trivial solution $C_1 = 0$.

The next-order problem in eqns. 4.5–4.7 in the inner field is

$$Y\partial_x c_1 = \partial_{YY} c_1 + \partial_{xx} c_0, \tag{4.19}$$

$$c_1 = 1 + \cos(kx) \text{ at } Y = 0, \tag{4.20}$$

$$c_1 = 0 \text{ at } Y \to \infty, \tag{4.21}$$

where again we use the transformation $y = Y\mathrm{Pe}^{-1/3}$ and further require that $\epsilon \approx \mathrm{Pe}^{-2/3}$ in order to include the perturbation of the ion concentration in eqn. 4.20. This problem may

be written as a superposition of three subproblems, where $c_1 = c_{1,1} + c_{1,2} + c_{1,3}$. Solving the problem for $c_{1,1}$, which is given by omitting the forcing term $\partial_{xx} c_0$ from eqn. 4.19 and replacing eqn. 4.20 by $c_{1,1} = 1$ at $Y = 0$, one finds

$$c_{1,1} = -\frac{3^{1/3}}{\Gamma(1/3)} \int_{\zeta'=0}^{\zeta} e^{-\zeta'^3/9} d\zeta'. \tag{4.22}$$

Hence, the corresponding dimensional flux of ions is

$$i_{1,1} = -D\partial_y c_{1,1}|_{y=0} = D\frac{3^{1/3}}{\Gamma(1/3)} \frac{c_{\text{bulk}}}{\delta} \left(\frac{\text{Pe}}{x/\delta}\right)^{1/3}. \tag{4.23}$$

One can further write the problem for $c_{1,2}$ by omitting the forcing term $\partial_{xx} c_0$ from eqn. 4.19 and replacing eqn. 4.20 by $c_{1,2} = \cos kx$ at $Y = 0$. The problem is written as

$$Y\partial_x \tilde{c}_{1,2} = \partial_{YY} \tilde{c}_{1,2}, \tag{4.24}$$

$$\tilde{c}_{1,2} = e^{ikx} \text{ at } Y = 0, \tag{4.25}$$

and

$$\tilde{c}_{1,2} = 0 \text{ at } Y \to \infty. \tag{4.26}$$

using the complex variable $\tilde{c}_{1,2}$ whose real component is $c_{1,2}$. Using the transformation

$\tilde{c}_{1,2} = f(Y)e^{ikx}$ in eqns. 4.24–4.26 produces the alternate system of equations

$$ikYf = \frac{d^2 f}{dY^2}, \tag{4.27}$$

$$f = 1 \text{ at } Y = 0, \tag{4.28}$$

and

$$f = 0 \text{ at } Y \to \infty, \tag{4.29}$$

which is satisfied by the complex solution

$$f = 3^{2/3}\Gamma(2/3)\mathrm{Ai}\left((ik)^{1/3}Y\right), \tag{4.30}$$

where Ai is the Airy function of the first kind. The Airy function decays in the limit $Y \to \infty$ subject to the argument $(ik)^{1/3}$. The real component of the Y derivative of $\tilde{c}_{1,2}$ is given by

$$\partial_Y c_{1,2}|_{Y=0} = \frac{\sqrt{\pi}(3/2)^{1/3}}{\Gamma(1/6)} k^{1/3} \left(\sin(kx) - \sqrt{3}\cos(kx)\right). \tag{4.31}$$

Hence, the corresponding dimensional flux of ions is,

$$\begin{aligned} &i_{1,2} = -D\partial_y c_{1,2}|_{y=0} = \\ &-D\frac{\sqrt{\pi}(3/2)^{1/3}}{\Gamma(1/6)} \frac{c_{\text{bulk}}}{\delta} (k\delta)^{1/3} \left(\sin(kx) - \sqrt{3}\cos(kx)\right) \mathrm{Pe}^{1/3}. \end{aligned} \tag{4.32}$$

Finally, one can write the problem for $c_{1,3}$ using eqn. 4.19 and replacing eqn. 4.20 by $c_{1,3} = 0$ at $Y = 0$. The problem for $c_{1,3}$ gives a spatially monotonic solution and requires a numerical solution; however, this solution does not contribute to the leading order solution for the dendrite-free region of the electrode denoted by x_{crit}. Hence, we refer to the solution of this problem on the order of magnitude of $\mathscr{O}[\epsilon]$ as follows.

The total ion flux to the Li electrode is given by $i = i_0 + \epsilon(i_{1,1} + i_{1,2} + i_{1,3})$, which translates to

$$\frac{-i}{\text{Pe}^{1/3} D c_{\text{bulk}}/\delta} = \frac{3^{1/3}(1-\epsilon)}{\Gamma(1/3)} (x/\delta)^{-1/3} + \epsilon \frac{\sqrt{\pi}(3/2)^{1/3}}{\Gamma(1/6)} (k\delta)^{1/3} \left(\sin(kx) - \sqrt{3}\cos(kx) \right) + \mathscr{O}[\epsilon], \tag{4.33}$$

where we note again that $\epsilon \approx \text{Pe}^{-2/3}$. We further highlight that a similar problem and solution appear when where the value of ϵ is arbitrary while satisfying $1 \gg \epsilon \gg Pe^{-2/3}$, with the exception that the forcing term $\partial_{xx} c_0$ does not exist in eqn. 4.19, and hence the result given in eqn. 4.33 does not contain the third term on the right hand side of the equation, given as $\mathscr{O}[\epsilon]$.

4.4.1 Li^+ ion gradient within stationary electrolyte: $\beta = 0$

In the absence of flow, we find that the diffusion-limited flux of ions to the electrode, $-i$, is given by,

$$-i = D \left(\frac{2 c_{\text{bulk}}(1-\epsilon)}{L} - \epsilon c_{\text{bulk}} k \cos(kx) \right), \tag{4.34}$$

where the negative sign in front of i appears because the flux of ions to the electrode is along the $-y$ axis direction. The flux of ions is locally enhanced near the hotspots, suggesting the initial Li^+ ion concentration gradient and subsequent nonuniform Li^+ plating and dendrite growth is inevitable.

4.4.2 The effect of electrolyte flow, $\beta > 0$, on the Li^+ ion gradient

The presence of flow near the Li electrode enhances the advection of Li ions to the electrode in a manner proportional to $\mathrm{Pe}^{1/3}$, where $\mathrm{Pe} \equiv u_c l/D$ is the Peclet number.[128] In addition, we show that the flow further enhances the local transport of Li ions to the hotspots in a manner proportional to $\mathrm{Pe}^{1/3}$. This result is expected since the enhanced convection of ions along the electrode to the hotspots decreases variations in ion concentration that would otherwise arise. The overall rate of Li ion adsorption onto the electrode is given by

$$\frac{-i}{\mathrm{Pe}^{1/3} D c_{\mathrm{bulk}}/\delta} = \frac{3^{1/3}(1-\epsilon)}{\Gamma(1/3)} \left(\frac{x}{\delta}\right)^{-1/3} + \epsilon \frac{\sqrt{\pi}(3/2)^{1/3}}{\Gamma(1/6)} (k\delta)^{1/3} \left(\sin(kx) - \sqrt{3}\cos(kx)\right) + \mathscr{O}[\epsilon], \tag{4.35}$$

where we assume that $\epsilon \approx \mathrm{Pe}^{-2/3}$ (albeit similar result appears when requiring that $1 \gg \epsilon \gg \mathrm{Pe}^{-2/3}$), and note that $\Gamma(1/3) \approx 2.68$ and $\Gamma(1/6) \approx 5.57$. The first term on the right indicates the spatially monotonic convective contribution of ion flux to a flat homogeneous electrode and the second term indicates the correction to the spatially non-monotonic convective ion flux due to the presence of the hotspots. The third term given simply as $\mathscr{O}[\epsilon]$ is an additional convective contribution to the ion flux, which is spatially monotonic

and may be obtained numerically. We note that the first and third terms are products of similarity analysis and hence are mathematically singular at the origin, $x = 0$, and hence the expression for the current in eqn. (4.35) is physically valid far from the origin.

The mechanism by which flow inhibits the growth of dendrites is counterintuitive. The flow enhances the flux of Li^+ ions to the electrode and particularly to the hotspots where dendrites may grow, as given independently by the first and second terms on the right side of eqn. (4.35), respectively. The ion flux is spatially perturbed by ion depletion next to hotspots for the growth of dendrites, which is given in the second term in the equation. However, the leading order convection term, which decays like $x^{-1/3}$ along the electrode, eliminates localized ion flux maxima and hence is the key to the inhibition of dendrites' growth. The combined contribution of both terms eliminates localized ion transport maxima to the electrode and hence eliminates spatially localized growth spots—dendrites—on the electrode. But this suppression of dendrite growth is only over a finite length of the electrode from $x = 0$, where the shear flow (or alternatively the electrode) commences, to $x < x_{\text{crit}}$; as x grows, the second of the two terms in eqn. (4.35) becomes dominant and the hotspots at $x \geq x_{\text{crit}}$ will begin to allow dendrite growth. To determine this critical length, we require the slope of ion flux to not change sign with respect to x along the electrode, such that $d(-i)/dx < 0$, thus avoiding localized ion flux maxima along the electrode. Substituting eqn. (4.35) into the non-equality, replacing the spatial derivative of the term $\sin(kx) - \sqrt{3}\cos(kx)$ by its numerical upper bound, 2, and ignoring the second order ($\mathcal{O}[\epsilon]$) spatially monotonic contributions to ion flux along the electrode surface, thus comparing between the contribution of the leading order spatially monotonic

ion flux and the leading order (harmonic) contribution to the ion flux from the presence of dendrites, gives

$$x_{\text{crit}} = \left(\frac{6\epsilon k^{4/3}\beta}{\alpha}\right)^{-3/4} \approx 0.35\ k^{-1}\epsilon^{-3/4} \approx 0.35\ k^{-1}Pe^{1/2}, \tag{4.36}$$

where $\alpha \equiv 3^{1/3}(1-\epsilon)/\Gamma(1/3)$ and $\beta \equiv \sqrt{\pi}(3/2)^{1/3}/\Gamma(1/6)$. The correction to the ion flux due to the presence of hotspots in eqn. 4.35 and in our corresponding estimate of the dendrite free length of the electrode, x_{crit}, are qualitative results. Their quantitative magnitude is given from our requirement that the contribution of ion depletion (next to hotspots) to the ion flux appears in the first correction (of the order of $\epsilon \approx \text{Pe}^{-2/3}$) to the leading order ($O(1)$) convective result. Hence, x_{crit} indicates that the excitation of flow near the electrode inhibits the growth of dendrites but to a limited electrode length, which is dependent on the properties of the electrode. In particular, x_{crit} increases when reducing the density of hotspots and their intensity, that is, reducing the excess of ion depletion next to the hotspots. Alternatively, it is clear that increasing flow intensity further increases x_{crit}. The curious result here is that this length is independent of the specifics of the flow, but only if the Peclet number is significantly greater than one. Here, our means to ensure the Peclet number is sufficiently large is acoustic streaming, and thus we choose the characteristics of the SAW device and its operation to ensure the amplitude, frequency, and length scale of attenuation of the acoustic wave [129] are appropriately chosen to ensure sufficient flow and avoid nonuniform Li^+ deposition, porosity, and dendrites.

4.5 Conclusions

We have devised a chemistry-agnostic means for avoiding ion depletion and dendrite growth in liquid electrolyte batteries. Adopting small, high-frequency ultrasound generators to drive electrolyte flow within the inter-electrode gaps gives rise to ion flux distributions that render potential locations of dendrite growth stable within a specific distance from the ultrasound source. This distance is independent of the details of the flow as long as the Peclet number is sufficiently large. This is fortunately possible with the acoustic streaming induced by our ultrasound devices and make practical Li metal rechargeable batteries possible, even with rapid charge rates and the choice of electrode materials and electrolytes that would normally be considered unrealistic. The Li‖Cu configuration, as an example, was able to cycle until 6 mA/cm^2 current density with reasonable Coulombic efficiencies above 80% throughout. Moreover, the Li‖$LiFePO_4$ configuration can deliver 95 mAh/g capacity after 200 cycles at 2C charge and discharge rates. Dense plating of Li in both cell types was shown with SAW, and compared to the significant porosity and dendrites present in otherwise identical cells without SAW.

We anticipate a remarkable freedom in the choice of battery electrochemistry and operation to be facilitated from this simple technology, enabling greater efficiency, utility, and sustainability of rechargeable batteries for a broad swath of current and future applications.

Chapter 4, in full, is a reprint of material appears in Advanced Materials 2020. Huang, An; Liu, Haodong; Manor, Ofer; Liu, Ping, Friend, James., Advanced Materials 2020. The dissertation author was the primary investigator and author of this paper.

Chapter 5

Acoustic wave interaction with multilayer lithium ion battery

5.1 Introduction

Electric vehicles (EVs) require a long-sought combination of large capacity, long life, and fast charging to be a compelling alternative to internal combustion vehicles. The U.S. Department of Energy devised the eXtreme Fast Charging (XFC) program [132], supporting research and development from charging infrastructure [133, 134], the design of EVs [135], battery packs [136], and the content of the batteries themselves [137, 138]. They established aggressive goals for improving LIB technology, seeking to deliver batteries that charge from zero to full capacity in 15 min with an energy density of 200 Wh-kg^{-1} and less than 20% fade in capacity after 500 cycles. These goals, combined, lie well beyond several major technical barriers that have existed for decades [132].

Fast charging an LIB requires high current flow, associated with a significant voltage difference between the operating and Li^+-plating potentials [98]. This reduces the performance, life, and safety of the LIB, and leads to lithium plating of the graphite anode instead of intercalation, with undersirable side reactions and excessive heating that may grow to thermal runaway [139]. High-performance cells tend to use thin-layer or nanoparticle-based electrodes of eelctrochemically active media to minimize the diffusion distance [98]. The electrolyte is likewise tailored to improve the ionic conductivity and transport. Ion transport in the electrolyte underpins the charging speed of the LIB. Furthermore, the capacity of an LIB is limited by the ohmic potential across the electrolyte as the cutoff voltage is prematurely achieved during charging. Fast charging depletes the Li^+ ions adjacent the anode as the their diffusion from the cathode and through the electrolyte via the separator is too slow to keep up, leading to a pronounced Li^+ concentration gradient, heating, and inhomogneous Li deposition and plating [99].

A major barrier to fast charging is the ionic conductivity of the electrolyte. A typical carbonate electrolyte in LIBs is $LiPF_6$ in ethylene carbonate (EC):dimethyl carbonate (DMC) at a weight ratio of 3:7, with an ionic conductivity of 8.5 mS-cm^{-1} with 1 M $LiPF_6$ salt, which is sufficient for low charge rates of 0.1– 1C. However, at high charge rates, $>$ 3C, at least 13 mS-cm^{-1} is necessary to avoid undesirable chemical reactions [100, 5]. Adding aliphatic esters—for example, methyl acetate (MA) or ethyl acetate (EA)—improves the ionic conductivity and overcomes this barrier while introducing another: decreasing the cycle life of the LIB through the formation of an undesirable solid electrolyte interphase (SEI) layer on the graphite anode [101, 102]. Formate, nitriles, and amides have also been

considered [5], but poor compatibility with the LIB's cell chemistry reduces the Coulombic efficiency [5]. Notably, fluorethylene carbonate additive avoids these drawbacks, yet has one of its own: it is prone to defluorination by PF_5 produced from the $LiPF_6$ in the electrolyte [103].

Beyond chemistry, other means to increase the charge rate have been attempted. Exposure of the cathode to white light produces additional Mn^{4+} oxidation sites, improving charge transport [104]. External magnetic fields have been applied to produce electrolyte flow via magnetohydrodynamics: a Lorentz force on the ions in the fluid electrolyte produces spiral-like flow, improving ion convection and helping to overcome the concentration gradient during fast charging. Unfortunately, magneto-hydrodynamics is extraordinarily inefficient [105].

Acoustic waves have been used as well, though mainly for sensing. [140] pioneered the use of pulsed ultrasound (US) transmission and detection to detect pouch cell degradation between the electrodes. [141] used a small piezoelectric transducer mounted on the outside for this purpose, employing instead a modulated sine wave to detect porosity and other morphological problems within the battery. [142] used pulsed 2.25 MHz US to detect lithium plating on the graphite anode. So far, the sole study on using acoustics as an actuator to enhance charging performance in batteries was the use of 100 MHz surface acoustic waves (SAW) in prototype lithium metal batteries [143]. In other contexts, high frequency US at 10–1000 MHz has been used to generate fluid and particle flow in micro to nanoscale confined structures somewhat analogous to the internal structure of batteries [16, 51]. We now integrate a SAW device into multilayer, nominally 2 Ah Li ion pouch

cells. These cells are made using standard graphite anodes, $LiNi_{0.5}Mn_{0.3}Co_{0.2}O_2$ (NMC532) cathodes, and EC:DMC at 3:7 v/v as our electrolyte. This carbonate electrolyte is widely known to be a poor choice for fast charging, and—with the use of some technique—if a battery using this carbonate electrolyte can be shown to have good performance with fast charging, it may indicate other rechargeable batteries can benefit from the same technique [100]. Using SAW in this cell, we demonstrate the ability to avoid Li plating during fast (15 min) charging with SAW through electrochemical measurements, examination of the morphology via scanning electron microscopy (SEM), x-ray diffraction (XRD), energy-dispersive x-ray spectroscopy (EDX), and visual inspection of the LIB's components after disassembly. We further examine the LIB without disassembly using neutron diffraction. Throughout, we use pristine uncycled and no-SAW LIBs as controls. Altogether, integrated SAW appears to be an effective method to overcome the myriad barriers to fast LIB charging.

5.2 Experiment methods

5.2.1 Cell and SAW device fabrication

The 1.8 Ah LIB pouch cells are composed of NMC532 as cathode and graphite as anode. The composition of cathode was NMC532: CNT:PVDF = 100:1:1.5 with mass loading of 36.2 $mgcm^{-2}$, 2.99 $Ahcm^{-2}$ areal loading, and 40% porosity. While the anode was composed of a combination of different carbon-based material of C:CMC:SBR:S-P = 94.5:1.5:3:1, results into a mass loading of 17.5 $mgcm^{-2}$, 3.2 $Ahcm^{-2}$ areal loading, and

30% porosity. Commercial grade 1M solution of lithium hexafluorophosphate ($LiPF_6$) in a 3:7 (w/w) mixture of ethylene carbonate (EC) and Dimethyl carbonate (DMC) (BASF) was used as the electrolyte.

The SAW device was fabricated through lift-off lithography to deposit twenty-eight pairs of unweighted Au/Cr fingers and form an optimal[51] interdigital transducer (IDT) onto a 500 μm thick 127.68° Y-rotated, X-propagating cut lithium niobate substrate ($LiNbO_3$ (LN), Roditi).[15, 117] The SAW device was then coated with parylene C using chemical vapor deposition (PDS 2010 parylene coater system, Specialty Coating Systems) to prevent reactions with the electrolyte [143]. Electrolyte were injected into the baseline LIB and SAW integrated LIB inside an argon-filled glovebox (MTI Corporation), followed by de-gas and final sealing (MTI). The moisture level and O_2 level were both <1 ppm.

5.2.2 Electrochemical measurement

Electrochemical studies were carried out in the 1.8 Ah pouch LIB, placing the SAW device within the cell perpendicular to the electrode gaps. The battery was underwent a formation cycle at constant current-constant voltage (CC-CV) mode, to use constant current at 0.1 C rate to charge to 4 V and then adapt constant voltage step to charge till the current is smaller than 0.01 mA. After the formation cycle, the cell was then de-gased in the glovebox and resealed for further testing. From the second cycle, the battery was charged and discharge at CC modes.

5.2.3 Morphological characterization

The cycled batteries were disassembled inside an argon-filled glovebox, we first use optical imaging to scan the surfaces of the electrodes. And then cut out the represented areas to further perform scanning electron microscopy imagining (SEM Quanta 250, FEI Corp.). The electrode samples were rinsed with dimethyl carbonate (Sigma-Aldrich) to remove the residual electrolyte on the surface of the electrode. And then attached to a specimen holder (Ted Pella) using double-side carbon tape (Ted Pella) and sealed within an aluminized polyethylene bag inside the glovebox for transferring samples to the SEM. After transport to the SEM, the samples were quickly transferred from the bag to the scanning electron microscopy vacuum chamber (SEM Quanta 250, FEI Corp.) for imaging at 5 kV. The samples were exposed to air for less than three seconds.

5.2.4 Crystalinity characterization

The structural properties of the samples were characterized by X-ray diffraction (XRD) (model number and brand) with a monochromatic Mo Kα radiation source ($\lambda = 0.15406$ nm). XRD patterns were collected in the range $10 < \theta < 80^{\circ}$ with a step size of $2\theta = 0.05^{\circ}$ and a count time of 12 s per step.

Furthermore, we adopt neutron diffraction to analyze post-cycled batteries after 250 cycles with 15 mins charge time and 3 hours discharge time. The neutron diffraction was performed at Oak Ridge National Lab.

5.3 Results and discussion

5.3.1 Electrochemical performance of 1.8 Ah Li ion pouch cell cycle performance with SAW device

The electrochemical performance are tested on pouch cells formats due to its manufacturing flexibility in commercial production. The baseline cells are composed of graphite as anode and lithium nickel manganese cobalt oxide 532 (NMC 532) as cathode with 1 M $LiPF_6$ in EC/DMC electrolyte. For a SAW integrated LIB (SAW LIB), a SAW device was carefully integrated into a pouch cell.

To understand the battery performances, we first test the rate capability performances on both of the cells. The tests are started from cycling at low current density of 0.1 A (20 hours charge and discharge time) to high current density of 5 A (10 mins charge and discharge time). The results are shown in Fig. 5.1. It is shown that at slow charge rate (0.1 A), both of the cells can deliver 1.8 Ah discharge capacities. However, at higher cycle rates, the discharge capacity discrepancies between the two cells became obvious. At 5 A cycle rate, a 55% discharge capacity is able to generate compare to the 0.1 A charge rate, while it is only 27% for a baseline cell. Moreover, at the first cycle of 5 A cycle rate, the SAW LIB can deliver 45 % more capacity than the baseline cell (0.9 Ah for a SAW LIB vs. 0.5 Ah for a baseline cell).

The differences between the cycling behaviors of the two cells is revealed by their individual cycle profiles as shown in Fig. 5.1 b. and c. for baseline cell and SAW LIB,

respectively. A increased polarization and unstable cell capacity loss at each individual cycle at different current densities is shown for a baseline cell. While a stable cycling performance is shown with limited cell polarization changed was shown for the cycles at the same current densities is shown for a SAW LIB.

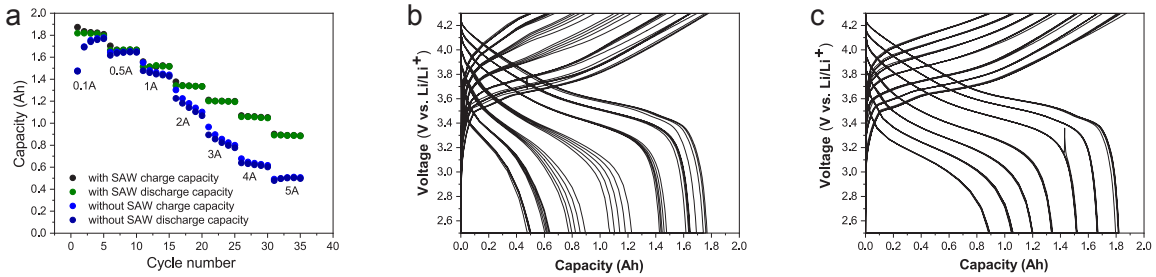

Figure 5.1: **Electrochemical performances of baseline cell and SAW LIB at different cycle rates a** Charge and discharge capacities of the baseline (blue (charge) and dark blue (discharge)) and SAW LIB (black (charge) and green (discharge)) are plotted versus the cycle numbers with progressively current densities of 0.1, 0.5, 1, 2, 3, 4, to 5 A. The charge and discharge voltage profiles of a baseline cell is shown in **b,** and likewise for the SAW LIB **c**.

Moreover, we examine the long term cycling performance of a baseline cell and SAW LIB cycle at high current density of 5 A (equivalent to 10 mins charging and discharge time) over 2000 cycles with cut-off voltages of 2.5–4.2 V. The results are shown in Fig. 5.2. Fig.5.2a shows the discharge capacity over 2000 cycles. It is clearly shown that the SAW LIB has superior cycle performances with regards to the better discharge capacity and stable cycle performances throughout. With SAW, the LIB offers 0.9 Ah capacity at initial cycle while only loses 20 % capacity to 0.72 Ah at 2000 cycle. On the contrast, the baseline cell only offers around 50% of the capacity compare to a SAW LIB of 0.42 Ah at the initial cycle and then decays to almost zero capacity at 200 cycles.

The effect of SAW is further apparent in a comparison between the individual charge and discharge voltage profiles of the baseline LIB in Fig. 5.2b and the SAW LIB in Fig. 5.2c, respectively. The polarization effect increases dramatically with the number of the cycles in the baseline cell, while stable cell voltages were shown in the SAW LIB. The unstable polarization effect is an indication of Li platting, electrolyte consumption of a battery. And therefore, the results indicates the achievement of stable cycle performance using SAW.

5.3.2 Post-cycle morphology change

We disassembled the cycled cells for optical analysis to visualize the morphology change. The images of disassembled cells are shown in Fig. 5.3. Fig. 5.3 a–d (left column) are the cycled components from a baseline cell, while the Fig. 5.3 e–h are the cycled components from a SAW LIB. We first found that the morphology change for the cathode electrodes are limited from both baseline cell (Fig. 5.3 a) and SAW LIB (Fig. 5.3 e). t is due to the degradation of cathode is usually performed in the micro-structure or micro-morphology, which will be discuss in the later section. However, the separator that faced the cathode from a baseline cell shows material deposition (brown and white deposition) from a baseline cell (Fig. 5.3 b). While clean morphology is shown from a SAW LIB (Fig. 5.3 f).

On the other hand, the differences of the surface morphology is quite clear from the anode electrode. The anode from a baseline cell (Fig. 5.3 c) shows severe Li deposition, materials cracking, and material pealing off, which are indications of anode degradation. Compare to the anode from a cycled SAW LIB (Fig. 5.3 g), showing close to pristine, clean morphology throughout. Likewise, the separator that facing toward the anode shows

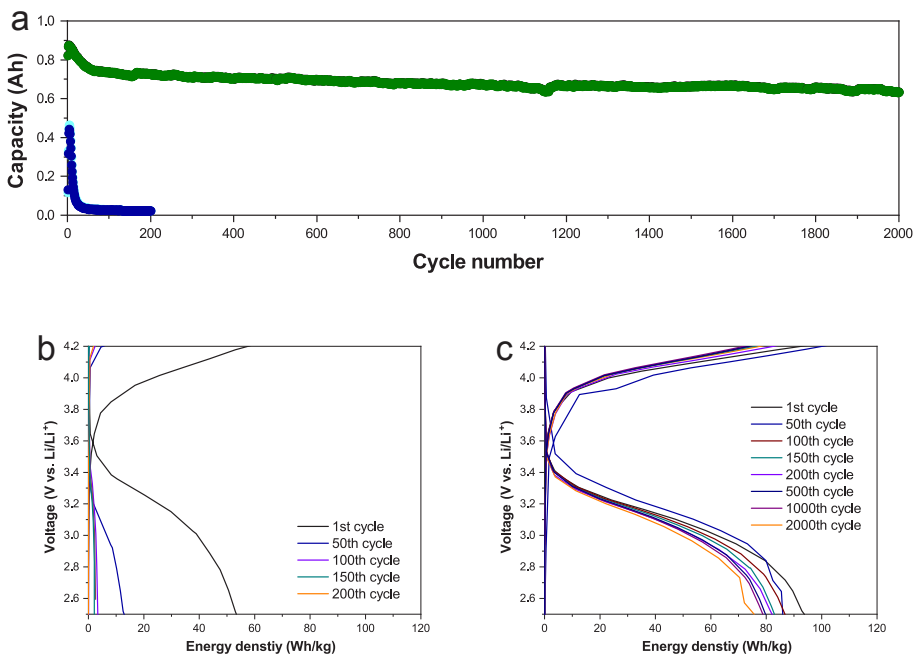

Figure 5.2: **Long term cycle performance of a LIB that cycled with SAW and without SAW.** Both of the cells are cycled at galvonostatic mode with 5 A charge and discharge currents (equivalent to 10 mins charge and discharge time). The cut off voltages are 2.5–4.2V. **a,** Discharge capacities with respects to different cycle number from the baseline cell (light blue and dark blue) and SAW LIB (green and black). **b,** Voltage profiles of selected cycles of 1, 50, 100, 150, and 200 from a baseline cell, likewise **c,** 1, 50, 100, 150, 200, 500, 1000, and 2000 cycles for a SAW LIB.

similar trend as the anode material. The white and brown deposition shows on the surface of the separator for a baseline cell (Fig. 5.3 d), while limited morphology was changed from a SAW LIB (Fig. 5.3 h).

Moreover, part of the representative areas from the electrodes are taken for SEM/EDX analysis. Dendritic-like morphology is present on the anode that cycled from a baseline cell

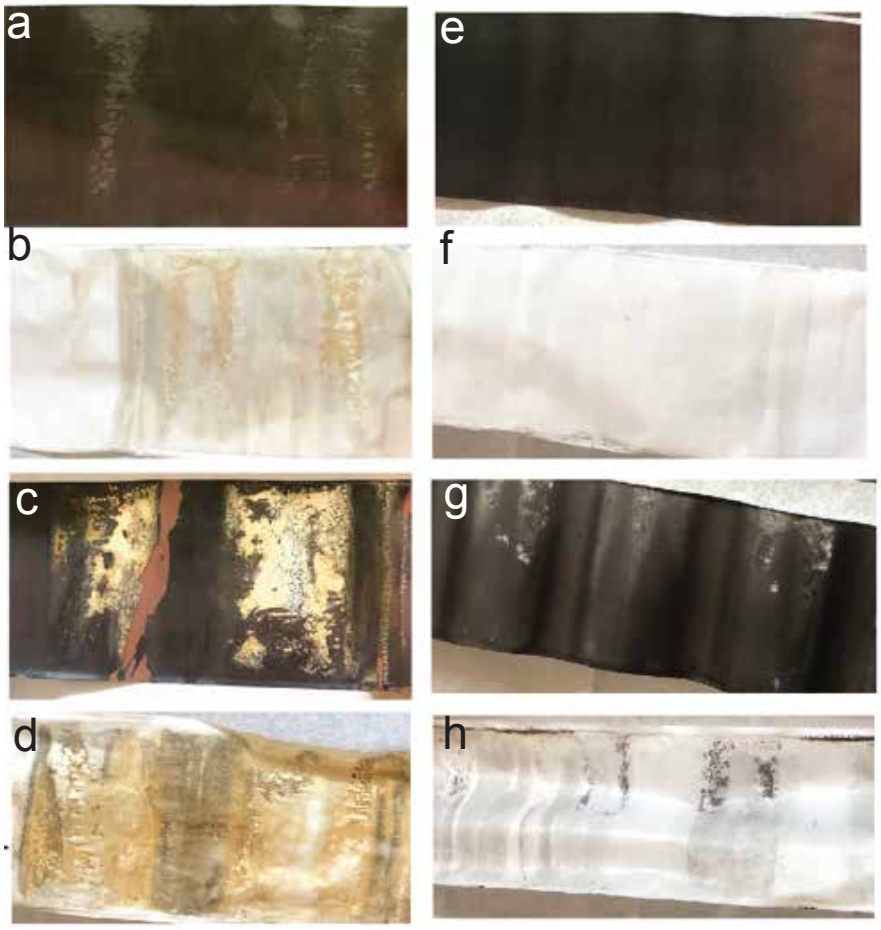

Figure 5.3: **Optical images to show the morphology change from cycled LIB cells.** The left columns represents **a,** cathode, **b,** cathode separator, **c,** anode, and **d,** anode separator from a baseline cell. While **e, f, g, h,** are cathode, cathode separator, anode, and anode separator from a SAW LIB.

(Fig. 5.4a,b). The dendrite deposition on the graphite anode comes from the sluggish Li transportation and results into the ions are not intercalacted into the graphite structure but deposit on the surface instead, resulting into irreversible capacity, short circuiting, and safety issues. This is an indication of limited material degradation from an anode material. On the contary, large particle, chunck-like morphology remains on the surface of the anode that cycled with SAW (Fig. 5.4c,d). This morphology is believed to be pristine

graphite morphology. Moreover, the EDX results indicate the ratio of elements C:F:O from a baseline cell is 1:0.31:0.2, while 1:0.16:0.1 for a SAW LIB cell. The smaller percentage of the F and O from a SAW LIB cell shows the lesser the solid state electrolyte interphase (SEI) is formed compare to a baseline cell. It is a further indication of the Li dendrite deposition associate with material degradation [144].

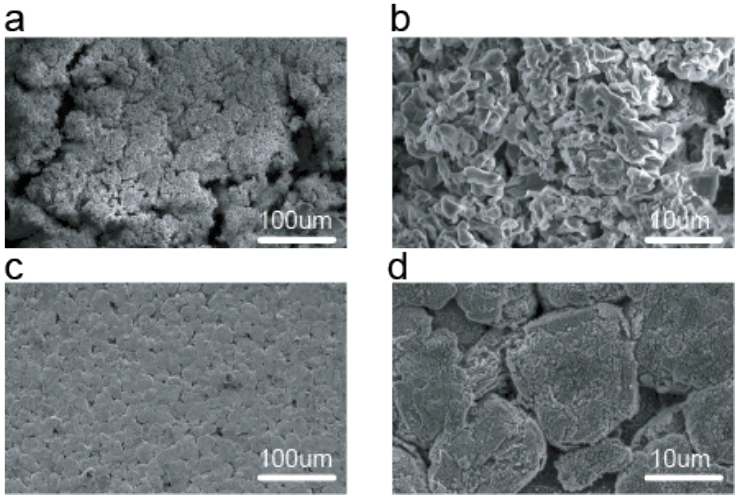

Figure 5.4: **SEM images on the cycled anode electrode from a baseline cell and SAW LIB. a,** Anode morphology from a cycled baseline cell, dendritic-like structure is shown on the surface and **b,** is the zoom in image of the **a**. While **c,** is the anode morphology from a cycled SAW LIB cell, likewise the **d,** is the zoom in image from **c**.

Post-cycle micro-structural change of the electrodes

We further examine the microstructral change from the anodes from pristine uncycled cell, cycled baseline and cycled SAW LIB through XRD, respectively (Fig. 5.5). For the pristine anode, there is a peak at 27°, which is the representative peak for graphite LiC_6 (100) plan [145, 146]. We further performed the XRD analysis on the anode with two positions: the first position was at the severe deposition area (green line, where the brown

and white deposition was shown on the anode surface), while the second position was at the black area (blue line). For the brown/white area, the peak becomes much less intense, suggesting less crystallanity of LiC_6. While a peak shows up at 26 $^\circ$, suggesting a new phase formation. The new phase may be a distorted carbon contents in the LiC_6, potential a LiC_{12} phase [142]. The peak is less sharp and broaden compare to the pristine electrode, indicating the spacing of the atoms are increased and less crystallanity. Moreover, for the black area from a baseline cell. The peak shifts to a lower angle, indicating the distortion of the LiC_6 phase with a potential LiC_{12} formation.

On the other hand, for the anode from a SAW LIB, the XRD peaks remain in the same angular positions as the pristine sample. Notably, these same results were found in samples closer to the SAW and farther away from it. This is an indication that the SAW is serving to maintain the anode's state throughout the battery.

The similar effects were also found from the cycled cathodes (Fig. 5.6). It is shown that the major peaks (003), (104), (101), (006), (102) are remained at the same scatter angles for the cathodes after cycling with SAW no matter with the position of a SAW device. However, this is not the case for the cycled cathode sample taken from a baseline cell. The peak positions of the (003), (006), and (110) orientations have either shifted or disappeared. The (003) and (110) planes are shifted, which are associated with lose of active Li. The peak shifting, broadening, or disappearing are an indication of the lattice structural change of the cathode material, resulting into strain change and material degradation of the baseline cell. While those effects were not observed from a cathode that cycled with SAW, suggesting the cathode degradation was prevented when a SAW device

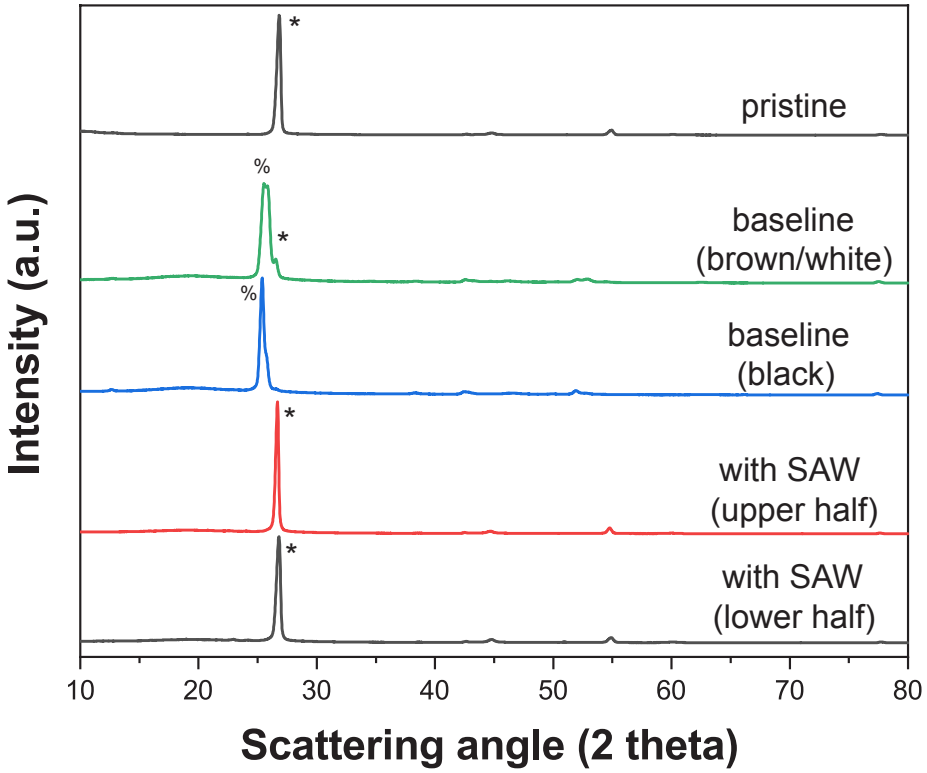

Figure 5.5: **XRD images from anodes from pristine, uncycled anode and from cycled baseline cell and cycled SAW LIB.** From top to bottom are the anode from pristine cell, baseline cell (black and white dominant region), baseline cell (black dominant region), upper region from a SAW LIB, and lower region from a SAW LIB. $*$ represents the LiC_6 phase, while % represents the LiC_{12} phase.

was adopted.

To understand the effects of the SAW device to a LIB, we performed neutron diffraction analysis to thoroughly understand the effect of SAW on the different positions of a LIB. The cells that used for the neutron diffraction analysis were cycled after 250 high-rate charging cycles (15 mins charge time) and C/3 slow discharge rate with and without SAW during charging. The cells were taken to the neutron analysis at the fully discharge state. A scheme illustration of a cell positioned and the scanned point numbers are shown in

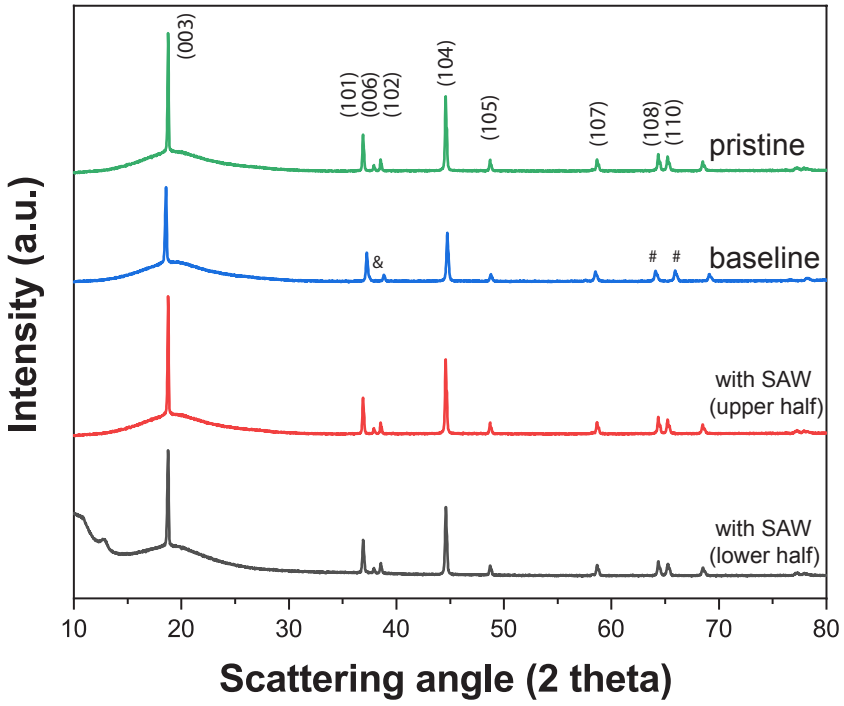

Figure 5.6: **XRD images from anodes from pristine, uncycled anode and from cycled baseline cell and cycled SAW LIB.** From top to bottom are the anode from pristine cell, upper region from a SAW LIB, lower region from a SAW LIB, and from a baseline cell. The & represents the missing (006) phase from the baseline cell, while # shows the distortion in peak angle of the (108) and (110) phases from the baseline anode.

Fig. 5.7a.. For the baseline cell, there is no SAW device integrated in the battery and there are 10 data points that were collected during the test. For a cell that integrated with a SAW device, the 10 points that were collected are at the same position of a baseline cell. While the point 5 and 10 are the closet points to the acoustic source and point 1 and 6 are the furthest away from the acoustic source.

The mapping results are shown in Fig. 5.7b., c., and d., representing of pristine cell (that is without any cycles), baseline cell after 250 cycles, and SAW LIB after 250 cycles, respectively. The cathode signals representing (110) and (108) phases are clearly shown in

the pristine cell (Fig. 5.7b.) While large variation and distorted of the phases are shown for a baseline cell (Fig. 5.7c.), indicating severe materials were degraded after the cycling of a cell. On the other hand, the two phases are still clearly been shown in a cycled SAW LIB cell. This indicates a less material degradation of a cell, leading to the stable cycling performances.

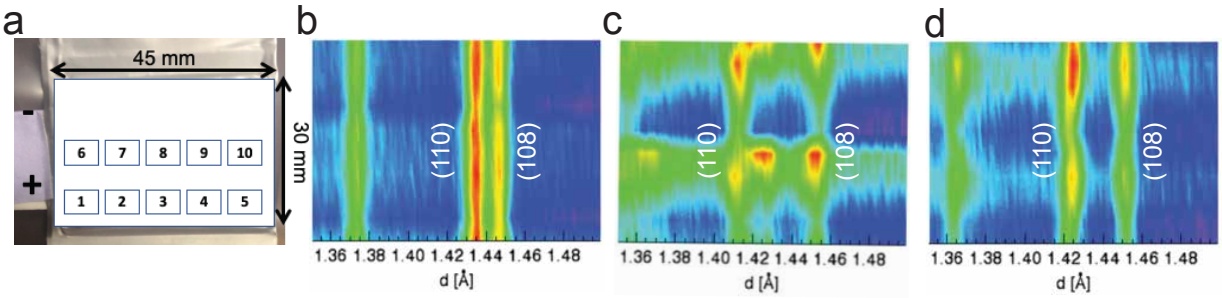

Figure 5.7: **Neutron diffraction results of the LIB at pristine stage, after cycling without SAW, and cycled with SAW. a,** shows the scanned points on a LIB, SAW device is integrate at the opposite site of the current collectors and therefore the point 5 and 10 are closet to the SAW device, while point 1 and 6 are the furthest away from a SAW device. **b,** mapping results of a pristine, uncycled LIB. **c,** cycled baseline cell and **d,** cycled SAW LIB cell.

Moreover, the change in the lattice parameter were analyzed. We first examine the c lattice parameter from a cathode. It is shown that the c lattice parameters has an average of 14.225 A at pristine stage, while the average of c lattice distance is 14.4309 (standard deviation 3.8 %) and 14.3758 (standard deviation 0.6 %) for the baseline cell and SAW LIB, respectively. It also indicates the baseline sample's lattice is expanded 1.426 % away from the pristine sample, while it is 0.92 % for the SAW LIB case. The differences between the two samples are 35.17 %.

On the contrary to the c lattice expansion, the a lattice shows reductions for both of the samples. The average of the a lattice for a pristine sample is 2.87 A, while it is 2.8477

(standard deviation of 2 %) for the SAW LIB and 2.81 (standard deviation of 10 %) for baseline cell. It suggests the a lattice reduced a 2 % of a baseline cell compare to a 0.7 % reduction of a SAW LIB cell, generating a 64% differences between the cases.

Combining the c lattice and a lattice changes of the samples. The results suggest that the Li loss is more severe in the cell that cycled without SAW. Moreover, it is shown that the cathode degradation is much slower and more uniform in a cell with SAW integrated.

The lattice parameter change were also investigated on the anode. It is shown that the average c lattice length is 6.71 A from an uncycled pristine cell. While the c lattice lengths are increased for both cycled cells and shows an average of 6.7312 A (σ = 0.5%) and 6.7107 A (σ=0.1%) for the cells cycled without SAW and with SAW, respectively. It indicates a 96% differences between the two cases, where the baseline cell shows 0.3% in the c lattice length differences compare to the uncycled pristine cell while only 0.01% of the differences is shown for a SAW LIB.

Moreover, the a lattice were analyzed. It is shown that the average a lattice length of a pristine, uncycled cell is 2.87 A. While it is 2.4608 A (σ=0.06%) for a baseline cell and 2.46013 A (σ=0.009%) for a SAW LIB. It is shown that a 0.03 % differences is shown in a baseline cell compare to a pristine cell, while a 0.005 % for a SAW LIB, making a 83 % differences between the two cells. The results is also correlated with the Wilcoxon rank-sum test (p=0.0012) that the differences is significant.

5.4 Conclusions

A lithium ion battery's maximum charge rate and energy density are intrinsically limited by the ion diffusion rate in the electrolyte. Most research focuses on materials science solutions to this problem, with but gradual improvement over the years. We instead propose a mechanical solution: to integrate a MHz-order frequency surface acoustic wave (SAW) device into an existing 1.8 Ah multilayered Li ion pouch cell to enhance the ion diffusion rate and the overall battery performance. Both the charging rate and cycling lifetime are improved from SAW. At a 5C charge and discharge rate, integrating SAW into the Li ion doubles the energy density and maintains at least 80% of the battery initial capacity after 2000 cycles. Moreover, using SAW quantifiably reduces battery degradation in these conditions as determined from optical imaging, scanning electron microscopy, x-ray diffraction, and neutron diffraction. The use of SAW appears to offer a method to avoid undesirable Li ion plating on the graphite anode during charging, and leads to much longer battery lifetime and good charge capacity despite rapid charging.

Chapter 5, in part, is a reprint of material that is in preparation for submission 2020. Huang, An; Liu, Haodong; Liu, Ping, Friend, James. The dissertation author was the primary investigator and author of this paper.

Chapter 6

Practical Microcircuits for Handheld Acoustofluidics

6.1 Introduction

The challenge to deliver a miniaturized solution to driving acoustofluidics devices has eluded the research community for over 25 years. The knowledge and know-how required to design MHz-frequency, high-power driver circuits in a small package is surprisingly rare among the many advancements in microelectronics technologies over the past 75 years, and is constraining progress in research and development of acoustofluidics as a potential method for delivering effective lab-on-a-chip devices into commercial and clinical use. The original use of surface acoustic wave (SAW) devices in microfluidics [147] resulted in the formation of a company, Advalytix AG, eventually owned by Becton & Dickinson focused on SAW-driven fluid mixing at small scales, yet the drivers for this commercial

product were both mains powered and large. Other, occasional reports of success have been claimed, only to learn that power wires were hidden in a sleeve for a "handheld" driver, or that the circuit fails after only a short time[148]. Several attempts to completely avoid the problem of MHz-order acoustofluifdics have been attempted with lower frequency devices and corresponding driver circuits. Bachman *et al.*[149] produced an acoustofluidic system based on a cell phone and an audio speaker, but this scheme is limited to ¡30 kHz. They also developed a system based on an Arduino and a motor controller, but this only increased the upper frequency limit to 65 kHz[150]. While useful, the long wavelengths of these low frequency devices are not suitable for microfluidics that define most lab-on-a-chip technologies, and there is the potential for cell and molecular damage from such low frequency acoustics.

This paper aims to provide the first comprehensive microcircuit design capable of reliably driving the vast majority of acoustofluidics devices at 1–300 MHz, including the strategy and details necessary to help the reader to build their own driver circuits for lab-on-a-chip acoustofluidics.

Acoustofluidic devices are ideally suited for point-of-care and lab-on-a-chip applications, as they are small and produce ample mechanical power that can be harnessed to transport fluids and suspended objects. When alternating current (AC) signals are applied to piezoelectric transducers used in these devices, the resulting acoustic waves produce direct forces at boundaries with acoustic impedance changes and acoustic streaming from the attenuation of the acoustic wave in the fluid and within the viscous boundary layer. In doing so, acoustofluidics offers the following advantages over other approaches: (i) the forces

formed from high frequency acoustic waves overcome surface and viscous-mediated forces that tend to dominate in microfluidics, (ii) acoustic waves enable label-free, non-contact particle manipulation at small scales, and (iii) the AC signals that directly drive these devices offer precise control and simple operation. Fluid mixing, droplet manipulation, particle manipulation, and atomization have all been demonstrated with acoustofluidic technology and helped overcome medical and diagnostic challenges[18, 151, 51]. However, the majority of these solutions have not found practical use because they are unable to be adapted to miniature, portable devices. They still require laboratory equipment including signal generators, amplifiers, and oscilloscopes.

Many point-of-care devices and all drug delivery and disease evaluation technologies must also avoid damaging biological samples. The absence of damage to biological molecules and cells has been shown repeatedly in high frequency acoustic devices[152, 1, 153], but lower frequency acoustic waves, on the order of 10 kHz, are known to cause cavitation[154] that can damage cells, proteins, and antibodies, even—for example—in modulating higher frequency acoustics devices[148].

To highlight the capabilities of our circuit design for enabling lab-on-a-chip concepts and work, we will demonstrate four acoustofluidics devices that utilize our microcircuit. We will first demonstrate quick mixing in a sessile drop using a surface acoustic wave (SAW) device driven by our microcircuit. The Reynolds number, $\mathrm{Re} = \rho u D/\mu$, must be large for the turbulent flow that characterizes mixing, and it scales with the length scale of the device, D, so that it is very difficult to generate mixing at the microscale. The earliest broadly known lab-on-a-chip application of SAW devices solved precisely this

problem[155]. Very high frequency acoustic waves transmitted into fluids in contact with these SAW devices lead to large accelerations that easily mix a broad range of fluids from glycerol to whole blood [156, 116, 157].

We next demonstrate tunable alignment of 2 μm particles with SAW of 40–80 MHz, another key application of acoustofluidics in lab-on-a-chip applications. The spacing between groupings of particles aligned using standing waves is determined by their frequency[158]. Furthermore, The ability to manipulate small particles with acoustic transducers[159] depends on the wavelength of the acoustic waves they generate.

Similarly, the isolation and manipulation of medically relevant particles—cells, organelles, biomolecules—with acoustofluidic devices[160] requires frequencies beyond 10 MHz. We demonstrate separation of 38 μm and 4 μm diameter particles in a sessile drop as an analog to blood sample separation.

These three SAW based applications are each demonstrated using the same handheld driver circuit, named the *SAW board*, reprogrammed for each case by quickly uploading code from a computer. This board is relatively large—the size of an open hand—and is plugged in to wall power, convenient for prototyping, testing, and saving data.

In the fourth case, we demonstrate a high power application, a nebulizer driven by a handheld, battery powered circuit. This circuit, named the *TM* (thickness mode) *board* is designed using the same principles, but is optimized in parts and layout to be a compact, near-commercial circuit design. Nebulization is accomplished at practically relevant flow rates from battery power using this circuit and the board comes pre-loaded with a program to run a simple user interface. Acoustofluidic atomization of therapeutic liquids has the

potential to replace other forms of nebulization because of the aforementioned biological compatibility and the proven ability to produce droplet sizes in the range for optimal delivery to the lungs[161, 162, 163]. Our circuit enables these benefits in a handheld device.

6.2 Circuit design for acoustofluidics

To suit the signal generation needs of acoustofluidics devices while offering the portability required in clinical and commercial applications, a driver circuit must be miniaturized, battery powered, and able to produce signals in the 1–300 MHz frequency range with a power of 50 mW to 2 W, based upon most of the past published work in this discipline[51, 52, 164, 165].

Benchtop equipment—signal generators, DC power supplies, and low-frequency (LF) to radio-frequency (RF) amplifiers—is simply too expensive, bulky, and heavy for use outside of research laboratories. Miniaturized electronics tailored to an application may be achieved using commercially available *off-the-shelf* electronic parts assembled on custom-designed printed circuit boards (PCB). Because of the unique power and frequency requirements of acoustofluidics devices, significant design, programming, and testing efforts are required, but nonetheless can produce compact and user-friendly devices.

We accomplish this by applying electronics design principles to develop two distinct driving circuits, the TM board for 1–25 MHz thickness mode (TM) transducers, and the SAW board for 30–100 MHz SAW transducers. The TM board is compact, as it is intended

for battery-driven handheld nebulization. The SAW board was originally developed to drive SAW within prototype lithium batteries[143] on the lab benchtop. Consequently, the SAW board is larger for convenience, requires less power, operates at a higher frequency range, and draws power from a wall outlet. It also has additional circuitry on the board used for charging and other purposes not relevant to the work reported in this paper. Here, we use the TM board to illustrate how the reader may make practical handheld driver circuits for acoustofluidics sufficient to even drive atomization. We use the SAW board to demonstrate three other acoustofluidic applications showcasing the adaptability of this circuit design. With some effort, the reader should be able to construct a prototype circuit such as the SAW board for their needs, and once a specific application is identified, a much smaller prototype driver like the TM board may then be produced.

6.2.1 Circuit blocks

Despite the differences in the required stimulus frequencies and power levels, electrical driver systems for acoustofluidic devices incorporate five basic units or *blocks*.

1. **Stimulus generation**: This is accomplished by semiconductor circuits known as *phase locked loops* (PLL), a type of frequency synthesizer. This low-cost solution uses a reference crystal oscillator to produce a highly accurate and stable tone. The frequency is programmable over a specified range with very fine resolution, in this case ¡0.01 MHz. However, unlike the benchtop signal generators or arbitrary waveform generators (AWG) it replaces, the output amplitude is usually fixed; PLLs typically

cannot produce the required output power to directly drive the SAW devices. This leads us to the next circuit block.

2. **Amplification**: We employ a chain of amplifiers to connect the output of the PLL to the input of the SAW device, achieving increasingly higher voltage swings as needed. Furthermore, duty cycle control can be added using the enable signals of clock buffers, while attenuators—using dedicated chips or a simple resistor voltage divider—can be used to fine-tune the signal swing, and a power amplifier with a push-pull output stage can be employed to efficiently deliver high current at fixed voltage to the device. The device itself can be modeled as a low impedance load at the resonance frequency.

3. **Power management**: From a single battery or a wall outlet, the power management unit (PMU) produces all voltage supplies (such as 3.3V, 5V, 24V etc.) as required by various semiconductor chips on the PCB. These circuits are commonly known as *DC-DC converters*. *Boost converters* are used to step-up voltages from input to output, while *low dropout* (LDO) regulators step-down voltages. If higher efficiency is required, a step-down function can also be achieved using a *buck converter*. This block replaces a typical benchtop power supply.

4. **Impedance matching**: In a typical bench top setup, maximum power transfer is achieved when the load impedance matches that of the source (signal generators, amplifiers, and cables are typically 50Ω), otherwise some fraction of the power is reflected at the impedance interface. Based on a simple source/load model, the power

dissipated by the load is $P_l = V_s^2 R_l/(R_s+R_l)^2$. However, our boards utilize a constant voltage operational amplifier, so that there is no source impedance with which to match the load impedance. In this case, power transfer, $P_l = V_s^2/Z_r$, is maximized by minimizing the load impedance, $Z_l = Z_r + iZ_i$, where the real impedance, Z_r, is resistance and the imaginary impedance, Z_i, is capacitive if positive and inductive if negative. At a resonance frequency $Z_i = 0$ by definition and we can minimize Z_r by choosing the resonance frequency with the smallest resistance (this is done automatically on our boards as will be explained in the next section).

An impedance matching network is effective at reducing the reflected power in a typical bench top setup or in a circuit with a source impedance. Such networks do impose a power loss, so the system must be optimized to account for this trade-off. Qualitative examples and additional tips on electrical design are provided by Winkler et al., who show that impedance matching networks can result in a 30% improvement in acoustic performance (in terms of streaming velocity)[166]. In contrast, the power to the transducer in our circuit could be increased by lowering the effective load resistance. Our boards have designated spots for an impedance network, but they have not been populated because the power transfer was already good enough for demonstration purposes.

In commercial acoustofluidic products, it will be necessary to measure the impedance of the transducer in the condition it will be used (i.e. within the driver circuit and with realistic mechanical contact while loaded as it would be during the intended

operation) and then populate an impedance matching network based on the measured impedance at the intended frequency. For a transducer intended to operate only at one frequency, the simple network designed into our boards or an inductor/capacitor impedance matching network in the case of a more typical set-up is sufficient. Kim et al. utilized an impedance matching network and showed that it leads to more efficient production of acoustic pulses for cell actuation[167]. For multi-frequency applications more complicated networks are required. Vivek Rathod has covered these and other related topics at length in a recent review[168].

5. **Control and user interface**: A micro-controller unit (MCU), such as the *Arduino Nano* (Arduino LLC, Boston, MA USA), serves as the interface between the electronic driver system and the user. Through general-purpose integrated circuit (I^2C) input-output (IO) expanders, the MCU translates user inputs into low-level digital signals to control all components on the PCB. The MCU can be connected via USB to a laptop for convenient programming and testing flexibility. It may also be pre-programmed with a few options—such as power on/off, frequency up/down—that are selected by onboard push buttons connected to the MCU. As a result, the final SAW-based system may be turned into a completely self-contained and user-friendly device.

6. **Sensing and feedback**: While the electronics described above are already sufficient to drive the SAW device, we can take advantage of modern electronics to offer additional features. For example, one can include thermistors to monitor the board

temperature in strategic locations to detect overheating or out-of-design operation. Digitized and read by the MCU, the measured data can be used to simply monitor the operating conditions or to act on the data via a feedback loop, for example, to automatically shut down when a component overheats. As will be discussed below, our systems incorporate current sensors on the SAW device inputs to automatically seek the optimal resonance frequency despite inevitable resonance frequency variations during operation and between devices.

The TM and SAW boards embody these principles. Their block diagrams are shown in Fig. 6.1, and we will explain their specific implementations including design choices, parts, layout, testing, and a step-by-step guide in later sections.

6.2.2 Automatic resonance search

In addition to the circuit blocks discussed in the last section that are required for basic functionality, both systems also include blocks to perform a resonance search. The PLL frequency range is swept by the MCU with a frequency step of 1 kHz, and the output current to the SAW device is measured, digitized, and recorded at each frequency step. An initial search range is specified in the algorithm to both minimize the time required to perform the sweep and reduce the risk of a spurious resonance mode's selection. The voltage amplitude, V, at the final stage of the signal chain and in the driver amplifier, is constant by virtue of its resistor feedback architecture. Therefore, the higher the output current amplitude, I, the higher the power, P, delivered to the device since $P = VI$.

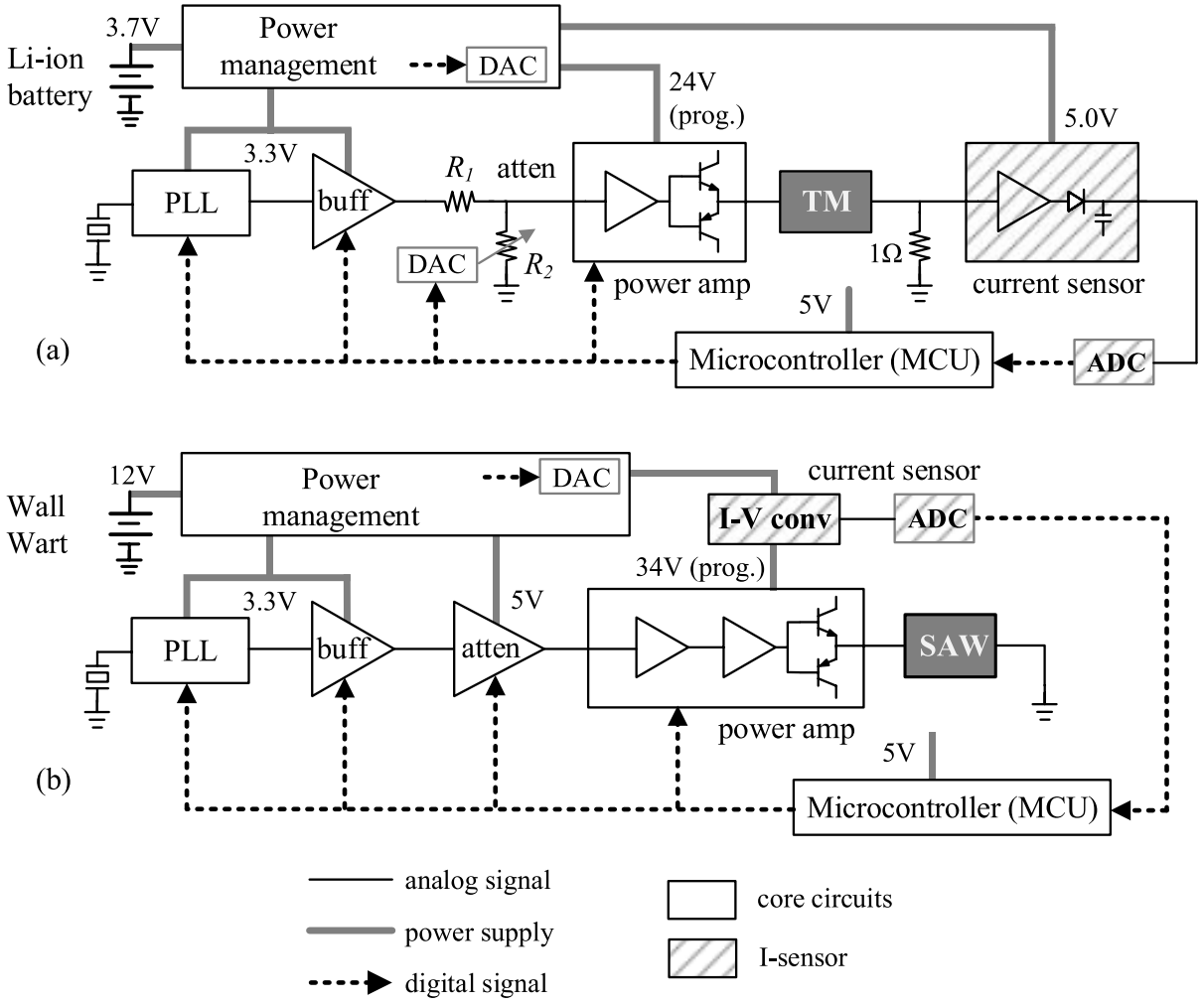

Figure 6.1: Block diagrams of the driving circuits designed for (a) the TM board designed specifically to drive a 1–25 MHz thickness mode (TM) transducer in a handheld, battery-powered nebulizer, and (b) the SAW board, designed to drive a 30-100 MHz SAW transducer, originally for enhancing the capacity of a rechargeable lithium metal battery, but useful for a broader range of acoustofluidics applications as illustrated later.

The frequency at which the measured current amplitude is maximized corresponds to the resonance frequency of the transducer. This feature effectively combats device-to-device differences and accounts for changes in circuit loading conditions, in particular the presence of liquid on the surface of the SAW or TM device. These factors often shift the resonance by

100 kHz or more, which is sufficient to significantly reduce the performance of an acoustic transducer, as most transducers have a quality factor (Q) [1] of >100, representing a very narrow bandwidth. Achieved by a straightforward electronics design and controlled by the MCU, this feature ensures all transducers are driven at their optimal frequency, despite any resonance changes. This might arise from the introduction of a new vial for drug atomization, too much fluid introduced in an experiment by accident, using the device at a different temperature, and so on.

The resonance search algorithm is verified against measurements from a vector network analyzer (VNA, E5071C Agilent Technologies, Inc., Santa Clara, CA USA) and a laser Doppler vibrometer (LDV, UHF-120SV, Polytec, Irvine, CA USA). A current spectrum resulting from a resonance search on the TM board reveals two peaks (Fig. 6.2(a)) from which the largest is chosen, thus identifying 6.62 MHz as the resonance of the transducer under test. The search is repeated with a drop of water on the transducer, which slightly shifts the resonance. Piezoelectric transducers can be modeled as a series combination of a frequency-dependent resistor, an inductor, and a capacitor. The impedance of such a circuit can be modeled as a complex function of frequency with a zero imaginary component at resonance, i.e., the inductive and capacitative components cancel out, leaving behind the real part: a pure resistance. This is equivalent to the frequency at which the S_{11} parameter, the input port voltage reflection coefficient from the VNA, intersects the real axis on a Smith chart (Fig. 6.2(b)). The closer the intercept point is to the origin, the

[1] $Q = f_c/\Delta f$, where Q is the quality factor, f_c is the resonant frequency, and Δf is the width in frequency space of the corresponding peak at half the maximum amplitude. Quality factor is also intuitively associated with the energy loss of the oscillation [46].

lower the resistance, so the highest peak in Fig. 6.2(a) should occur at the same frequency as the left-most intercept in the Smith chart (Fig. 6.2(b)). Four thickness mode (TM) transducers intended for the TM board were all tested as shown in Fig. 6.2; each pair of frequencies identified with this technique agreed to within 0.2%. Similarly, a 40 MHz SAW transducer was tested and the VNA and the on-board algorithm were found to agree within 0.2% (Fig. 6.3). In each case, an LDV scan was performed over the region of interest on the transducer, and both the TM and SAW transducers were confirmed to have the largest amplitude at the frequency indicated by the on-board algorithm and the VNA.

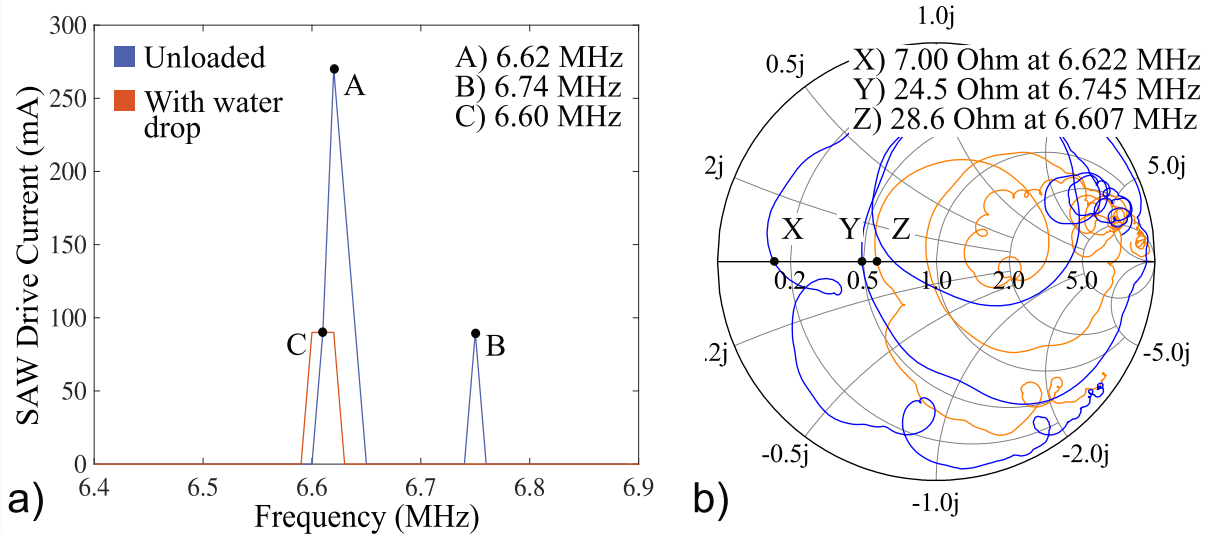

Figure 6.2: A TM transducer was run through a frequency sweep using both the TM board and a VNA. The blue plots correspond to a dry transducer and the orange plots correspond to a transducer laden with a $\sim$5 $\mu\ell$ drop of water. (a) The current across the transducer is measured over the frequency range of interest by the MCU. A simple algorithm identifies the largest peak, in this case peak A when dry and peak C with water present. (b) Measured S_{11} of the TM transducer on a VNA. This confirms that the measured current peaks correspond to resonances of the transducer, both with and without liquid present. The messy appearance of the Smith chart is expected for a TM transducer with finite lateral dimensions, since spurious Lamb wave modes exist at similar frequencies. Despite this, the algorithm is still able to identify the desired TM mode for the drive circuit.

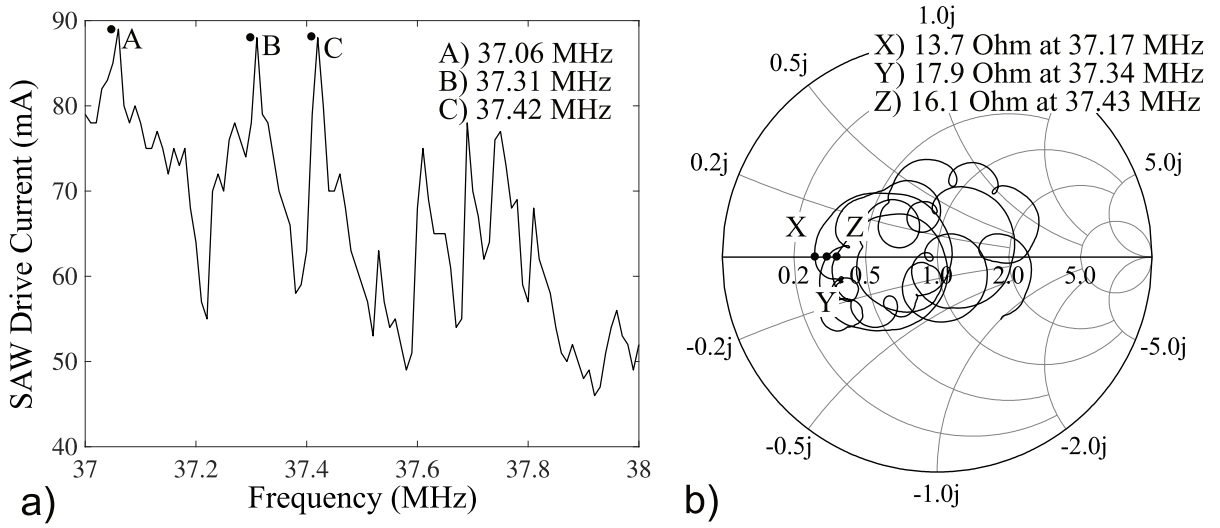

Figure 6.3: A SAW IDT was run through a frequency sweep using both the SAW board and a VNA. (a) The current across the transducer is measured over the frequency range of interest by the MCU. The algorithm simply identifies the largest peak, in this case peak A. (b) Measured S_{11} of the SAW transducer on a VNA. This confirms that the measured current peaks correspond to resonances of the IDT. It is expected that multiple adjacent resonances—*side bands*—exist in an IDT that lacks specific design features, such as apodization, to prevent them.

6.2.3 Implementation in two examples

Here we elaborate on the circuit design and fabrication principles described in the main article for both the SAW board and the TM board. The thickness-mode (TM) board drives a 6–7 MHz thickness mode transducer to achieve a handheld nebulizer. SAW is impractical at less than 40 MHz because the penetration depth of the SAW is 4–5 wavelengths, exceeding the 500 μm thickness of the widely available piezoelectric lithium niobate wafers used for this purpose. The transducer is driven by 0.5 to 2 W of power. The SAW board has a similar design, but is tailored to drive a 40–120 MHz SAW device used to enhance the capacity of a rechargeable lithium metal battery. The SAW transducer typically demands 0.1 to 1 W of power in this application. The SAW devices demand as

much as 5 W for atomization, the reason for the selection of other vibration modes that are more efficient in that application. However, the designs described in this Electronic Supplementary Information may be readily modified to produce driver circuits appropriate for these greater power requirements.

We will describe our choice of integrated circuits (ICs) for these applications. Since the TM board will be operated by a small 3.7 V battery, the power consumption of the electronics should be minimized. On the other hand, the SAW board operates at much higher frequencies, thus demanding higher-speed electronics. Fortunately, the board is powered by wall-wart supply, so the overall power consumption is of secondary concern. Note that the resulting boards, while fairly optimized, are not unique. Many IC options exist to accomplish the same function, each offering some trade-off in cost, size, performances, ease of assembly and usage. Engineers often start the design process by exploring and comparing ICs from the vast, searchable catalogues on electronic component distributors' web pages.

The SAW driver signal chain begins with the stimulus source. The complementary metal–oxide–semiconductor (CMOS) Si5351 (from Silicon Laboratories) clock generator (PLL) chip was employed to synthesize a tone with programmable frequency between 2.5 kHz to 300 MHz. It is followed by the CDCLVC1104 clock buffer (Texas Instruments, Dallas, TX USA). At 3.3 V input, it can operate up to 250 MHz. It is used to drive the attenuator that follows, preserve the low-skew clock, and accomplish duty-cycle control for pulse-width modulation. To shorten the development time, identical PLL and buffer circuits are used for both boards. Potential savings in cost and power did not warrant a

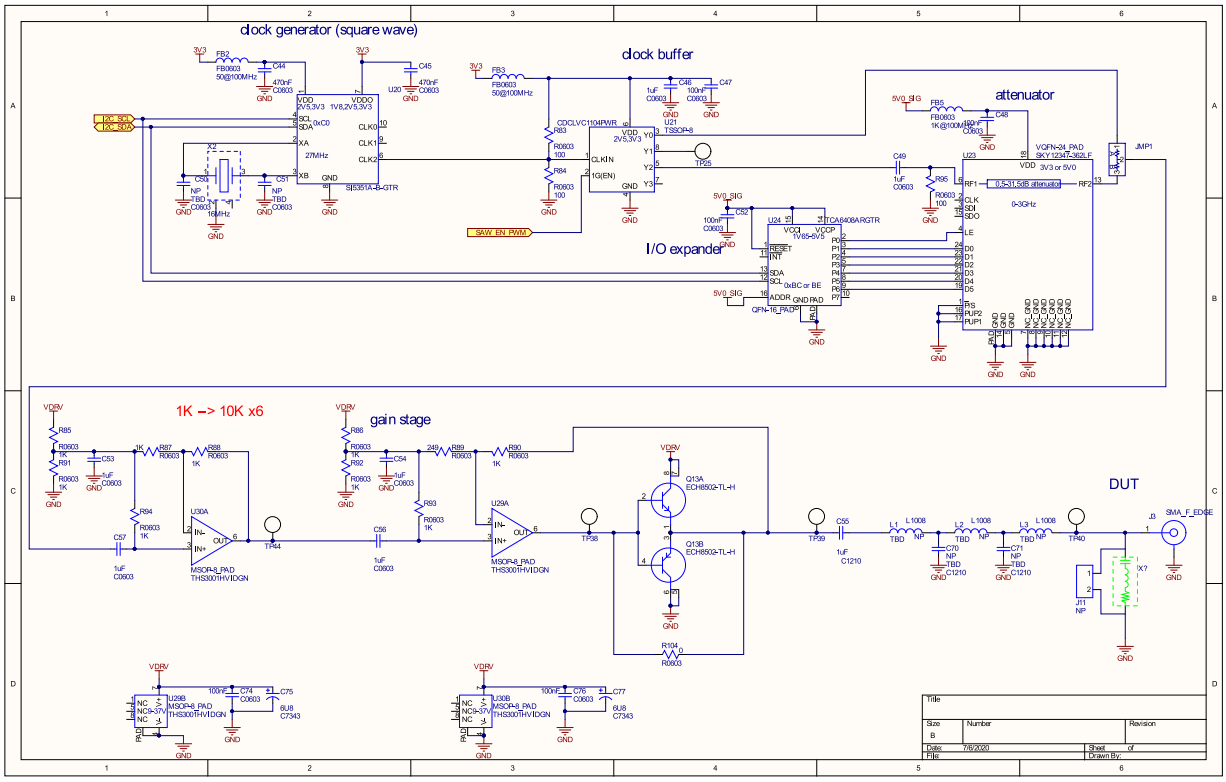

Figure 6.4: Each circuit component is symbolically represented in this schematic organized for conceptual clarity.

customized design effort in this case.

Gain control is achieved by a programmable attenuator. The TM board features a "resistor divider" with a variable resistor (R2) achieved by an N-type metal-oxide-semiconductor (NMOS) transistor. Its resistance is digitally adjusted by the gate voltage fed by a voltage DAC (digital-to-analog converter) MCP4726 (from Microchip Technology). While this very simple implementation works well at low frequencies, the parasitic capacitance of the NMOS transistor will form a RC (R for resistance, C for capacitance) low-pass filter (LPF), distorting waveforms at higher frequencies. Therefore, the SAW board employs an active attenuator IC SKY12346 (from Skyworks Solutions). Designed

for broadband cellular (up to 3 GHz) operation, the attenuator has no LPF or distortion issues, but at the expense of added direct current (DC) power consumption.

To boost the signal to drive the thickness mode device, the power amplifier section of the TM board employs one stage of a voltage feedback amplifier LM7171 (Texas Instruments). At 6.5 mA bias current, it features a unity-gain bandwidth of 200 MHz, sufficient to handle multiple harmonics of the clock to preserve the sharp, square waveform. On the other hand, the SAW board employs the amplifier THS3001 (also from TI), whose bandwidth reaches 420 MHz at slightly higher (10 mA) bias current. Moreover, gain is distributed into two stages. As the gain of each amplifier is lowered (halved), its stability at high frequencies, formally measured by the "phase margin", also improves. As the last stage of the signal chain, the power amplifier shall deliver high current to the SAW. To achieve that goal, a standard bipolar junction transistor (BJT) push-pull output driver is employed. Configured as emitter followers, a complementary PNP and NPN BJT pair (ECH8502, from ON semiconductor) can efficiently and rapidly pump and sink currents into and from the load.

The micro-controller (MCU) function is provided by the Arduino nano clone ATmega328P (from Microchip Technology) and the accompanying software. It is pre-loaded with programs to calculate, based on user inputs and component parameters, the control signals for all ICs on the PCB. The input-output (I/O) expander chip TCA6408A (from Texas Instruments) provides eight bits of general-purpose parallel input/output expansion for the two-line bidirectional "I2C" bus protocol, simplifying all IC control and user interfaces.

For the power management unit (PMU), there are literally thousands of boost converter ICs (voltage step-up) and low-dropout (LDO) regulator ICs (voltage step-down) for designers to choose from, targeting different input/output voltage ranges and current ratings. The design process is fairly straightforward. For example, the main input of the TM board comes from a 3.7 V battery, and 3 V, 5 V and 24 V are desired. This is accomplished as follows: (1) a boost converter XCL101C (from Torex Semiconductor) steps up 3.7 V to generate 5 V; (2) an LDO regulator TLV733P (from Texas Instruments) steps down from 5 V to generate 3 V; and (3) a boost converter MP3213 (from Monolithic Power Systems) steps up from 3.7 V to 24 V. On the other hand, the main input of the SAW board comes from a 12 V wall wart supply, and 3.3 V, 5 V and 34 V are required. This is achieved by: (1) two LDO regulators MIC5225 (from Micrel Technology) stepping down 12 V to both 3.3 V and 5 V, and (2) a boost converter LT3489 (from Linear Technology) stepping up from 12 V to 34 V.

The current sensing function in the TM board is achieved by a 1Ω series resistor, directly performing current-to-voltage (I-to-V) conversion on the output sinusoidal current driving the SAW device. The corresponding voltage signal is subsequently amplified and rectified (LT1810, by Linear Technology); a diode (BA891, by NXP) provides peak detection from this signal. The resulting peak DC voltage is digitized by an ADC (analog-to-digital converter) embedded in the MCU. The MCU automatically sweeps the PLL (stimulus) frequencies over a pre-defined range and records all corresponding ADC values. Resonance is given by the frequency at which the peak ADC value occurs. The current sensing function in the SAW board is indirectly performed. High-frequency current signals

vary too quickly for direct rectification and peak detection without disrupting the normal operation of the power amplifier. Instead, a current amplifier chip (LTC6101, by Analog Devices) is employed at the power supply of the driver amplifier.

6.2.4 Layout and testing

Having chosen the ICs and defined the circuit architecture, the design may be laid out on a custom-made printed circuit board (PCB). There are many commercially available computer-aided drafting (CAD) tools to aid with the PCB development process. Here, Altium Designer was employed. The design process begins by capturing all circuit components schematically (Fig. 6.4). Symbols representing ICs are connected to all required circuit components. The functions and performances of certain critical parts (e.g. the driver amplifiers) can be verified using circuit simulation software such as LTspice®. All components are laid out according to design rules and manufacturing requirements while maintaining interconnectivity.

The above procedure entails a fair amount of design time, cost, and efforts. In order to make the engineering tasks more manageable, especially when new chips or circuit functions were introduced, we adapt the following step-by-step approach. To start, we employ "evaluation boards" offered by chip vendors (e.g., Si535x–B20QFN–EVB for the phase-locked loop (PLL) from Silicon Labs) to test out the circuit functions rapidly. The drawback is the higher cost, and the clumsy interface and size. Next, we integrate all chips onto a relatively large, two-layer PCB. Routings are done in a straight-forward manner, with all components mounted on only one side of the board, ICs with bigger packages

are chosen for easier soldering and probing, and multiple test points and signal breaking points (with a 0ω resistor) are generously incorporated. To avoid signal noise, wide traces and large copper planes for ground and power are used. After this easy to build PCB has been debugged and the functionality verified, the layout is optimized to achieve the desired form factor. Board size is reduced by using double-sided, multi-layer PCBs with dedicated ground and power planes. Testing features, with a few crucial exceptions, are removed. More densely packed components require more carefully planned routings to avoid long traces and signal cross-talk.

6.3 Application to handheld acoustofluidics devices

For microcircuit-driven acoustofluidic devices to be viable, they must perform similarly to benchtop devices designed and demonstrated in laboratories. We compare our handheld nebulizer—utilizing the TM board (Fig. 6.5(a)—with acoustofluidic atomization literature and with a benchtop driver setup with an identical transducer. The TM board has a custom program pre-loaded to facilitate use without further connection to a computer or other device. Such a pre-programmed board design is especially convenient in a prototype closer to use as a consumer product.

Similarly, we present three implementations of the SAW board and compare these results with benchtop-driven devices from the published literature and a benchtop signal generator and amplifier combination driving these same three devices in our own laboratory. The frequency, power, and duty cycle delivered by the SAW board can be selected by

defining these parameters in a custom (MATLAB, Mathwords, Natick, MA USA) script uploaded from a connected PC to the board's MCU. An externally connected PC is required to change these settings with the SAW board, and the PC is convenient for real-time download of the operating state of the SAW board, making it possible to adjust the board's operation and detect the effects from the computer. This is much more difficult to accomplish with the pre-programmed TM board.

For consistency, during comparisons with benchtop setups, the same equipment is used in all four applications. Acoustic vibrations are produced by applying a sinusoidal voltage signal to the transducers using a signal generator (WF1967 multifunction generator, NF Corporation, Yokohama, Japan) and an amplifier (ZHL–1–2W–S+, Mini-Circuits, Brooklyn, NY USA). The instantaneous voltage and current are measured and used to compute the net power input via an oscilloscope (InfiniVision 2000 X-Series, Keysight Technologies, Santa Rosa, CA USA) as shown in Fig. 6.5(b).

6.3.1 Nebulization

Megahertz frequency acoustofluidic nebulization offers several advantages over current technology for delivering therapeutic proteins, cells, functionalized nanoparticles, and monoclonal antibodies to the lungs[161, 169, 170]. It is cheaper and less prone to clogging than the current state-of-the-art, ultrasonic mesh nebulizers. These operate at much lower frequencies and in order to generate droplets small enough for optimal lung delivery, and they must rely on 5 μm laser-cut holes in a metal plate through which a drug solution is forced[171, 172]. Mesh nebulizers tend to be tailored to work with a particular

solution and have a limited range of fluids that they will nebulize. Mesh nebulizers in general may cause damage to biomolecules due to high shear forces and kHz-order frequency operation[173, 174]. By contrast, acoustofluidic nebulization has been demonstrated for delivery of antibodies[162, 163] and DNA[161]. There is also some evidence—in unpublished work—that the droplet size can be adjustable during device operation. This could be necessary either between patients, for example adults and children, or in compensation for the changing airflow during inhalation and exhalation. These aspects are important in seeking appropriate dose control in pulmonary delivery[161].

However, MHz-frequency nebulization is only competitive with mesh nebulizers if it can be decoupled from benchtop equipment, enabled for the first time with the TM board (Fig. 6.5). A previous attempt at such a circuit[64] did not provide sufficient power for consistent atomization, even with signal modulation intended to reduce the average power consumption[148]. Furthermore, this circuit could drive transducers at only a single, predetermined frequency, and had a short lifetime of a few hours.

We present a handheld nebulizer based on a lithium niobate TM transducer, which has been shown to produce higher efficiency atomization (flow rate per unit power input) than either SAW or other wave types in lithium niobate or TM in lead zirconate titanate (PZT)[175]. We drive the 3x10 mm TM lithium niobate transducers at their primary resonance frequency as indicated in Fig. 6.2, usually 6.6 MHz. The device consists of a transducer holder, a fluid supply system, and the TM board powered by a rechargeable lithium-ion battery (Fig. 6.5). The user interface consists of a power switch and five buttons: resonance frequency algorithm run, switch on or off, amplitude increase, amplitude

decrease, and reset. The transducer holder provides electrical contact while minimizing mechanical damping of the acoustic waves. A video provided in the ESI † demonstrates operation of the nebulizer.

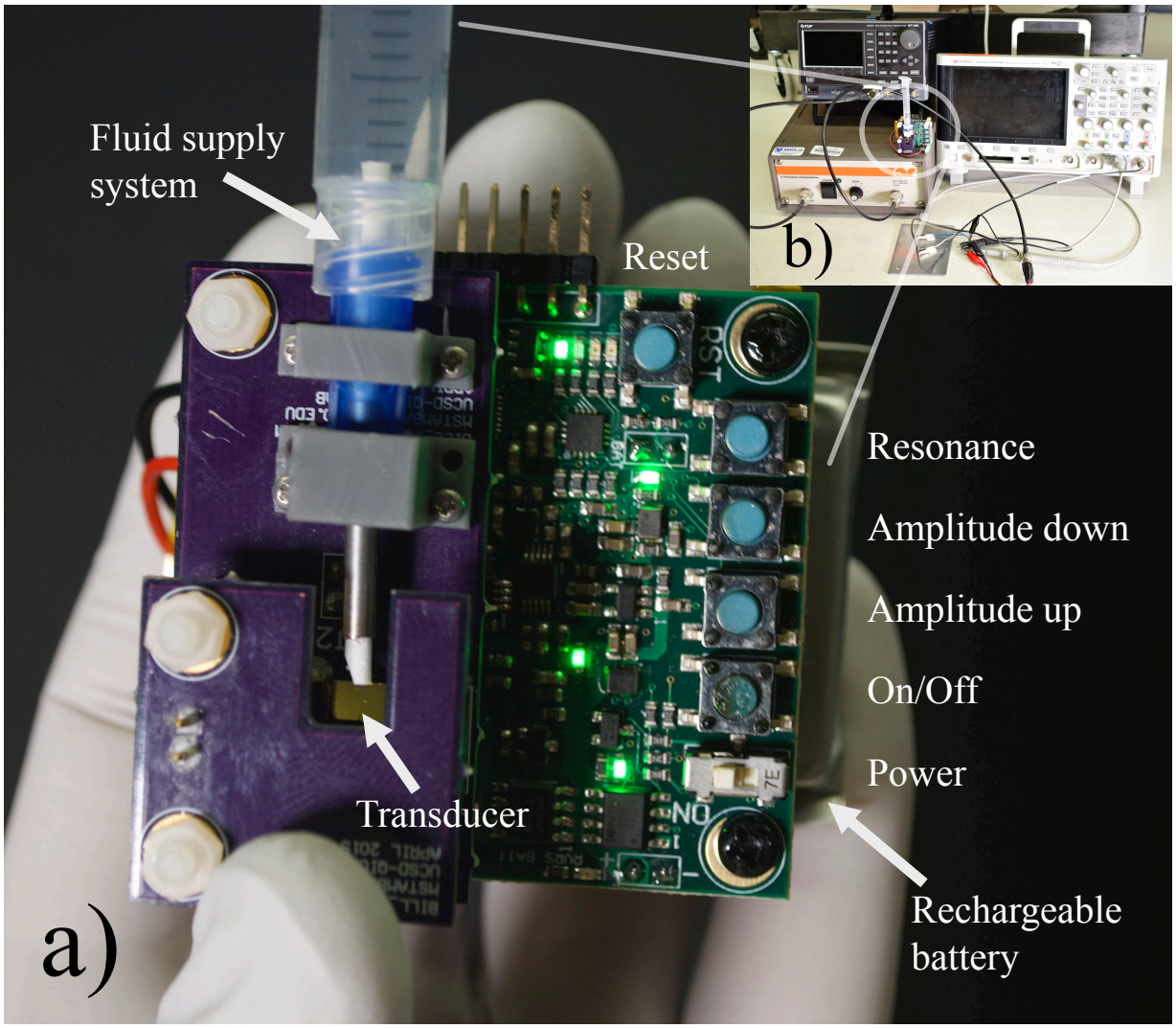

Figure 6.5: (a) Major components of the handheld nebulizer are labeled along with the user interface. (b) Benchtop equipment—including signal generator, amplifier, oscilloscope, cables, and connections—typical of the acoustofluidic device experience—is entirely replaced by our small, inexpensive, and portable circuit.

Liquid is wicked from a reservoir through a fibrous nib onto the transducer surface. A physically hydrophilic region is ablated onto the surface of the transducer using an excimer

laser (LaserShot, Optec, Belgium). This hydrophilic region and the capillary action of the nib help draw liquid out in a thin layer over the transducer. While the transducer is vibrating, acoustowetting provides additional flow forcing[176], leading to a semi-passive liquid supply system that ensures liquid is only drawn out during nebulization, which prevents flooding and drying out of the transducer surface. No active pumping mechanism is required.

We compare the performance of our 6.6 MHz handheld nebulizer to an equivalent atomization set-up with a benchtop signal generator and amplifier. The benchtop set-up can deliver greater power inputs and produces a pure sine wave voltage signal, which often produces a cleaner acoustic wave. The handheld device uses a square wave, which significantly reduces the complexity of the circuit, thus allowing it to fit in a smaller footprint and reducing development time and cost. More frequency modes are generally excited by a square wave, but we show that TM nebulization performance is unaffected. Figure 6.6(a) demonstrates that the droplet size distribution for water is not significantly affected by the voltage signal waveform. The maximum flow rate for a given power input, again, using water, is similar between the handheld and benchtop devices (Fig 6.6(b). These results are the same order of magnitude for maximum flow rate compared with the literature—Winkler *et al.* report 0.2 mℓ/min at 3.5 W for SAW[177] and Collignon *et al.* report 0.3 mℓ/min at 1.4 W for TM[175], all with water (though the latter does report a broader range of fluids). The majority of the atomized water volume occurs in droplets less than 10 μm, ideal for pulmonary drug delivery. The power output of the handheld device is currently limited by a maximum voltage of 22 V (equivalent to $\sim$2 W in this

case), which is sufficient for all but the most demanding acoustofluidics applications. It may be increased, but such an increase must be balanced against the cost and time of further development and any size or battery constraints.

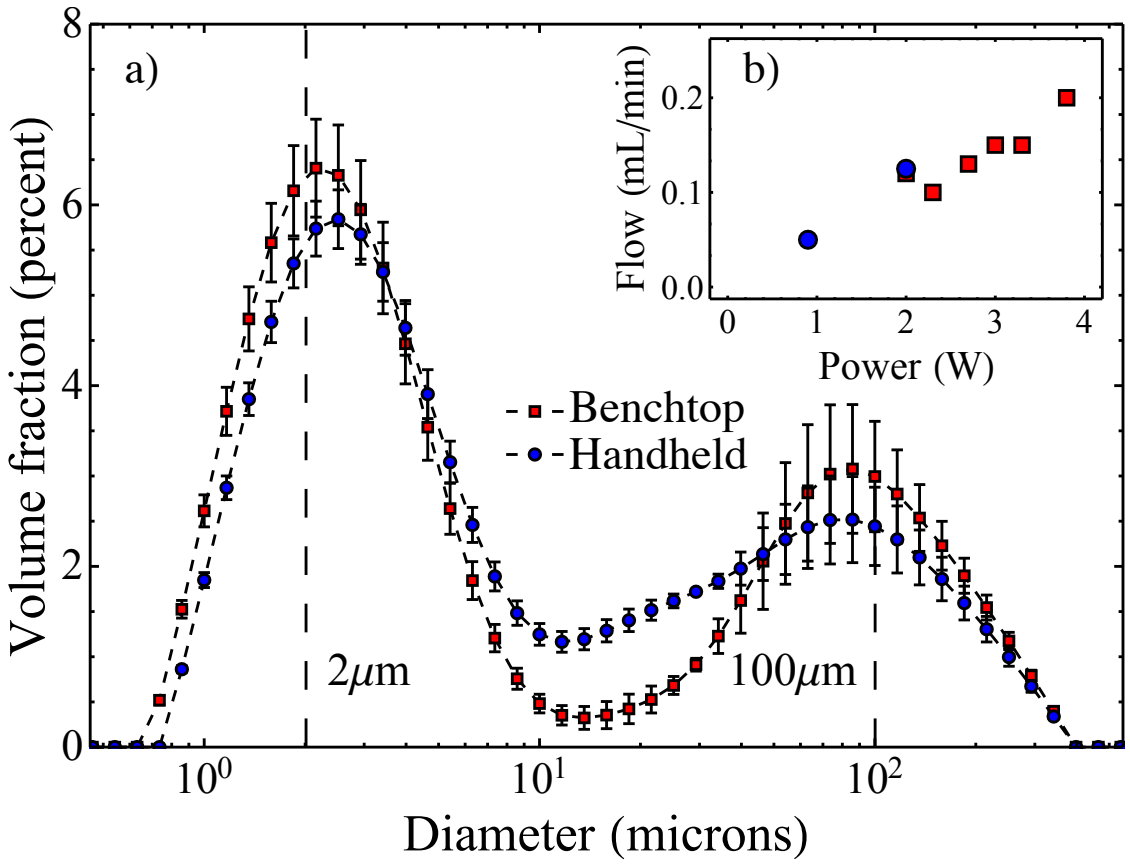

Figure 6.6: (a) Droplet size distributions were obtained using a laser diffraction particle sizer (Spraytec, Malvern). Three measurements were taken for both the benchtop set-up and the handheld device and the mean values and standard errors are reported. Identical electrical/mechanical contact and fluid supply was used in each case and in each case the transducer was driven at 6.6 MHz and 2 W. Notice that the distribution is in terms of volume fraction so that a small number of large droplets produces a relatively large peak—the vast majority of droplets are close to 2 μm. (b) For experiments in this plot alone, for the purpose of accuracy, flow rates were imposed using a syringe pump. The power was adjusted until atomization was sustainable—no sputtering and no flooding. Again the transducer contact and fluid supply were identical in both the benchtop set-up and the handheld device.

SAW board set up

Here we provide a sample image of the SAW board during its use to perform a typical acoustofluidics-based chip operation. Please also consult the video provided in the ESI † that demonstrates operation of the SAW board during fluid mixing.

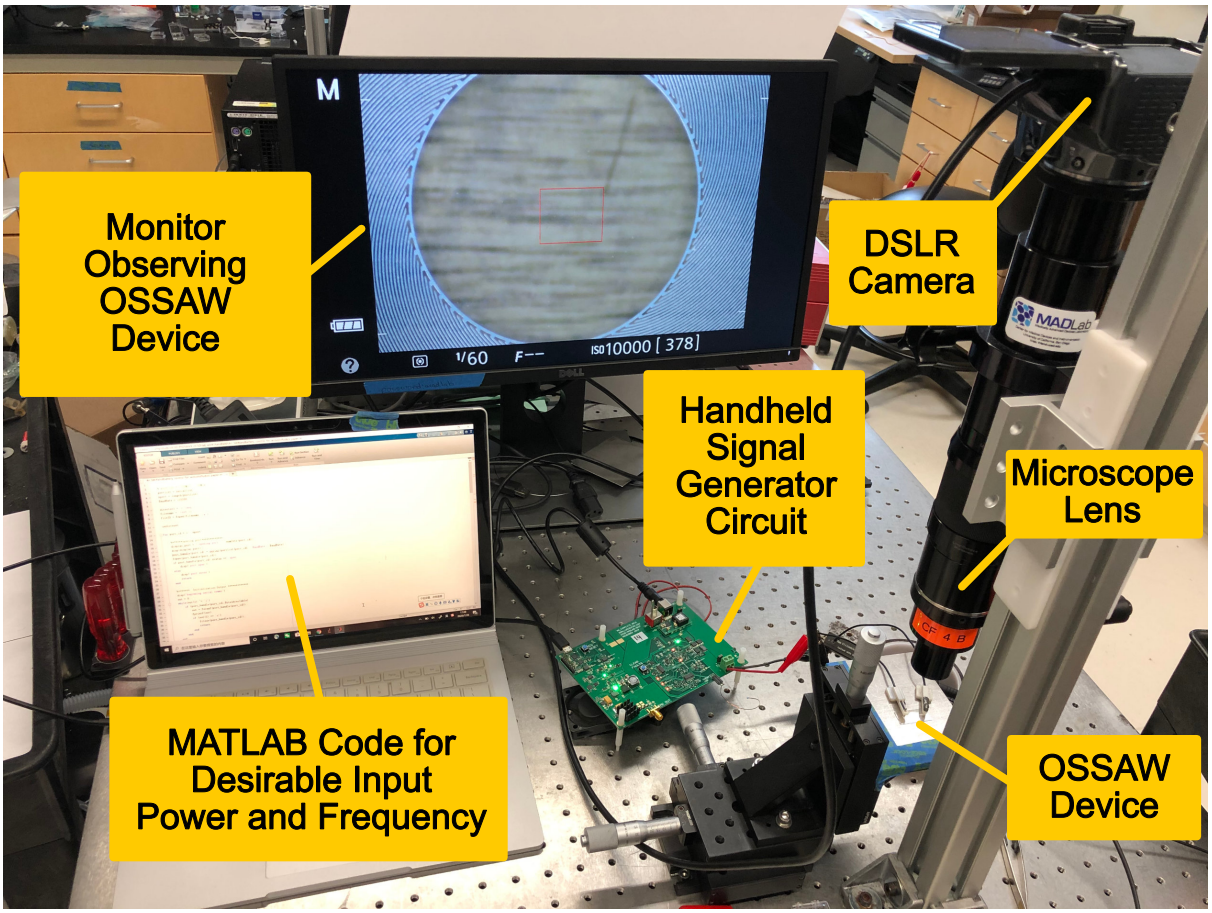

Figure 6.7: An example of the SAW board in use for SAW-induced particle separation.

6.3.2 Mixing in liquid droplets

Rapid and complete mixing in microfludics and nanofludics is needed in time-sensitive chemical reactions and bio-chemical processes [151, 178]. However, diffusion dominates

micro scale mixing because the flow is usually laminar. Such diffusion-based mixing is too slow for most lab-on-a-chip applications especially for biological samples. Adopting surface acoustic wave (SAW) induced acoustic streaming to generate chaotic advection is a solution to increase the diffusion rate and decrease the mixing time significantly, as shown by Shilton et al.[179].

We illustrate rapid mixing in a simple experimental setup. A single droplet contains two initially separate liquids—a 1 $\mu\ell$ transparent glycerol drop is first placed on the surface and then a 0.25 $\mu\ell$ blue-color dyed water drop is placed into the glycerol droplet (*see* Fig. 6.8(a)). A 40 MHz SAW device is chosen to produce efficient mixing between the two droplets. Fig. 6.8(b) shows a drop that has been mixed using benchtop equipment for 7 s at 280 mW. Fig. 6.8(c) shows a drop that has been mixed for 6 s at 300 mW using a handheld circuit as illustrate in Fig. 6.7. These results are essentially equivalent and are on par with literature values, for example, Shilton *et al.* report complete mixing of colored dye into a glycerol solution in 8 s at $\sim$1 W (the excess power is because there was a microfluidic well instead of a sessile drop in that case, which increases attenuation).

6.3.3 Microparticle separation within a microliter sessile droplet

Particle and cell separation induced by SAW in sessile drops has become a popular platform due to its convenience, rapid response, and biocompatibility. Straight and standard interdigital transducers (IDTs) with a sessile drop located at an offset position from the center of the SAW propagation direction have been used to spin fluid droplets, producing particle concentration and separation due to asymmetric SAW actuation [1, 3, 180].

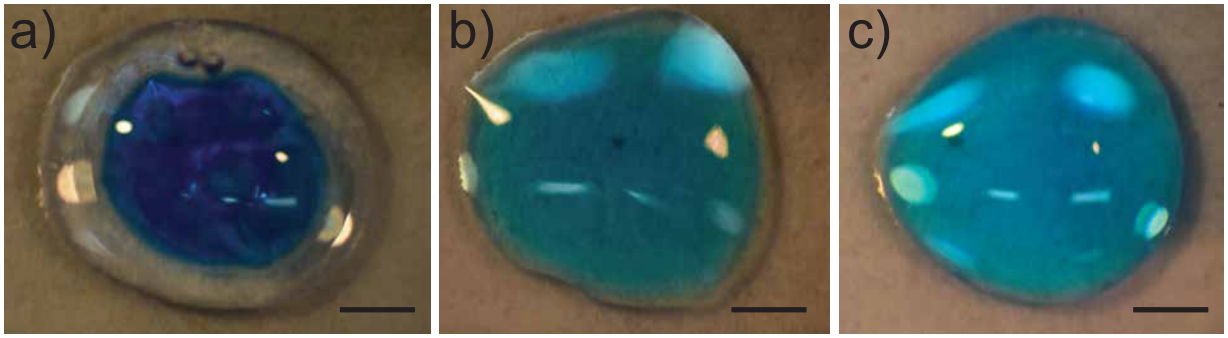

Figure 6.8: Effective droplet mixing via travelling surface acoustic wave. The water droplet is dyed with blue color (the middle ring), while the glycerol droplet remains transparent. (a) is the pre-mixing stage, (b) and (c) are the post-mixing stage via external driven power caused chaotic mixing with benchtop signal generator with power amplifier and handheld circuit boards, respectively. The scale bar represents 250 μm.

We have recently produced a novel omnidirectional spiral surface acoustic wave (OSSAW) interdigital transducer design. This spiral design was developed such that the wave propagation direction is always rotationally symmetric and tangent to a circle inside the IDT structure (*see* Fig. 6.9). This allows the production of inward-bound acoustic waves ideal to spin a droplet, but only because we have placed the IDT on a selected cut of lithium niobate that allows the production of SAW in any direction [181]. We further demonstrated accurate particle manipulation and multi-size separation in a microliter ($\mu\ell$) drop with this effort.

Here, we perform microparticle separation with the same OSSAW transducer, but now employ the SAW board instead of a standard benchtop setup. An operating frequency of 40 MHz was chosen to produce a $\sim$8 μm particle/cell separation threshold, taking into account particle compressibility [66, 182, 183]. Polystyrene (PS) particles (Polysciences, Inc., Warrington, PA, USA) with diameters of 4 and 38 μm were selected to show size-selective separation at the microscale. A 1 $\mu\ell$ droplet containing these particles in concentrations of

4×10^9 and 1×10^5 particles/mℓ, respectively, was placed at the center of the transducer. After ~5 s at ~1 W, the smaller particles collected at the periphery and the larger particles concentrated at the center (*see* Fig. 6.10b-d and a video in the ESI †). The same result was obtained with either the SAW board or the benchtop equipment described above and it is reasonably comparable to past work[3] using lab equipment, where 6 μm and 31 μm particles were separated using 20 MHz SAW at 250 mW in ~4 s. Our implementation requires more power for a similarly sized sessile drop because the frequency is much higher, which causes greater attenuation but produces superior separation selectivity based on particle size.

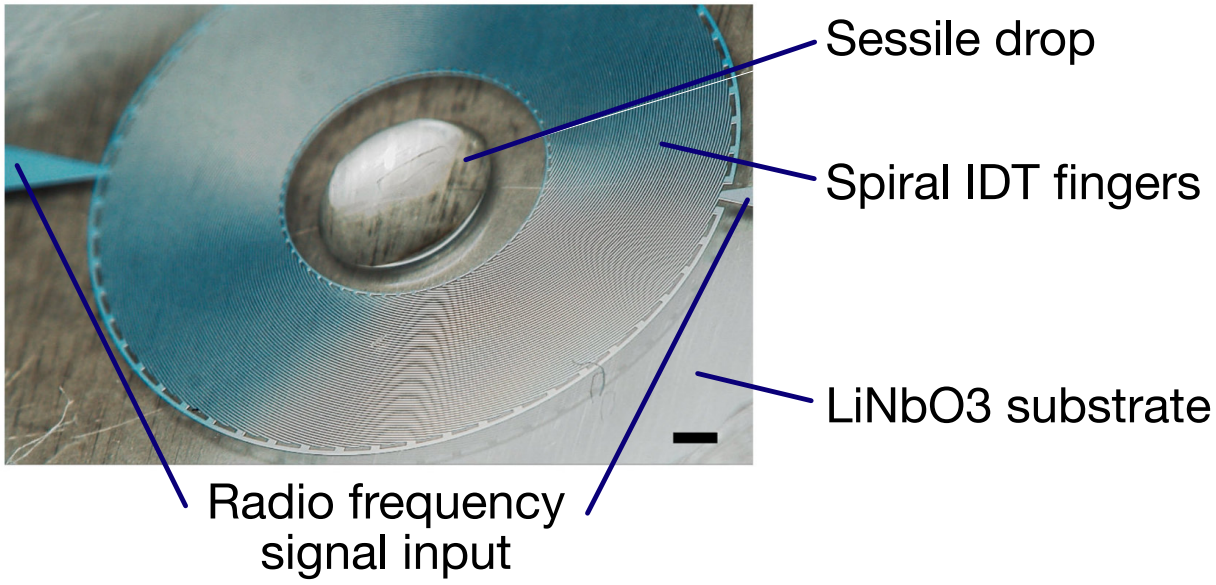

Figure 6.9: A 60-MHz OSSAW device with a microliter sessile drop in the inner circular region, showing the fingers and electrode connection to produce a suitable spiral SAW. Scale bar: 0.5 mm.

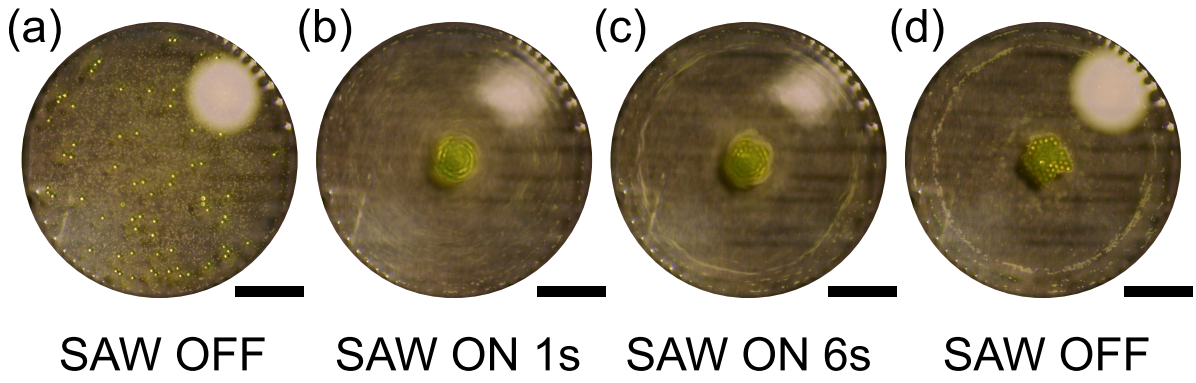

Figure 6.10: Effective particle separation via omnidirectional spiral surface acoustic waves (OSSAW) with size of 38 μm and 4 μm operated at a resonance frequency of 40 MHz. (a) Before SAW actuation, (b) 1 s after SAW is on, (c) 6 s after SAW is on, and (d) after SAW actuation. Scale bar: 0.5 mm. The bright dot at the top right of the droplet is the light reflection from the droplet boundary.

6.3.4 Particle alignment

Particle alignment via collection at nodes of acoustic standing waves has been demonstrated for applications such as tissue engineering[184] and cell characterization[153] and serves as a fundamental tool wherever small particles need to be patterned. Utilizing acoustic forces rather than laser actuation as in optical tweezers prevents damage to cells and does not rely on the magnetic or electric properties of the particles. Standing waves generated by counter propagating SAWs with the same frequency create stationary pressure nodes, where suspended particles can be trapped by acoustic radiation force. The spacing between adjacent nodes is determined by the wavelength ($\lambda/2$). Chirped IDTs allow for a range of frequencies to be used in the same transducer so that the nodal and anti-nodal positions can be changed at will[159, 185].

We present particle alignment and patterning with adjustable spacing driven by the SAW board. Two pairs of chirped IDTs with resonance frequencies in the range 40–

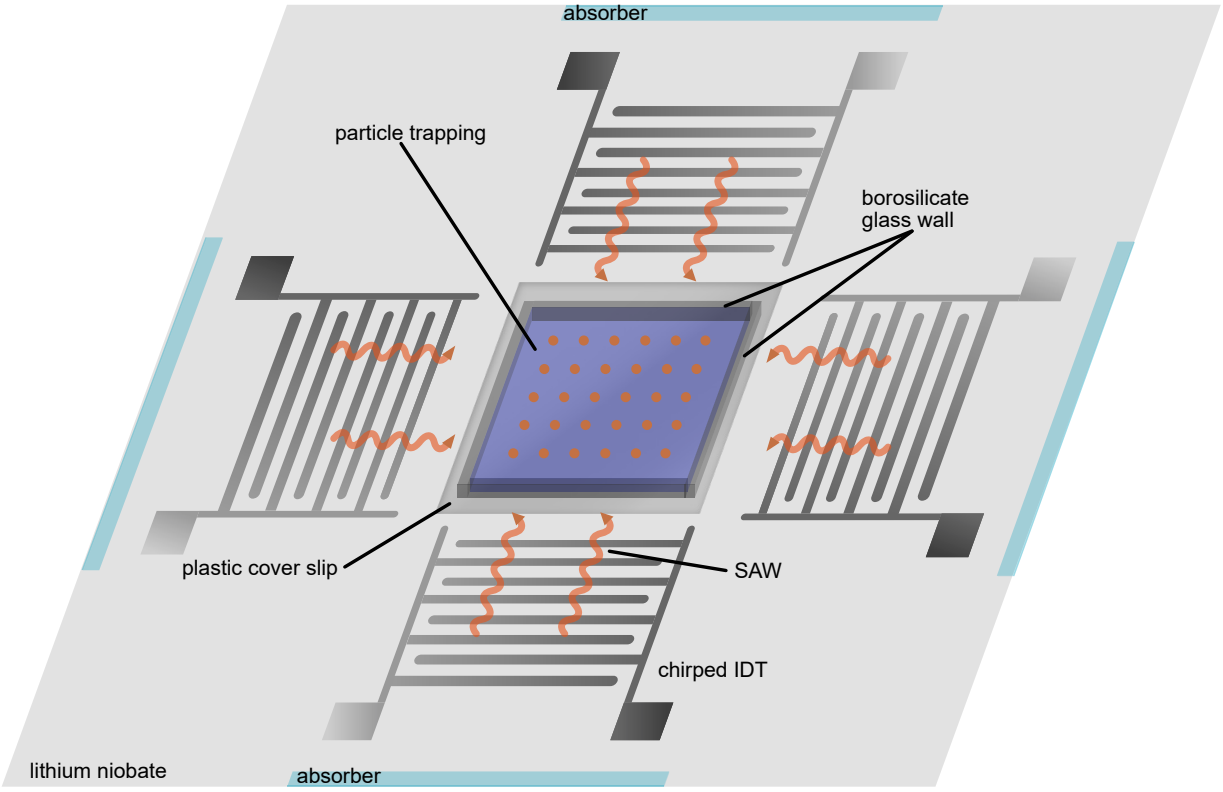

Figure 6.11: A schematic graph of the 2D alignment device. 4-way chirped IDTs create pressure node so that particles will be trapped.

80 MHz were fabricated around a 6 mm by 6 mm closed glass chamber 100 μm in height (*see* Fig. 6.11). Fluorescent polymer particles 2.1 μm in diameter were aligned in various patterns based on the signals generated with the SAW board. When only one pair of IDTs, as shown in Fig. 6.12(a) and (b), are powered at 40.2 MHz, the particles are aligned in lines with 48.5 μm separation, close to one half the SAW wavelength (49.9 μm); this wavelength is the relevant one as the particles are near the substrate [186]. When all four IDTs are actuated, particles assemble around nodal points to form an equally spaced array. With the chirped IDT, the spacing may be adjusted by changing the frequency. Fig. 6.12(c), (d) and (e) display the arrays at 40.2 MHz, 59.8 MHz and 79.4 MHz, respectively, resulting

in 48.3 μm, 34.1 μm and 25.3 μm spacing. A comparison of results obtained with the SAW board and with the benchtop equipment are given in Table 6.1, which shows nearly identical results. This capability closely mimics that demonstrated by Shi *et al.* where 2 μm particles were aligned to a grid with ~50 μm spacing in a matter of seconds[187].

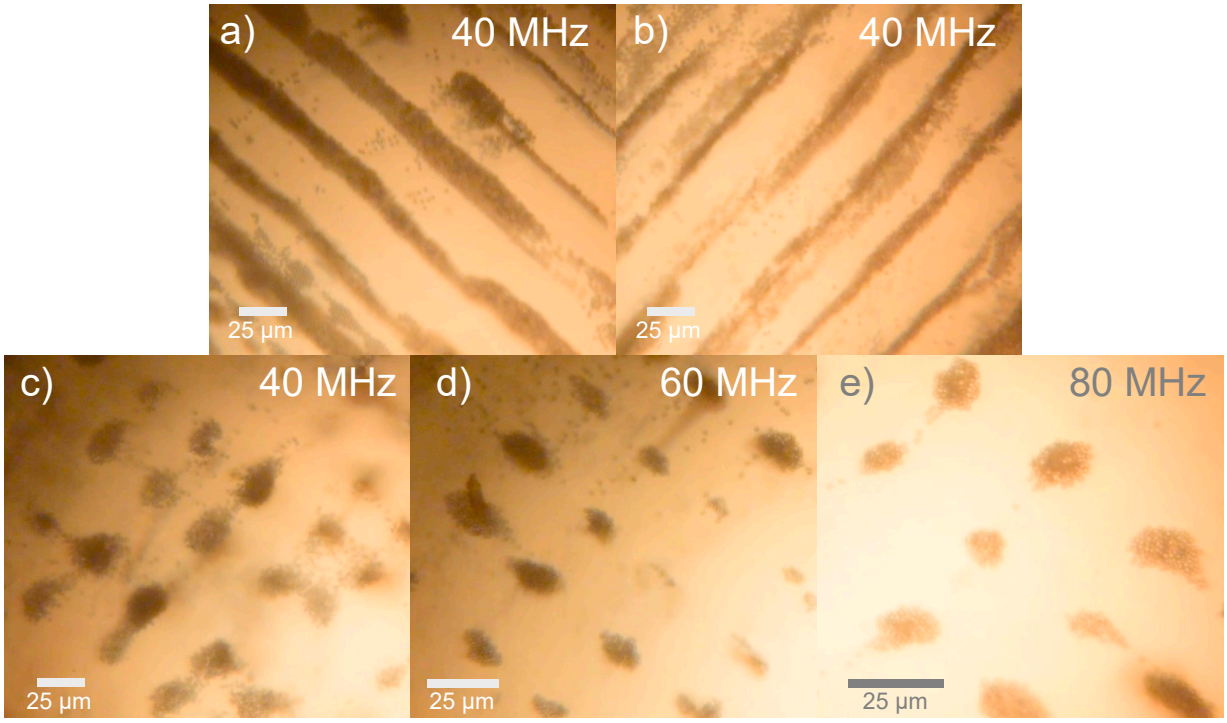

Figure 6.12: When only two IDTs are actuated, particles are aligned in lines along (a) the x direction or (b) the y direction depending on which pair of IDTs are actuated (in this case at 40.2 MHz). When 4 IDTs are actuated at the same time, particles are aligned in an array with different separations at corresponding frequencies: (c) 40 MHz, (d) 60 MHz and (e) 80 MHz. Scale bar: 25 μm.

Table 6.1: Comparison of handheld device and regular signal generator.

	Handheld device	Signal generator
Frequency (MHz)	40.2	40.2
Voltage output	70%	1.69 V
Oscilloscope read	2.1 V	2.1 V
Response time	7.0 s	6.8 s
Spacing (μm)	48.3	49.1

6.4 Conclusions

Acoustofluidics devices have—for far too long—betrayed the ideal of "lab-on-a-chip", bringing instead to mind the tired old joke "chip-in-a-lab" from all the signal generation and monitoring equipment tethering the devices to a lab bench just to get them to function. No longer. Acoustofluidics may now be used in practical lab-on-a-chip and point-of-care devices with the circuit design information and simple examples provided in this paper. Our aim in this contribution is to enable those trained merely in the basics of electrical circuits to be able to devise and fabricate a design for their needs. Our approach is suitable for providing controlled signals to drive 1–300 MHz acoustic devices from 50 mW to 2 W of power and, with some work by the reader, these ranges may be greatly expanded while maintaining either the mains or battery-powered, handheld format needed in many applications. Using the design principles espoused in Section 6.2, we have demonstrated a completely handheld, battery-powered acoustic device driver (the TM board) for a high-power application: atomization. We have also demonstrated a mains-powered design (the SAW board) with a computer interface useful for monitoring and controlling the operation of the driver circuit, including the power and frequency of the signal supplied to the acoustic device. This design was used for acoustic devices to produce liquid mixing, particle separation, and particle alignment exemplifying many of the operations needed in micro to nano-scale fluidics devices.

During these tests, these driver boards delivered signals equivalent to the much larger benchtop or rack-mount laboratory signal generation, amplification, and monitoring equip-

ment in use in many researchers' laboratories. Crucially, these driver boards *also* offer resonance tracking, power management, and signal monitoring features absent in laboratory equipment and necessary in the unpredictable clinical and industrial environments where these devices will be used. Together, these implementations show how almost any embodiment of acoustofluidic research could be miniaturized and rendered conveniently portable.

Chapter 6, in part, is a reprint of material that is in preparation for submission 2020. Huang, An; Connacher, William; Stamburg, Mark; Zhang, Shuai; Zhang, Naiqing; Mei, Jiyang; Jian, Aditi; Alluri, Sravya; Leung, Vincent; Rajapaksa, Anushi; Friend, James. The dissertation author was the co-primary investigator and author of this paper.

Chapter 7

Driving morphological changes in magnetic nanoparticle structures through the application of acoustic waves and magnetic fields

7.1 Introduction

Self-assembly is touted as a useful bottom-up alternative to traditional top-down fabrication techniques, improving material performance and utility of nanomaterials via superior collective physical and chemical properties in transitioning from zero to one (1D) or two dimensionally (2D) ordered patterns [188]. Such patterns, self-assembled on a liquid interface, may prove useful in emerging applications [189]. For example, 1D chains facili-

tate single electron transport [190], waveguiding [191], and energy transfer [192] along the chain axis. Likewise, 2D nanoparticle (NP) films have been considered for biosensors [193], targeted drug delivery [194], photonic crystals [195], and high-density data storage [196].

Here we used magnetite (Fe_3O_4) as our precursor NP due to its promising intrinsic properties, natural abundance, non-toxicity, chemical stability, biocompatibility, and ferrimagnetism. It is a ferrite with cubic structure (Fd3m), exhibiting unique electric and magnetic properties due to electron transfer between Fe^{2+} and Fe^{3+} at the octahedral sites, and has long been considered a useful NP [197, 198, 199].

7.2 Experiment methods

7.2.1 Experiment setup

The experimental setup is depicted in Fig. 7.1. A sinusoidal electric signal generated by a function generator (SG 380, Stanford Research Systems, Sunnyvale, CA) and high frequency amplifier (ZHL-1-2W, Mini-Circuits, Brooklyn, NY, USA) was used to drive a 127.86° Y-rotated X-propagating cut of lithium niobate ($LiNbO_3$ (LN), 500 μm thick, Roditi, London, UK) surface acoustic wave device via a simple unweighted Al/Cr interdigital transducer [35] of 28 finger pairs deposited using lift-off lithography [16] with gap and finger widths of 10 μm ($\lambda_{SAW}/4$), producing a resonant frequency of $f_s = c_s/\lambda_{SAW} =$ 100 MHz. A 3 $\mu\ell$ deionized (DI) water sessile drop with a 0.1 $\mu\ell$ Fe_3O_4 NP in toluene (5 mg/mL) was placed on LN (Sigma Aldrich, St. Louis, MO, USA). The particles were strongly bound to the free interface of the droplet by surface tension [200]. The SAW

passes acoustic energy into the drop at the Rayleigh angle, $\sin^{-1}\theta = c_l/c_s = 22°$, where $c_l = 1485$ m/s is the speed of sound in water, producing acoustic streaming in the sessile drop [201]. A reasonable estimate for the maximum particle velocity in a media continuously supporting an acoustic wave without failure is $\sim$1 m/s and independent of the resonant frequency [116]. At 100 MHz, the SAW displacement amplitude is extremely small at $\mathcal{O}(1$ nm) but produces an extremely high surface acceleration of $\mathcal{O}(10^8 \mathrm{m/s}^2)$. Despite this, in our experiments in this study, the shape of the drop did not change nor oscillate, due to the low power SAW used here.

7.2.2 Imaging tools

The morphologies and radii of the Fe_3O_4 NP were determined by environmental scanning electron microscopy (ESEM, Philips XL 30, FEI, Hillsboro, Oregon, at 10 keV; *see* Fig. 7.1(c)): the average radius of the particles is 10 nm with a standard error of 0.4% ($n = 150$). External magnetic fields of 200–400 mT were produced using magnets (Grade N42, K&J Magnet, Pipersville, PA USA) of the same 9.525 mm diameter but different thicknesses. The motion of the Fe_3O_4 NPs was recorded with a high-speed camera (FASTCAM Mini UX100, Photron, Tokyo, Japan) and microscope (K2/CF–4, Infinity, Boulder, CO USA). The images were analyzed using MATLAB (Mathworks, Natick, MA USA) and ImageJ (National Institutes of Health, Bethesda, MD USA).

7.3 Results and Discussion

Due to the useful properties of Fe_3O_4 NP agglomerates, a variety of techniques have been developed to produce 1D chains and 2D films, including alumina templating [202], electrodeposition [203], and the imposition of external magnetic fields from 0.2 to 0.6 T [204] for 1D structures and Langmuir-Blodgett films [205], spin coating [205], electrophoretic deposition [206], laser interference lithography, and emulsion[207] for 2D structures. Inevitably, weak and defect-laden structures are formed from these methods unless external forces or chemical binders are introduced which unfortunately reduce the utility of the NP chains and films [208, 209]. Moreover, the complexity and cost of these methods relegate them to a relatively small market niche [202, 210].

We present a fast, cost-effective, and additive-free approach to obtain 1D chains and 2D films composed of Fe_3O_4 NP in the presence of 0.2–0.4 T external magnetic fields and Rayleigh surface acoustic wave (SAW)-driven acoustic waves, and consider the mechanisms responsible for the self-assembly via a combination of scaling and experimental results from a simple prototype.

The phase map, Fig. 7.2, illustrates how the applied SAW power and magnetic field leads to 1D chain assembly and 2D film formation of the Fe_3O_4 NP on a 3 $\mu\ell$ sessile drop. As expected, chains of NP assemble (region I) without SAW and with or without an external magnetic force [211, 204]. The Brownian force is known to dominate and produce random floating chains in the absence of SAW and magnetic fields from dispersed suspensions of magnetic NP [211].

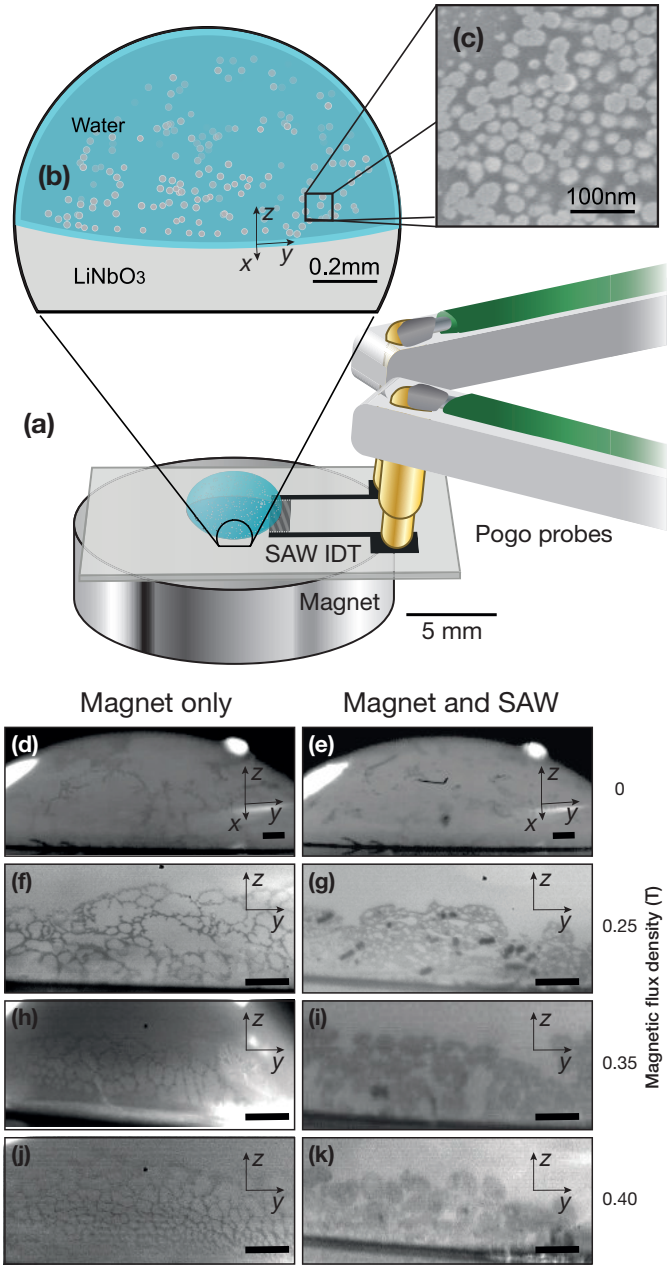

Figure 7.1: (a) A 3 $\mu\ell$ DI water sessile droplet with 0.1 $\mu\ell$ Fe_3O_4 NP produced via solvent exchange from toluene is placed upon a bare LN surface (size $\sim$ 1 mm) incorporating a 100 MHz SAW device (wavelength 40 μm). The $\sim$ 10 nm Fe_3O_4 NP (c) reside upon the fluid-air interface. With only the application of (d) 0, (f) 0.25, (h) 0.35, and (j) 0.4 T external magnetic field fluxes, respectively, 1D chains are produced; (e,g,i,k) SAW is necessary to produce 2D films. Here 10 s of SAW was applied to obtain the images (d–k: scale bar is 500 μm).

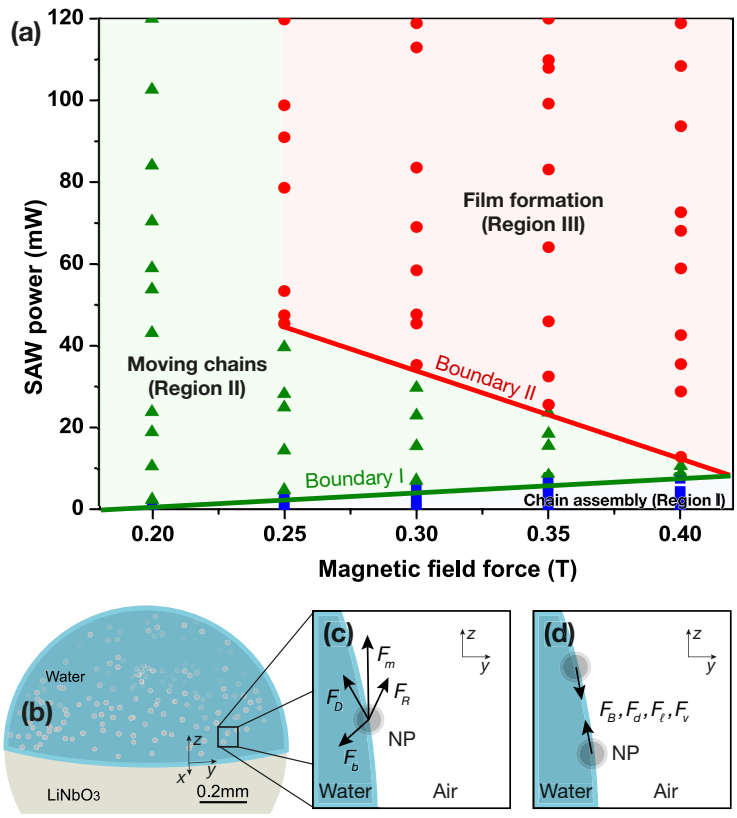

Figure 7.2: (a) Phase diagram depicting chain assembly (I), chain movement (II), and film formation (III) regions as a function of SAW power (0–120 mW) and magnetic field strength (0.2–0.4 T). Above 120 mW, the 3 $\mu\ell$ DI water droplet translates across the LN surface, so 120 mW is the upper limit in applied power for our experiments. (b) The directions of the forces experienced by the Fe_3O_4 NP present around the periphery of the drop, including the external magnetic (F_m), dipolar(F_d), Brownian (F_b), van der Waals (F_v), lateral capillary (F_l), SAW radiation (F_R), drag (F_D), and Bjerknes (F_B) forces.

Upon introducing a magnetic field, the Fe_3O_4 NPs orient along the magnetic field lines[211] in head-to-tail, dipolar aligned chains to minimize the overall dipolar potential energy [212, 213, 214]. These chains appear around the periphery of the drop and near the contact line, with a significantly reduced concentration of particles at the top of the drop. Interestingly, a dense honeycomb-like structure is formed upon application of a stronger magnetic field, believed to be due to the increase in the induced inter-particle magnetic

forces. [215, 214] The as-prepared NP states under 0.25, 0.35, and 0.4 T external magnetic field fluxes are shown in Fig. 7.1(f), (h), and (j), respectively. The average Einstein-Stokes hydrodynamic radius (r_h) of the chains is around 3 μm (Fig. 7.3(b)) using $r_h = (\frac{3\eta M}{10\pi N})^{1/3}$, where η is the intrinsic viscosity, M is the molecular weight (233 g/mol for Fe_3O_4), and N is Avogadro's number [216]. By computing the Minkowski–Bouligand (MB) dimension, d_{MB}, via box counting[217] from the NP images in Fig. 7.1, we find (*see* SI Fig. 1) that the dimension of the NP morphology remains nearly 1D with even a strong 0.4 T magnetic field: $d_{\mathrm{MB}} \approx 1.21$. Upon applying a combination of a 0.25 T or 0.4 T magnetic field and SAW, the NP morphology becomes nearly two-dimensional, with $d_{\mathrm{MB}} \approx 1.79$ or 1.92, respectively.

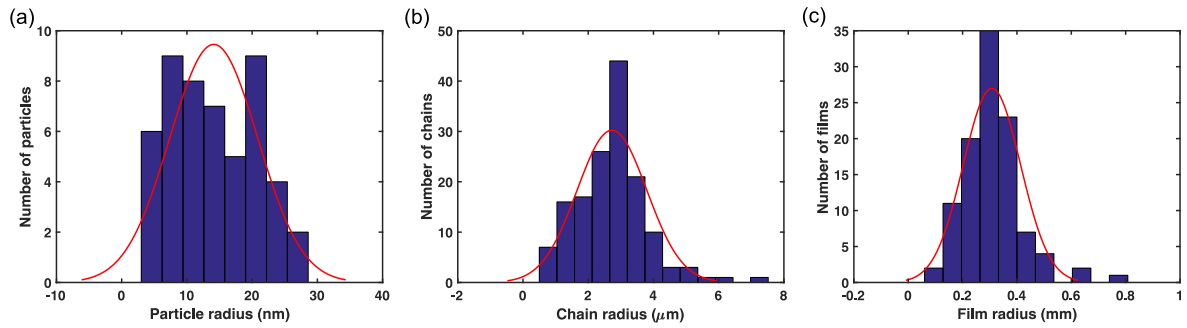

Figure 7.3: Histogram (blue bar) with Gaussian distribution (red line) plots of the (a) 0D particles, (b) 1D chains and, (c) 2D film size distributions.

Boundary I ($B \propto P_{SAW}$) is reached while increasing the SAW power P_{SAW} from zero (Fig. 7.2(a)), where B is the magnetic field strength. The boundary indicates the minimum power required to produce chain motion due to SAW-driven acoustic streaming, increasing linearly, albeit weakly with magnetic field flux, indicating that the acoustic power required to overcome the magnetic dipole-driven stability of the interlinked chains to transport

them upon the free fluid interface grows with an increasing magnetic field. Fig. 7.1(g) is representative of the NP morphology in this region: the interstitial spacing between the chains is reduced after 10 s of SAW streaming at 115 mW power while a 0.25 T magnetic field is being applied. However, a 2D film does not form.

Boundary II ($B^{-1} \propto P_{SAW}$) indicates the transition to sufficient SAW power and magnetic force to form 2D NP films. For NP chains formed under larger magnetic forces, less SAW power is needed to form the 2D Fe_3O_4 NP film. The interchain spacing is known to be reduced with stronger external magnetic forces [215, 214] and thus it is reasonable to expect this outcome. However, below 0.25 T, there is no film formation at any SAW power. The scattering of acoustic waves from the NPs and structures formed from those NPs exerts a Bjerknes force between them, the magnitude and sign of which depends upon the spacing and particle size as indicated in Fig. 7.4(b). When the interchain spacing is larger than 400 μm, the induced Bjerknes forces between the NP structures are generally constant and repulsive, separating the Fe_3O_4 NPs. When the spacing is less than 400 μm, the Bjerknes forces depend upon the spacing, but grow more negative as the spacing of the NP structures are reduced. This predicts the observed experimental results (Fig. 7.1(e)), where the average Fe_3O_4 interchain spacing is consistently $\sim$400 μm when the external magnetic force is below 0.25 T.

Crossing boundary II, region III is reached, where 2D films are formed with both SAW and magnetic fields (Fig. 7.2(a)). Figure 7.1(i,k) provide example 2D films formed in this region from 10 s of 115 mW SAW with 0.25 and 0.4 T magnetic fields, respectively. The effective hydrodynamic radii of these 2D films, $\sim$3 mm, is provided in Fig. 7.3(c). These

2D films remain intact until the water evaporates, and often remain even until dried.

Beyond 120 mW SAW power, we see droplet translation from SAW-driven acoustic streaming within and acoustic pressure on the free fluid interface that together overwhelm the drop's contact line tension [218].

To understand the chain assembly and film formation upon application of magnetic fields and SAW, we further examine the forces involved as a function of the hydrodynamic radii of the NP and chains and films formed from them. According to Newton's second law, the balances of forces on an object moving on the free fluid interface while exposed to a magnetic and acoustic field is shown in eqn. (7.1) and illustrated in Fig. 7.2(b).

$$\begin{aligned} m_p \frac{d\mathbf{v}_p}{dt} &= F_m \mathbf{e}_m + F_d \mathbf{e}_d + F_b \mathbf{e}_b + F_v \mathbf{e}_v \\ &+ F_l \mathbf{e}_l + F_R \mathbf{e}_R + F_D \mathbf{e}_D + F_B \mathbf{e}_B \,, \end{aligned} \tag{7.1}$$

where m_p is the object mass and $d\mathbf{v}_p/dt$ its acceleration; the external magnetic F_m [219], dipolar F_d [220], Brownian F_b [221], van der Waals F_v [222], lateral capillary F_l [223], primary SAW radiation F_R [224], drag F_D [225], and the Bjerknes F_B [226] forces may be present. The unit vectors $\mathbf{e}_m$, $\mathbf{e}_d$, $\mathbf{e}_b$, $\mathbf{e}_v$, $\mathbf{e}_l$, $\mathbf{e}_R$, $\mathbf{e}_D$, and $\mathbf{e}_B$ indicate the forces' direction as grouped into two categories in Fig. 7.2(b): forces present *between* the objects (F_B, F_d, F_l, and F_v) and external forces present on *all* the objects (F_D, F_m, F_b, and F_R). The forces in the latter category may be ignored: they affect all nearby objects in a similar fashion and therefore are unlikely to lead to a morphology change, *except* for the Brownian force F_b: this force is random and therefore unique to each object.

By contrast, the interparticle forces are crucially important to the NP agglomerate's

morphology, and, for any two Fe_3O_4 NPs include the dipolar force, Brownian force, van der Waals force, and the lateral capillary force [227]. The dipolar force is expressed as $F_d = \frac{6\mu_0 V_p m_p^2}{4\pi r^4}$, where μ_0=7×10^{-20} J is the magnetization of the Fe_3O_4 NP and $r = 10$ nm is the radius of each Fe_3O_4 NP [220]. The Brownian force is $F_b = \sqrt{\frac{6\pi k_B}{\Delta t} T(2r)}$, where $K_B = 1.38 \times 10^{-23}$ J/K is the Boltzman constant and T is temperature [221]. The Van der Waals force is $F_v = \frac{Ar}{12L^2}$, where $A \sim 35{\times}10^{-12}$ erg is Hamaker's constant for Fe_3O_4 in water [228] and $L = 10$ nm is the distance between two Fe_3O_4 NP [222, 229]. Finally, an attractive capillary force exists between any two Fe_3O_4 NP on the H_2O surface, expressed as $F_l = 2\pi\gamma \frac{Q_1 Q_2}{L}$, where γ is the surface tension of water, and $Q_n \simeq r_n \sin\varphi_n$ is the "capillary charge", characterizing the local deviation of the meniscus shape at the three-phase contact line due to the NP's presence, where r_n and φ_n are the radius of the contact line and the slope at the contact line with respect to the particle's surface, respectively [230, 231].

When the Fe_3O_4 NP are placed in an external magnetic field, the NPs and their magnetic moments rotate into the direction of the field and increase the magnetic flux density. The magnetic force on each NP is expressed as $F_m = \frac{V_p \Delta\chi}{\mu_o} B(\bigtriangledown B)$, where V_p is the volume of the particles, $\Delta\chi$=10^{-5} is the susceptibility of Fe_3O_4 relative to medium (water), μ_o=10^{-6} N/A^2 is the permeability of vacuum, and B is the magnetic flux density [219, 232].

Finally, the forces from the fluid upon the NP with SAW include direct acoustic radiation, Stokes drag, and Bjerknes' forces. The direct acoustic radiation force imposed by a traveling wave on an compressible particle—which the NPs are expected to be—was derived by Nadal [233] and is expressed as: $F_R = \frac{2}{3}\pi\rho_w(\xi_0 C_w)^2(k_0 r)^3(\frac{\beta-1}{\beta})\frac{\epsilon}{\sqrt{2}}$, where ρ_w is the

density of water, ξ_0 is the displacement of the incident wave, C_w is the speed of the sound in the water, k_o is the wavenumber, $\beta = \rho_w/\rho_c$, where ρ_c is the Fe_3O_4 density, and $\epsilon = (\frac{r^2 w}{v})^{1/2}$ describes the dimensionless relationship among the particle radius (r), frequency (w), and kinematic viscosity (v). Moreover, the Stokes drag upon the particle is $F_D = 6\pi\mu r v$, where μ is the viscosity of H_2O and v is the velocity difference between the surrounding fluid and the NP. Finally, Bjerknes' force, an interparticle force arising from the scattering of the incident acoustic wave, is defined as $F_B = 4\pi r^6 [\frac{(\rho_c - \rho_w)^2 (3\cos^2\theta - 1)}{6\rho_w r^4} V^2(X) - \frac{\omega^2 \rho_w (\beta_c - \beta_w)^2}{9L^2} P^2(X)]$ [226], where $V(X)$ is the particle velocity amplitude, β_c is the compressibility of Fe_3O_4 NP, β_w is the compressibility of water, and $P(X)$ is the acoustic pressure amplitude, respectively. Bjerknes' force changes in amplitude *and* from attraction to repulsion as the interparticle chain spacing increases, as shown in Fig. 7.4(b).

The primary acoustic radiation force and viscous drag force dominate for objects of radii 1 nm to 0.1 mm as shown in Fig. 7.4(b). However, both of these forces are equally present upon all the objects in the system, and consequently are irrelevant for the NP morphology. Among the remaining forces, the Brownian force dominates objects less than 100 nm in size, the magnetic field flux-derived force dominates those sized between 100 nm and 10^{-4} m, and Bjerknes' force dominates those particles larger than 100 μm in size. Consequently, a single Fe_3O_4 NP (as the average radii of Fe_3O_4 is around 10 nm) forms loosely-bound 1D chains, as shown in Fig. 7.1(d) and seen in past work [234]. Brownian forces dominate the particles at these small scales irrespective of the presence of magnetic or acoustic fields.

When particles randomly agglomerate from Brownian motion to form 1D chains sur-

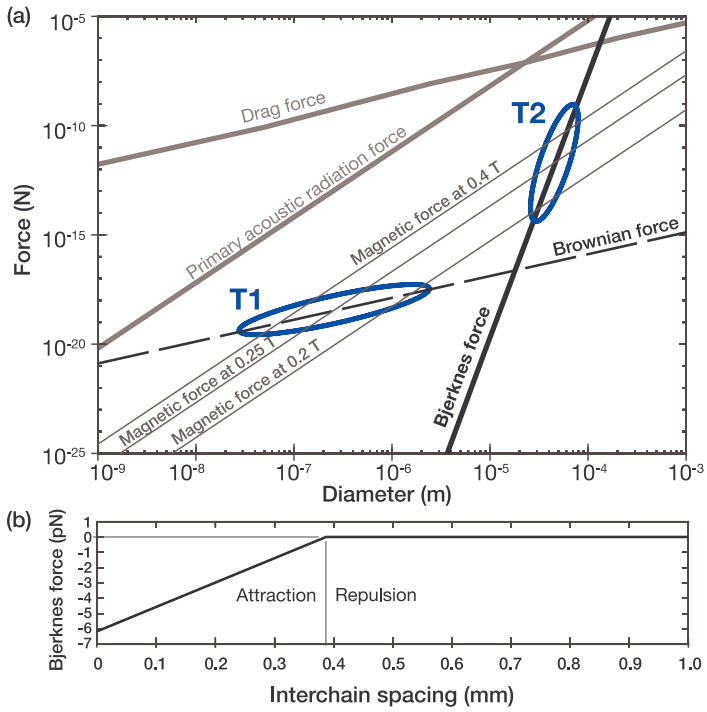

Figure 7.4: (a) Dominant forces on the Fe_3O_4 NP particles floating on the liquid surface in magnetic and acoustic fields as a function of particle radii. (b) Relationship between interchain spacing and the Bjerknes force. The critical point is 400 μm, where the Bjerknes force transits from negative to positive values (though nearly zero).

passing a hydrodynamic radius of 100 nm, application of a magnetic field causes the attractive magnetic interparticle forces to dominate the chains' behavior. Nanoparticle 1D chains of 100 nm to 10 μm size (Fig. 7.3(b)) form honeycomb-like structures that only appear upon the application of an external magnetic field. The NPs' dipoles reorient along the field, induce local magnetic fields between neighboring Fe_3O_4 NP, and drive head-to-tail, interparticle attraction that links the chains together for as long as the magnetic field is present [235, 204, 215]. The transition from Brownian motion to magnetic field-dominated behavior is denoted as the first transition point (T1) between these influences in Fig. 7.4(a).

As these chains of NPs grow in size from 100 nm to 100 μm in size and 1D to 2D in dimensionality, the secondary acoustic force present between the objects, or NP agglomerates, due to interparticle acoustic scattering—the Bjerknes force—grows to dominate. The force can either be repulsive (positive) or attractive (negative) depending on object size and interobject separation distance [226]. Because in our system we are growing the size of the interacting objects from the starting individual NPs, we consider the 10 μm sized objects already present as the Bjerknes force begins to dominate. These objects are widely spaced as 1D chains across the fluid interface. When the spacing between these objects is *reduced* below about 10 μm from the action of the magnetic field and aided by jostling of the objects by the overall acoustic field, acoustic streaming, and fluid drag, the Bjerknes force becomes attractive and acts to drive the agglomerated objects even closer together, triggering the formation of 2D films of the NPs. These films remain intact long after removal of both the magnetic and acoustic fields, until evaporation grows to dominate.

7.4 Conclusions

The growing interest in acoustic manipulation of particles in micro to nanofluidics using surface acoustic waves, together with the many applications of magnetic nanoparticles—whether individual or in arrays—underpins our discovery of how these forces can be used to rapidly, easily, and irreversibly form 1D chains and 2D films. These films and chains are difficult to produce by other methods yet offer many advantages over suspen-

sions of individual nanoparticles by making use of the scale of the structures formed, 109 to 105 m, and by taking a balance of the relevant external and interparticle forces, the underlying mechanisms responsible for the phenomena become apparent. For loosely connected 1D chains, the magnetic field alone is sufficient, though applying an acoustic field drives a topology change to interconnected loops of ∼10–100 particles. Increasing the acoustic field intensity drives a transition from these looped structures to dense 2D arrays via interparticle Bjerknes forces. Inter-particle drainage of the surrounding fluid leaves these structures intact after removal of the externally applied forces. The self-evident morphology transitions depend solely upon the relative amplitudes of the Brownian, Bjerknes, and magnetic forces.

Chapter 7 in full, is a reprint of material appears in Applied Physics Letters 2018. Huang, An; Miansari, Morteza; Friend, James., Applied Physics Letters 2018. The dissertation author was the primary investigator and author of this paper.

Chapter 8

The vibration behavior of submicron gas vesicles in response to acoustic excitation determined via laser Doppler vibrometry

8.1 Introduction

Microbubbles, made stable through tailored coatings, are useful across many disciplines—especially in medicine, pharmacology, materials science, food engineering, and water treatment. [236, 237, 238] They have long been [236] injected into humans and animals alike for ultrasound imaging as a contrast agent, [239] exploiting their significant contrast difference with the surrounding tissue and their safe dissolution and resorption after a few

hours. When functionalized, they are especially useful for delivering drugs and genetic material and serving as cavitation nucleation sites for disrupting tumor cells. [240] Researchers are exploring ultrasound imaging into interstitial regions and across vessel walls in tumors where traditional microbubbles are too large to penetrate, driving interest in submicron to nanoscale bubbles. [241] Moreover, reducing the bubble size increases their number density for the same total bubble volume, improving the resolution and specificity of multimodal imaging and therapeutic applications. [242]

Bubbles of whatever scale are known to oscillate in response to incident ultrasound pressure waves, scattering the ultrasound through the surrounding medium. Ultrasound contrast-aided imaging relies upon the detection of nonlinear signals from the bubbles that arise when the oscillation amplitudes become large, [236] and the details of micro-sized bubble oscillation have and continue to be theoretically and experimentally studied. [243] Because bubbles are multi-phase systems, with a gas surrounded by liquid and perhaps a third media as the coating at the interface to stabilize the gas, any analysis should first be divided into free and coated bubble treatments, producing a significant difference in the complexity of the analysis. [244] For free bubbles, the contained gas is directly in contact with the liquid surrounding it. However, the Laplace pressure is sufficient to require a stabilizing coating on submicron to nano-scale bubbles to avoid their premature resorption. [236] Gas vesicles (GVs) are a family of gas-filled protein nano-sized structures naturally expressed by photosynthetic microbes as a means to achieve buoyancy in water, [245, 246, 247, 248] offering a number of advantages peculiar to their small size and characteristics. The potential benefits of purified nano-scale GVs include ultrasonic

imaging to unprecedentedly tiny regions of vasculature and the interstitial space within tumors. [249, 250, 251] Recently introduced acoustic reporter gene cassettes can be used for the imaging of gene expression into deep tissue, through conditional production of GVs in engineered bacteria [252] and mammalian cells. [250] Despite the free diffusion of gas through them, the GVs' amphiphilic shells make them physically stable for long periods of time—weeks to months—both within these microbes and without. They can withstand external pressures of hundreds of kilopascals without collapsing. Further, the GVs can self-assemble into long-range ordered structures without external application of any forces. [253]

While GVs offer many advantages due to their small size, because they are so small, their vibrations under ultrasound stimulation are difficult to observe using light microscopy and consequently remain poorly understood. [254]

In order to most effectively use ultrasound with bubbles, researchers have adopted imaging methods from high frame-rate microscopic imaging [255, 256, 257, 258] to the transmission and reception of ultrasound via transducers to determine the intensity of the scattered ultrasound signal. This signal is then correlated to models of the bubbles' vibration behaviors. While the transmitters in most studies are similar, different receivers are used depending on the circumstances, including paired transmitting/receiving ultrasonic transducers [259, 243, 260] and laser Doppler vibrometers (LDV). [261] Although the LDV has been reported to generate results consistent with high-speed imaging in measuring the vibration of micro-scale objects, it has so far not been used in any observation of the vibration of *submicron* objects. [262]

Most importantly, the vibration modes of GVs have not yet been directly observed. [263] Furthermore, the resonance frequencies of the GV are unknown but are expected to be greater than microbubbles—which exhibit resonances in the megahertz range—and potentially could reach gigahertz frequencies. In addition, numerical models predict GV buckling across a wide range of ultrasound pressure levels, potentially producing strong nonlinear signals, [263] though these have not yet been observed. In this paper, we propose to use laser Doppler vibrometry to observe the GVs' vibration behavior. Unlike widely used techniques for understanding microbubble vibration that fail at the submicron scales of GVs, LDV employs interferometry, offering far better spatiotemporal resolution of up to 2.4 GHz in frequency and for motions as little as 200 fm. [51] However, we must agglomerate the GVs to a size greater than the wavelength of the laser used in the LDV, in our case 532 nm, in order to make them observable. We further must pin the GVs to a surface to enable reliable LDV observation. Using analysis borne from theoretical models and computations, we show how these acts only weakly affect the experimentally observed resonant *frequencies* of the GVs, with a fundamental resonance at 1 GHz and the first harmonic at 1.7 GHz. In agglomerating the GVs to ∼615 nm, we identify the existence of a new vibration mode from the entire agglomeration at ∼300 MHz. Finally, we elucidate the GVs' responses to a controlled, acoustically-delivered pressure at a clinically-relevant 7 MHz, representing excitation well away from their individual and agglomerate resonances, all the way to buckling and collapse. To our knowledge, this is the first time that the vibration behavior of nano-sized GVs have been directly measured, and furthermore the first time that an LDV has been used to measure the motion of nano-scale

objects.

8.2 Experimental methods

8.2.1 Gas vesicles preparation

The GV used for this study is Anabaena flosaquae (Ana) GV (CCAP 1403/13F, Culture Collection of Algae and Protozoa, Scottish Marine Institute, Oban, UK), produced by a green filamentous cyanobacterium that naturally inhabit freshwater lakes.[248, 264] The GVs were purified from these cells as previously described[264]. A standard quality assurance step in which outer diameter measurements were taken at 0–120 kPa was performed for each sample. These measurements were carried out using a system composed of an echoVis Vis-NIR light source coupled with an STS-VIS spectrometer (Ocean Optics, Largo, FL USA), and a 176.700-QS sample chamber (Hellma Analytics, College Park, GA USA). Next, the external shell protein GvpC was removed from the GVs to produce the harmonic GVs used in this study.[264] Finally, the GVs were clustered using sulfo-NHS-biotin (10,000-fold molar excess, Thermo Fisher Scientific, Carlsbad, CA USA) and streptavidin (100-fold molar excess, G-Biosciences, St. Louis, MO USA), facilitating dense GV binding to our LDV setup. [264] Sufficient GVs are present to produce laterally dense agglomerations, and unbound GVs are removed before the experiment. The clustering also enabled sufficient reflection of the 532-nm laser light in our LDV measurements via the setup illustrated in Fig. 8.1(a-d), producing a low-noise displacement measurement signal. The mean size of the GV clusters was 615.3±24.5 nm, determined with dynamic

light scattering measurements (Zetasizer Nano ZS, Malvern Pananalytical, Worcestershire UK). The measured optical density was 11.4. Details of the preparation and handling process may be found in the previous literature. [264] The utility of the GVs in ultrasonic imaging is illustrated via its the signal magnification ability through an agar phantom scan provided in Fig. 8.2.

8.2.2 Single-crystal lithium niobate transducer

The 5 mm wide × 8 mm long thickness-mode transducers used as acoustic sources in this study were diced from 500 μm thick, 100 mm diameter, double-side optically polished, 127.86 Y-rotated, X-propagating single-crystal lithium niobate (LN) wafers (Roditi, London, UK) chosen for their superior thickness mode performance as described in detail elsewhere.[175] Electrodes were formed on both faces of the wafer prior to dicing using sputter deposition of 500 nm of gold. The acoustic energy generated by these transducers was in part coupled to the GVs via a thin fluid meniscus through the arrangement shown in Fig. 8.1(a–d). This was done to minimize both the direct measurement of the transducer's motion by the LDV and the indirect measurement of any possible motion of the fluid meniscus covering the Au-bound GVs that might arise in other arrangements. The transducer was placed at 45° to avoid blocking the LDV laser. An acrylic mounting, omitted for clarity, was used to hold the transducer and LN-gold substrate in place.

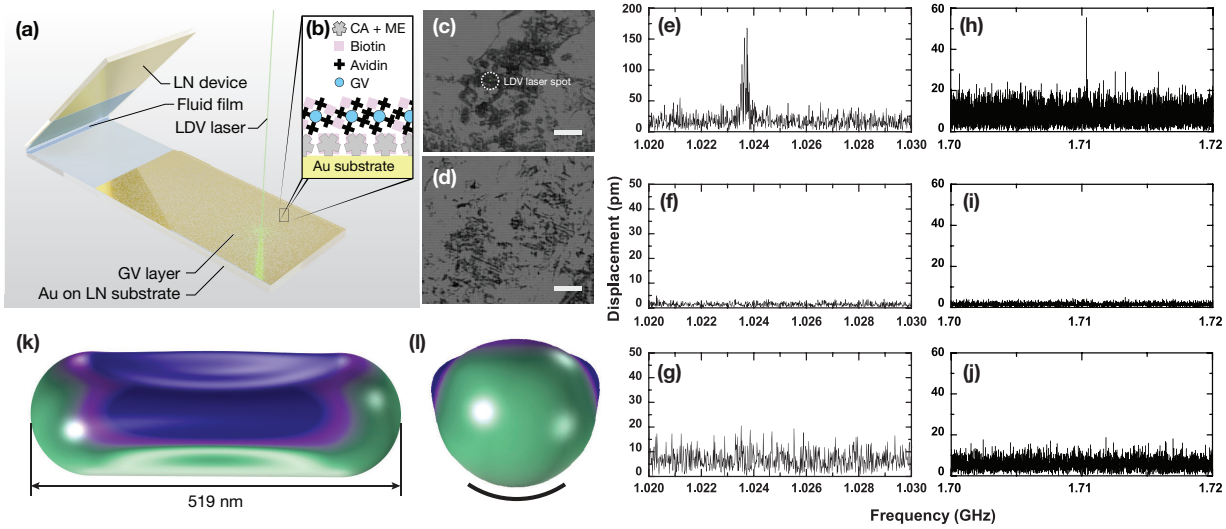

Figure 8.1: The (a) LN transducer is coupled via a thin fluid film spread across a second gold-LN substrate with a 45° angle between them. This arrangement ensures effective acoustic wave transmission into the fluid film while avoiding occlusion of the LDV. The avidin-conjugated GVs are (b) bound to the gold substrate via biotin and CA+ME. Transmitted light microscopy of the as-bound GVs indicates (c) intact GVs, and (d) collapsed GVs after exposure to intense (330 kPa) harmonic acoustic pressure at 6.5 MHz (c,d: scale bars are 20 μm), the fundamental thickness-mode resonance frequency of the LN transducer. The green dot in (c) represents the size of the LDV laser measurement spot used to produce the (e-j) LDV spectra using an acoustic pressure of 38 kPa. Ten trials were conducted, and these results were identical to the resolution of the LDV to those plotted here. A (e) fundamental linear resonance peak appears at 1.025 GHz only in the presence of the GVs; it is absent with (f) only the gold substrate and (g) after the GVs have been collapsed using an acoustic pressure of 400 kPa at 6.5 MHz. No response peak exists for the GVs below this frequency, except for a response at ∼300 MHz discussed later. The next resonance peak to appear, the first harmonic, is (h) at 1.71 GHz with GVs, and is once again absent with (i) only the gold substrate or (j) the GVs after their collapse. These results are on the same order as predictions from the modified Rayleigh-Plesset equation (*see* text) and closely correspond to the predicted fundamental resonance frequency, 1.09 GHz, from computational analysis. The corresponding ((k) side view and (l) end view) fundamental resonance mode shape is provided for a 519 nm-long, 140 nm radius GV, taking into account both the fluid loading and the surface binding as explained in the methods. The heavy curved line indicates the region of binding in the (l) end view.

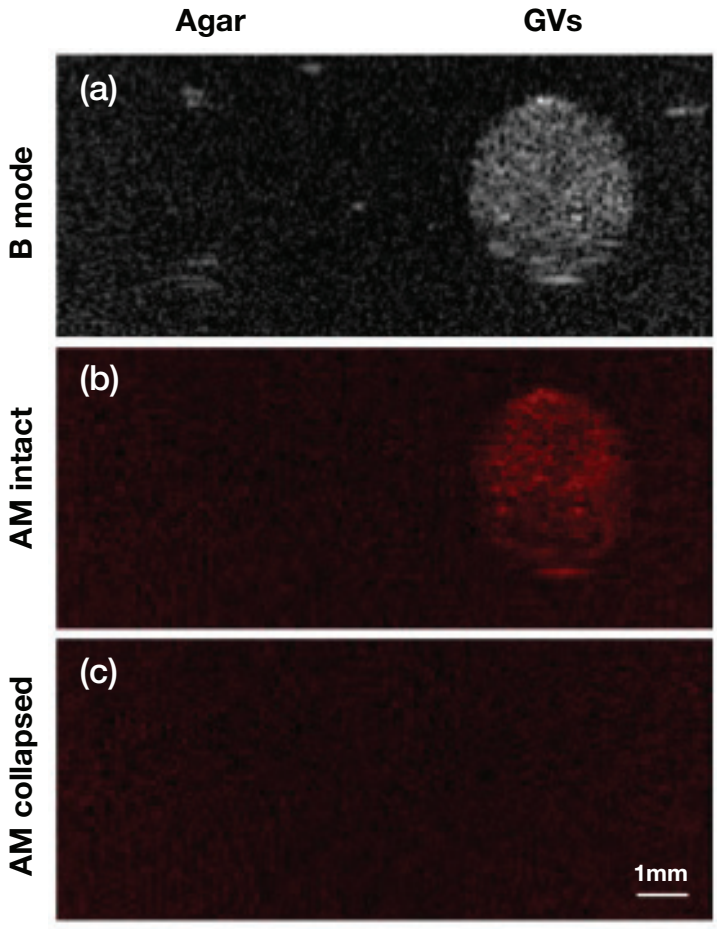

Figure 8.2: Linear and non-linear ultrasound contrast images of stripped Ana GVs. (a) The linear contrast of GVs can be detected using an anatomic B-mode ultrasound scan at 18 MHz. The result of the scan for an agar-filled well is provided for comparison on the left. (b) The non-linear contrast of stripped Ana GVs can be observed using the amplitude modulation pulse sequence. (c) If necessary, the GVs can be "erased" via apparent collapse using high pressure; in this case 2.09 MPa ultrasound from a commercial transducer.

8.2.3 LN-gold substrate for streptavidin-biotin binding of the GVs

The gold surface was modified to attach the GV through biotin-avidin bonding as detailed in the literature. [246] The devices were first cleaned through hexane, ethanol, and deionized water, and then finally dried using compressed dry, clean air. The devices were then immersed into a solution contains 0.05 M cystamine dihydrochloride (CA, Sigma Aldrich, St. Louis, MO, USA) and 0.05 M 2-mercaptoethanol (ME, Sigma Aldrich) with DI water as solvent to create sulfur bonds on the gold substrate. After leaving the devices immersed for 24 hr to await completion of the bonds, they were removed and carefully rinsed with deionized water and ethanol before drying them using compressed dry, clean air. The devices were then immersed into a NHS-biotin solution prepared through the reaction of biotin (Sigma Aldrich) mixed with 0.12 mol N,N-diisopropylethylamine (DIPEA, Sigma Aldrich), O-(N-succinimidyl)-N,N,N′,N′-tetramethyluonium (TSTU, Sigma Aldrich, in 10 ml N,N-dimethylformamide (DMF, Sigma Aldrich) solution. At this point, the NHS-biotin bonding on the gold substrate has been established. We then pipetted a 1 mL avidin-GV solution onto the NHS-biotin-gold substrate and waited 30 min to ensure sufficient biotin-avidin bonding on the gold substrate. The devices were subsequently rinsed with deionized water to remove unbound GVs.

Fourier-transform infrared spectroscopy using a liquid nitrogen cooled MCT detector (FTIR, Perkin Elmer, Waltham, MA, USA) was used to confirm NHS-biotin bonding on the gold substrate. Fifty patterns were accumulated at a resolution of 4 cm^{-1} for a single

run.

8.2.4 LDV measurements of GV responses to acoustic irradiation

The flat, GV-bonded gold layer was placed perpendicularly to the laser from the LDV; the laser was passed through a 50x lens (M-plan 50x objective, Mitutoyo, Kanagawa Japan) to reduce the depth of coherence (akin to the depth of field) to about 1 μm for observation. A thin layer of deionized water was added onto the surface of the bottom substrate with a fluid bridge to the transducer as a means to couple the acoustic wave from the transducer onto the inert substrate with GVs bonded to its surface; the gold was mildly hydrophilic in this study, and the fluid bridge was therefore stable. The depth of the water layer was set at 1 to 2 mm, much larger than the wavelength of the acoustic wave, but sufficiently thin to facilitate observation of the GV's surface morphology through LDV. A sinusoidal electric signal from a function generator (SG 380, Stanford Research Systems, Sunnyvale, CA) was used to drive the transducer via a high-frequency amplifier (ZHL–1–2W, Mini-Circuits, Brooklyn, NY, USA) from 9 kHz to 2 GHz. The excitation was non-resonant for a vast majority of this frequency range, but sufficient to drive GV motion observable by the LDV. Near the fundamental thickness-mode resonance at 6.5 MHz of the transducer, the acoustic pressure that could be generated by the transducer was 10 to 400 kPa, sufficient to examine GV collapse according to predictions in the literature. [265, 264]

We performed finite-element modal analyses of the GVs (COMSOL Multiphysics 5.4,

COMSOL, Burlington, MA USA) to determine the resonance frequencies and modes of a single GV. The elongated GV capsule—or *allantoid*—GV dimensions were 140 nm diameter and 494 to 544 nm total length with a Young's modulus $E = 3$ GPa, Poisson's ratio $\nu = 0.34$ and density $\rho = 1320$ kg/m^3. [266] The thickness of the membrane was modeled as 2 nm based on reports from the literature. [254] A portion of the cylindrical shape along the long edge equivalent to one-eighth of the total surface area was fixed to simulate the strong biotin-avidin bonding between the GV and gold substrate. [267] Based on results from a lumped constant approximation, [268] the effect on the resonance frequencies by damping of water was negligible, allowing us to neglect the effects of surface tension and thermal conductivity.

8.3 Results and Discussion

8.3.1 Resonant response of GVs

Using the LDV to measure the vibration of agglomerated avidin-biotin-bound GVs, we identified two well-defined Lorentzian [269] resonance responses centered at 1.025 GHz (Fig. 8.1(e)) and 1.71 GHz (Fig. 8.1(h)) that appear from linear response to excitation from the transducer: the measured frequency corresponds to the excitation frequency over the frequency range of the plots. These responses represent a physical motion of the GVs, as the motion of the gold substrate in their absence (Fig. 8.1(f,i)) lacks these responses, and other aspects of the experiment are controlled to maintain identical conditions.

Consequently, we next consider whether these motions represent individual GV vibra-

tion, and whether the motions correspond to coated bubbles where the coating acts to reinforce the bubble's rigidity. We employ a theoretical model [266] derived to determine such bubbles' resonance frequencies,

$$f_s^2 = \frac{3}{\rho_l R^2} K_v. \tag{8.1}$$

Here the compressibility is $K_v = \kappa P + \frac{4}{3}\frac{\chi}{R}$, where χ is the elastic compression modulus and $\kappa \approx 1$ is the polytropic exponent. By comparison, the compressibility of non-coated, free bubbles is instead $K_v = \kappa P + \frac{3\kappa-1}{3}\frac{2\sigma_w}{R}$ with σ_w as the surface tension between water and air. Here, we equate the model's spherical volume to the volume of the allantoid GVs' volume to give $R^2 = 1.69\times10^{-14}$ m^2 for the radius of the sphere, squared, and $\rho_l \sim 1000$ kg/m^3 and $K_v \sim 10^7$ Pa, [265] producing a fundamental resonance frequency of $\sim 10^9$ Hz.[1] This result is a similar order of magnitude to the resonance frequencies observed in our experiments. Damping is omitted as $ka \ll 1$, and doing so substantially simplifies the analysis. The prediction from these equations for the resonance of the ~ 615 nm GV *agglomeration* is much lower, an order of magnitude of 100 MHz, and in fact a separate resonance of the GV agglomerations appears at ~ 300 MHz as discussed later.

In the past, the resonance frequency of GVs has been posited to be anywhere from a few kilohertz to a few megahertz, [249] and, compared to these estimates, our results here rather closely correspond to our experimental observations. The correspondence

[1]The actual estimate from eqn. (8.1) is about 1.5 GHz, but this prediction presumes the objects are spherical, and the GVs are allantoid. The analysis is therefore used to solely *estimate* the order of magnitude of the resonance frequencies. For the spherical bubbles to specifically produce a 1 GHz resonance, they would need to have a diameter of approximately 240 nm.

also indicates the GV is a nano-sized bubble coated with a significant elastic membrane. Treating them otherwise, as explained in detail in the Supplemental Information, produces flawed resonance frequency predictions.

As hollow structures with significant elastic shells, it should be possible to collapse the GVs with sufficient acoustic pressure, and the collapse may be permanent. Figure 8.1(g,j) shows that after applying 400 kPa at 6.5 MHz, the resonance frequency of our transducer, LDV measurements of the exposed GVs around 1.025 and 1.71 GHz have disappeared. Only noise remains, a consequence of the poorer reflectivity of the GVs, and otherwise resembling the response of the gold substrate alone (Fig. 8.1(f,i)). The disappearance of the signal may come from the collapse of the GVs, later considered in detail.

In seeking to better understand the effects of surface binding and agglomeration, we conducted computations to estimate the resonance frequencies and mode shapes of individual fluid-loaded and surface-bound GVs corresponding to those used in the experiments. The fundamental resonance of individual, surface-bound unagglomerated GVs is predicted by computation to be 1.047 GHz, within 0.9% of the experimentally measured (1.025 GHz) value, and producing a mode shape as illustrated in Fig. 8.1(k,l). Remarkably, agglomerating or binding the GVs only weakly affect their resonance frequencies (*compare* Figs. 8.3 to 8.5), from a frequency of 0.992 GHz for an individual GV when completely free to 1.09 GHz when bound to a surface as an individual GV and 1.06 GHz when bound and agglomerated to another two GVs—representing the more general case. While this may seem peculiar, it is important to keep in mind that the volume of entrapped gas remains fixed despite these changes in the binding, and consequently the resonance *frequencies*

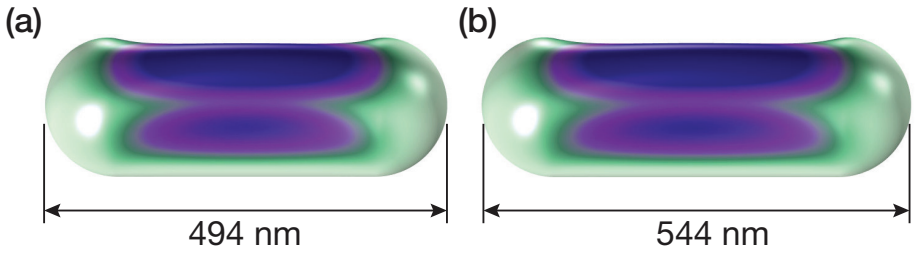

Figure 8.3: The computed mode shapes of a surface-bound GV, with one-eighth of the cylindrical portion of the GV nearest the bottom fixed in place, representing binding to a surface. The length of the GV is different (a) 494 nm and (b) 544 nm with resonance frequency at 1.092 GHz and 1.088 GHz, respectively, within 4.3% of the experimentally measured fundamental resonance frequency at 1.047 GHz.

described in large part by the oscillation of those gas bubbles should not be expected to drastically change. However, it is equally important to note that the resonance *shapes* are predicted by computation to be strongly affected by the binding, an aspect difficult to measure via LDV or another method.

There is another curious phenomena. While the minor diameter of the GV is generally constant, its length can vary depending on growth time and conditions, from a sphere to a long allantoid. [254] We knew a diversity of GVs was present in our samples, yet the resonant response was consistently well-defined and invariant. As indicated from Supplemental Fig. 8.3, the effect of varying the length of the GV only weakly affects the resonant response. Specifically, the change in the fundamental resonance frequency f with respect to GV length, L, is $df/dL = 0.002$ GHz/nm for $494 \leq L \leq 544$ nm, and so this is why we see a consistent set of resonances throughout (*see* Fig. 8.4).

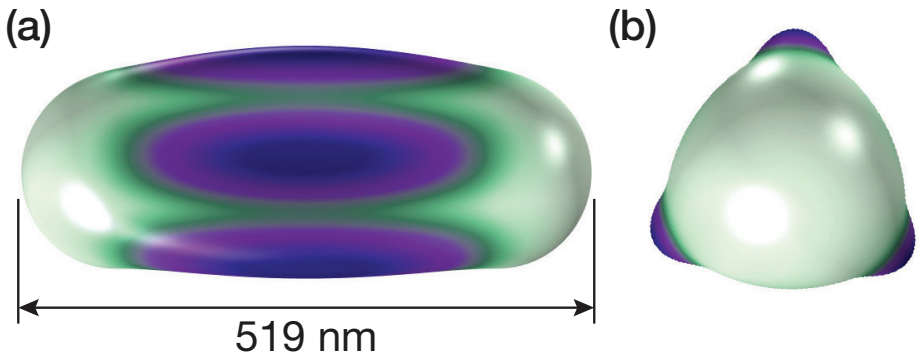

Figure 8.4: A GV completely free to move produces a computed fundamental resonance frequency of 0.992 GHz, remarkably only 6.8% less than the measured fundamental resonance frequency of 1.047 GHz for bound and agglomerated GVs.

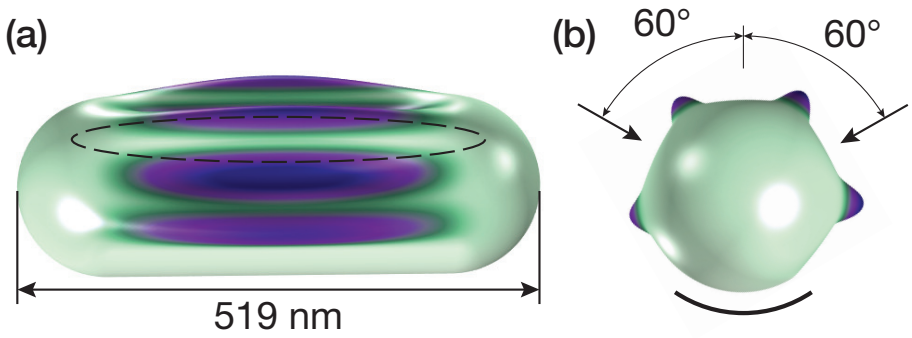

Figure 8.5: The computed mode shapes of a surface-bound GV; with it bound with other GVs at 60° from the vertical via symmetry boundary conditions. The boundary conditions are applied along lines defined upon the GV's cylindrical portion, one shown and one hidden upon the back side of this GV; and one-eighth of the cylindrical portion of the GV nearest the bottom fixed in place as indicated with the heavy curved line in the end view. Each symmetry-bound agglomeration line lies 45° from the vertical and is along the cylindrical portion of the allantoid shape. The fundamental resonance frequency produced by this object is 1.06 GHz, 1.2% above the 1.047 GHz resonance found for the GVs in our experiments.

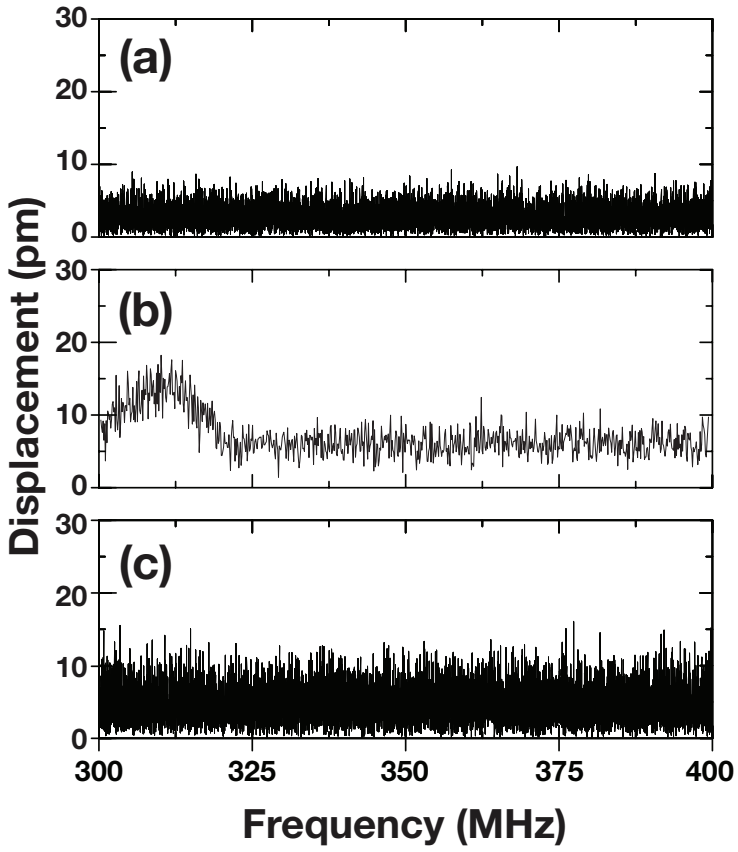

Figure 8.6: The LDV-measured displacement response from 300 to 400 MHz from narrowband driven vibration at (a,b) 38 kPa for (a) a biotin-coated gold substrate without GV agglomerates, and (b) GV agglomerates upon the gold substrate. After exposure to 400 kPa at 6.5 MHz, a return to measure the response of the (c) GV agglomerates to 38 kPa from narrowband-driven vibration from 300 to 400 MHz shows the response has disappeared, likely indicating the GVs' collapse.

8.3.2 Resonant response of GV agglomerates

At frequencies significantly lower than the resonance frequencies of the individual GVs, the sole significant response from the system beyond 6.5 MHz is a small but prominent response peak at around 300 MHz. The peak has a maximum displacement of about 18 pm (*see* Fig. 8.6(b)) in linear response to a narrowband 38 kPa sweep excitation from 300 to 400 MHz. This peak is only present with GVs: the biotin-treated gold substrate shows no such response in Fig. 8.6(a), and the response peak disappears as shown in Fig. 8.6(c) after exposure to 400 kPa, 6.5 MHz acoustic waves that appear to collapse the GVs.

The mechanism responsible for these 300 MHz peaks (Fig. 8.6(b)) may be the resonant vibration of the GV agglomerates as a whole. The measured vibration responses obtained here are broader and weaker than the individual GV resonant responses observed at 1 GHz and beyond (Fig. 8.1(e,h)). Furthermore, the response frequencies at around 300 MHz can vary from experiment to experiment between 280 to 320 MHz (Fig. 8.6), unlike the nearly identical results obtained for the resonances of the individual GVs.

The slight variation in observed resonance frequencies—from 280 to 320 MHz—is correlated with a measured variation in the size of the GV agglomerates, 589 to 640 nm. If we treat the agglomeration as a collection of cavities with a known void fraction, U, we may calculate [270] the collective resonance frequency, $f_U = (2\pi R)^{-1}\sqrt{3\gamma P/\rho U}$, where P is the static pressure within a gas-filled structure in the absence of the ultrasound, and the ratio of specific heats $\gamma = 1$. If we assume the aggregated structure size is 615 nm as provided from our dynamic light measurements, the presumption that $f_U = 300$ MHz

then produces [271] a void fraction $U = 3\gamma P / \left[\rho \left(2\pi R f_U\right)^2\right] \sim 10^{-4}$, a reasonable value. If we then use $U \sim 10^{-4}$ as the void fraction for our GV agglomerates, the range of observed agglomerate sizes in our study of 589 to 640 nm produces a commensurate shift in f_U from 313 to 289 MHz, reasonably similar to the observed range of these GV agglomerates' resonance frequencies, 280–320 MHz.

8.3.3 Vibration response of GVs to medically relevant ultrasound

We next examine the GVs response to lower frequency acoustic sources typical in medical imaging, as they are anticipated to be especially useful as ultrasound contrast media. The GVs act to *nonresonantly* amplify the response from ultrasound at 6.5 MHz as shown in Fig. 8.7(a,b), though the response is also observed to be broader and noisier with GVs (Fig. 8.7(a)) than without (Fig. 8.7(b)). The increase in noise is likely from the LDV measurement: the intensity of the specularly reflected laser light from the GVs is significantly less than from the gold substrate, leading to a noisier result in this and the previous LDV results when GVs are present.

To quantify the nonresonant amplification of ultrasound from the presence of the GVs, we used the Rayleigh-Plesset equation to represent the vibration behavior of the bubbles, modified to take into account the presence of the elastic shell. The original Rayleigh-Plesset model [272] relies upon the Rayleigh equation [273] to describe the vibration of free uncoated bubbles with only surface tension, the viscosity of the surrounding liquid,

and pressure as a function of time into consideration, producing

$$\rho R\ddot{R} + \frac{3}{2}\rho\dot{R}^2 = p_i - p_{\text{atm}} - \frac{2\sigma}{R} - \frac{4\mu}{R}\dot{R}, \tag{8.2}$$

where ρ is the density of the liquid surrounding the bubbles, p_{atm} is the ambient pressure, and μ is the viscosity of the fluid. To incorporate the shell structure of the GV, the pressure expression on the right-hand side of eqn. (8.2) needs to be modified to produce[265]

$$\begin{aligned}\rho_l\left(R\ddot{R} + \frac{3}{2}\dot{R}^2\right) = p_{\text{atm}}\left[\left(1 - \frac{3\kappa\dot{R}}{c}\right)\left(\frac{R_0}{R}\right)^{3n} - 1\right] - p_s(R) - \frac{R}{c}\dot{p}_s(R) \\ - p_L(R) - \frac{R}{c}\dot{p}_L(R) - \frac{4\mu\dot{R}}{R} - \frac{4\mu R}{c}\left(\frac{\ddot{R}}{R} - \frac{\dot{R}^2}{R^2}\right) - p_h - P_a(t),\end{aligned} \tag{8.3}$$

where R, $\dot{R}$, and $\ddot{R}$ are the GV's radius and its derivatives, and R_0 is its equilibrium radius. In addition to the ambient pressure p_{atm} and hydrostatic pressure p_h, the effects of pressure differential p_s and Laplace pressure caused by shell-liquid interfacial tension p_L are taken into account, and μ is the viscosity of the surrounding liquid. The speed of sound in the surrounding liquid is c, the polytropic index $\kappa = 1.4$ for a perfect gas, and p_a is the acoustic pressure. The acoustic pressure applied to the GVs is difficult to measure and thus we estimated it from the vibration amplitude in Fig. 8.7(b) of the gold surface the GVs are directly bonded to. The acoustic pressure is determined from first principles as $p_a = \rho_s c^2 k\delta$ with ρ_s as the density of LN (as the gold is a very thin layer and therefore mechanically insignificant here), k the wavenumber, and δ the displacement amplitude of the gold surface. In our case, $\rho_s = 4650$ kg/m^2, $k = \frac{2\pi f}{c} = 6.28\times10^3$ m^{-1} and

$c = 6.6 \times 10^3$ m/s. To overcome the effects of noise in Fig. 8.7(b), we least-squares fitted the data to a Lorentzian function and used the result to complete our calculations via the Rayleigh-Plesset equation, indicated in Fig. 8.7(a) in comparison to the experimental results. It can be seen from Fig. 8.7(a) that prediction of displacement of GVs with Rayleigh-Plesset model is larger than the LDV measurements. This discrepancy is not surprising given the spherical bubbles assumed in the model and allantoid GVs in reality, though the results are of a similar order of magnitude.

8.3.4 The buckling and collapse of GVs

Buckling is a particularly interesting nonlinear phenomenon with coated bubbles, and appears upon driving large oscillations in or upon applying large forces to the bubbles. When oscillations are small, it is known[274] that the bubble exhibits radial oscillations and the bubble coating is subjected to significant in-plane stresses that, with growth in the oscillation amplitude, begin to exhibit a non-linear response that becomes non-uniform over the bubble surface and leads to buckling.

To obtain sufficient acoustic pressure from our system to induce buckling, we chose the fundamental thickness mode resonance of our piezoelectric transducer, 6.5 MHz, far below the resonance frequencies of the GVs or the GV agglomerates. Buckling and collapse of the GVs will consequently rely upon intense ultrasound rather than any resonant amplification. With sufficient input power to the transducer, we were able to obtain acoustic pressures of 89 to 400 kPa, as calculated via the equation of state and the LDV-measured vibration amplitude on the surface of the acoustic device with $p_a = \rho_s c^2 k \delta$, determining the pressure

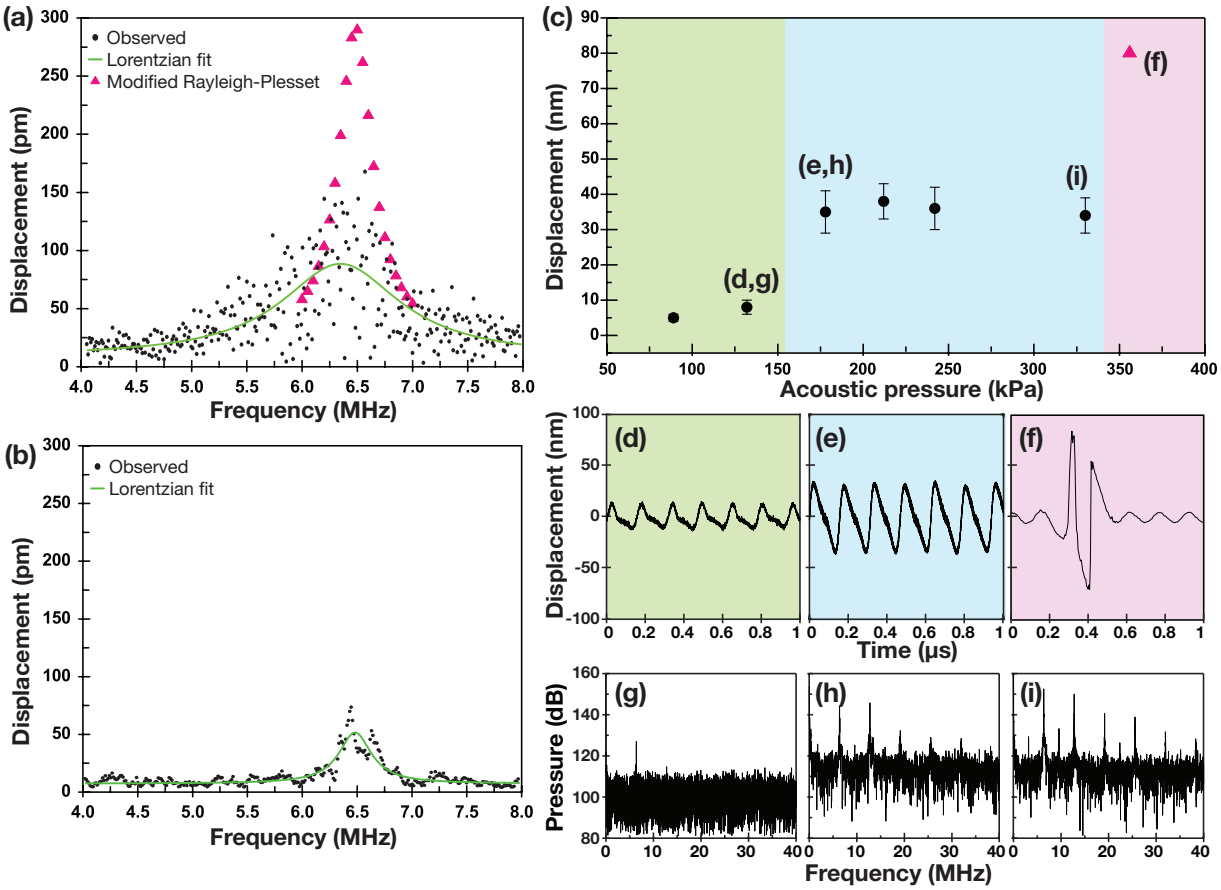

Figure 8.7: The frequency response of the GVs to 38 kPa acoustic pressure oscillations from 4.0 to 8.0 MHz (a) on the gold substrate is both larger and broader than (b) the gold substrate alone as measured using an LDV. Using the Rayleigh-Plesset equation with modifications by Cherin to accommodate the presence of the elastic shell (a, R-P results), the amplitude of the vibration is predicted to be 160 pm, larger than but comparable to the experimental results. The (a,b) fitted data is a least-squares fit to a Lorentzian response typical of a linear resonant dynamic system. The maximum peak height of the curve in (a) is 77.54 pm and in (b) it is 54.07 pm. The half-peak widths for the fitted curves in (a,b) are 1.4471 MHz and 0.397 MHz respectively. The vibration response of the GVs to 6.5 MHz large amplitude excitation. As the acoustic pressure is increased, (c) the LDV-measured displacement of the GVs grows nonlinearly, with three key regions. The GV response to (d) relatively low-pressure excitation is typical of bubble vibration responses over time. Upon (e) increasing the amplitude of the excitation pressure, the GV displacement (c) plateaus at about 40 nm, showing (e) the characteristic sawtooth response of bubbles nearing buckling. Upon exceeding 3.5 MPa excitation pressure, the (c) amplitude of the GV vibration is nearly doubled, but (f) only for a single cycle, after which the response is far lower than even for the (c,d) low-pressure excitation. The error bars represent the range of GV vibration amplitude over 1000 cycles. The frequency spectra of the GVs' radiated sound pressure due to an oscillatory excitation pressure of (g) 132 kPa, (h) 178 kPa and (i) 330 kPa, respectively, shows the appearance of a (g) linear response in the green region, followed by the (h) appearance of standard harmonics due to finite amplitude deformation and (i) the appearance of a subharmonic and superharmonics indicating nonlinear coupling in the system.

in the fluid by noting the pressure transmission ratio from the acoustic device to the fluid as $T = \frac{Z_L - Z_w}{Z_L + Z_w} = 0.15$, where $Z_L = 18.5 \times 10^6$ Pa-s/m^3 is the acoustic impedance of LN and $Z_w = 1.5 \times 10^6$ Pa-s/m^3 is the acoustic impedance of water.

The vibration response of the GVs due to the acoustic pressure produced by our transducer at 6.5 MHz is shown in Fig. 8.7. The vibration amplitude grows from 10 to nearly 100 nm, much larger than the 10–100 pm displacements observed at the GV and agglomerated GV linear resonance frequencies in Figs. 8.1 and 8.6, respectively. As the acoustic pressure is increased to between 89 and 132 kPa, the GVs' displacement amplitude grows from 5 to 10 nm (*see* the green area in Fig. 8.7) with displacement characteristic of large amplitude bubble oscillations in Fig. 8.7(d), a plot of the real-time response of the GVs. The physical response of a bubble is different in the compression and expansion phases, [274] leading to a periodic response with a change in slope as the bubble transitions between the two phases as observed in these GVs. It is worth noting here that the LDV provides information on the direction of deformation, with positive displacement here implying motion of the measured surface towards the substrate and away from the LDV system, towards collapse, while negative displacement values are away from the substrate and towards the LDV.

There is a significant increase in the displacement amplitude to around 40 nm as the acoustic pressure reaches 175 kPa (*see* the blue area in Fig. 8.7), with the GVs' time-based response exhibiting nearly limiting sawtooth oscillations in Fig. 8.7(e). This vibration amplitude remains constant with an increase in the acoustic pressure to just beyond 320 to 370 kPa, at which point the displacement doubles once again to just over 80 nm (*see*

the pink area in Fig. 8.7)—but only for one to a very few cycles of vibration. As shown in Fig. 8.7(f), the application of such high acoustic pressure causes large displacements, first towards collapse, then away from the substrate, again towards collapse at a lower amplitude, and finally followed by a much weaker vibration response from the GVs. This indicates irreversible buckling and collapse of the GVs. It is worth noting that the measured vibration amplitude of slightly more than 80 nm roughly corresponds to one-half the size of the GV itself: taking into account the wall thickness of the GV, this could reasonably represent the internal radius of the cavity driven to collapse from the buckling.

We calculated the radiated sound pressure of the GVs $P_{rad} = \rho_l(2R\dot{R}^2 + R^2\ddot{R})/d$ based on the LDV-measured real-time vibration amplitude data of the GVs, $R = R(t)$, where d is the distance of the measurement from the GVs.[265] The fast Fourier-transformed P_{rad} frequency spectra in Fig. 8.7(g-i) show that the number and intensity of peaks in the spectra grows with an increase in the excitation pressure. As the excitation pressure is increased from (Fig. 8.7(g)) 132 kPa to 178 and 330 kPa (Fig. 8.7(h,i), respectively), the appearance of harmonic responses in the emitted GVs' pressure indicates a transition to finite non-sinusoidal deformation of the GVs and participation of these higher frequency modes. The increase in both the number and amplitude of these harmonics with increasing excitation pressure is a strong indicator of building towards collapse of the GVs, as modal participation in an instantaneous change in displacement would extend to very high harmonics with linearly decreasing modal amplitudes. Furthermore, at 330 kPa (Fig. 8.7(i)), the appearance of resonances not associated with any of the standard linear responses of the system—a subharmonic response at 3.25 MHz and superharmonic responses at 9.65

and 21.8 MHz—indicate a nonlinear mechanism in the GV response and support the contention that the GVs are buckling and approaching collapse.

The 178 kPa produced from our transducer in our study is between the critical pressure required for buckling according to Cherin, *et al.*, [265] (92.4 kPa) and Lakshmanan, *et al.* [253] (200 kPa), while at higher amplitudes our transducer produces acoustic pressures sufficient to achieve the critical pressure estimates by Lakshmanan, *et al.* The difference between the buckling pressure threshold predicted in Lakshmanan's work and our experiments can be attributed to different buckling observation and pressure measuring methods. Lakshmanan, *et al.* represents the intensity of GVs' vibration with intensity measured in ultrasound scanning images while we performed direct observation of the displacement of the GVs in our study but must compute the resulting pressures. The limited observability of the true GV motion via our LDV may also be a factor in the relatively low prediction of the threshold pressure required to collapse the GVs in our measurements: only motion along the laser is measured via the LDV, though the GV motion is certainly more complex.

8.4 Conclusions

The ability to monitor sub-micrometer gas vesicles' (GVs) vibration behavior to nonlinear buckling and collapse using laser Doppler vibrometry is reported, providing a precise noncontact technique for monitoring the motion of sub-micrometer objects. The fundamental and first harmonic resonance frequencies of the vesicles are found to be 1.024 and 1.710 GHz, respectively. An interparticle resonance is furthermore identified at ∼300 MHz,

inversely dependent upon the agglomerated GV size of around 615 nm. Most importantly, the vesicles amplify and broaden input acoustic signals at far lower frequencies—for example, 7 MHz—associated with medical and industrial applications, and they are found to transition from a linear to nonlinear response at 150 kPa and to collapse at 350 kPa or greater.

Chapter 8 in full, is a reprint of material appears in Advanced Functional Materials 2020. Zhang, Shuai; Huang, An; Bar-Zion, Avinoam; Wang, Jiaying; Mena, Oscar; Shapiro, Mikhail; Friend, James., Advanced Functional Materials 2020. The dissertation author was the primary investigator and author of this paper.

Chapter 9

Summary and future work

Acoustofludics is a phenomenon that describes fluid manipulation in micro or nano-scaled under the acoustic wave. Compare to other external excitation forces to trigger the fluid motions, surface acoustic wave (SAW) stands out due to its small size, power density, customized designs capability, and efficiency. Uniquely, SAW generate extreme local acceleration, driving acoustic streaming-driven fluid flow up to 1 m/s, and imparting acoustic forces upon objects present in the fluid down to the micro or nano sized scales.

In this dissertation, three applications was achieved due to SAW is used in the system. The first one is enhancing the Li ion diffusion rate to achieve a dense Li deposition for a Li metal battery, and similar to achieve a high power density and high energy density Li ion battery. The second approach is to adopt SAW device with external magnetic forces to trigger the 0-D magnetic particles to 2-D magnetic films formation. Finally, adopting an acoustic device to observe resonance frequency responses and non-linear buckling behaviors of the submicron-sized gas vesicles is been shown.

Chapter 4 devised a chemistry-agnostic means for avoiding ion depletion and dendrite growth in liquid electrolyte batteries. Adopting small, high-frequency ultrasound generators to drive electrolyte flow within the inter-electrode gaps gives rise to ion flux distributions that render potential locations of dendrite growth stable within a specific distance from the ultrasound source. This distance is independent of the details of the flow as long as the Peclet number is sufficiently large. This is fortunately possible with the acoustic streaming induced by our ultrasound devices and make practical Li metal rechargeable batteries possible, even with rapid charge rates and the choice of electrode materials and electrolytes that would normally be considered unrealistic. The Li‖Cu configuration, as an example, was able to cycle until 6 mA/cm^2 current density with reasonable Coulombic efficiencies above 80% throughout. Moreover, the Li‖$LiFePO_4$ configuration can deliver 95 mAh/g capacity after 200 cycles at 2C charge and discharge rates. Dense plating of Li in both cell types was shown with SAW, and compared to the significant porosity and dendrites present in otherwise identical cells without SAW.

Chapter5 introduced integrating a SAW device into a multilayer LIB to enhance the Li ion diffusivity of a LIB. The ion flux generating from the SAW device enhancing the diffusion rate of the cations and therefore enhance both energy density and power density. It is shown that a SAW LIB pouch cell is able to cycle to at least 5C charge rate, while achieving at least doubled energy density compare to the no SAW cell. Moreover, it is shown that the SAW LIB achieves long term cycle ability to at least 2000 cycles while maintains 80% of the energy density. It is also shown that the SEI layer is thinner with the SAW device according to the EDX results. Moreover, there's no lithium dendrites on

the anode from a SAW LIB, indicating good Li intercalation during fast charging. This correlates with the results from XRD, where limited peak shifting is happened in the SAW LIB compare to a no SAW cell. Finally, the neutron diffraction analysis indicates that less Li loss after the cycling due to the existence of a SAW device. It is anticipate that a remarkable freedom in the choice of battery electrochemistry and operation to be facilitated from this simple technology, enabling greater efficiency, utility, and sustainability of rechargeable batteries for a broad swath of current and future applications.

Chapter 6 provided a promised solution to not only enable the cycling of a SAW integrate Li batteries but also enable a "true" acoustofludics powered lab-on-chip device. SAW devices, providing rapid fluid and suspended object transport. Acoustofluidic lab-on-chip devices offer a vast range of benefits from the energy storage and conversion field to noninsavie drug delivery. However, their potential has long been undermined by the need for benchtop or rack-mount electronics. The piezoelectric ultrasonic transducers within require these equipment and thus acoustofluidic device implementation in a bedside setting has been limited. A detailed circuit designs to enable the microcircuits to drive 1–300 MHz acoustic devices was proposed and tested. Furthermore, the automated resonance finding and tracking, sensing and feedback, and built-in adjustability to accommodate devices' vastly different operating frequencies and powers in a single driver, including examples of fluid and particle manipulation typical of the needs in the acoustofludics discipline was discussed. Finally, we compare the performance of the circuit with the benchtop equipment with common acoustofludics phenomenon to verify the functionality of the PCB boards.

Chapter 7 presented a rapid and affordable technique to trigger rigid 2-D self-assembled

films of magnetite (Fe3O4) NP. We have experimentally demonstrated that the round-like 2-D magnetite films formed with sufficient surface acoustic wave power and external magnetic force. A rapid dimensional transition happens, from 1-D chain to 2-D film of Fe3O4 NP, through external magnetic force (0.25- 0.4 T) and surface acoustic wave (up to 115 mW). The scaling theory coupled with the experimental results was conducted to analyze the forces associated with the system to understand the mechanism of chain or film assembly processes. It is shown that the brownian force dominate at the 0-D particles region, while magnetic force dominate the 1-D chain region and the Bjerknes force take over the magnetic force and dominate at the 2-D film region. Chapter8 shows the ability to monitor sub-micrometer gas vesicles' (GVs) vibration behavior to nonlinear buckling and collapse using laser Doppler vibrometry is reported, providing a precise noncontact technique for monitoring the motion of sub-micrometer objects. The fundamental and first harmonic resonance frequencies of the vesicles are found to be 1.024 and 1.710 GHz, respectively. An interparticle resonance is furthermore identified at ∼300 MHz, inversely dependent upon the agglomerated GV size of around 615 nm. Most importantly, the vesicles amplify and broaden input acoustic signals at far lower frequencies—for example, 7 MHz—associated with medical and industrial applications, and they are found to transition from a linear to nonlinear response at 150 kPa and to collapse at 350 kPa or greater.

Given the abovementioned work, there is definitely a need to keep exploring the applications in the acoustofludics discipline. The integration of acoustic device in a battery shows promising results, from improving the deposition morphology, energy density, power density, cycle life, to the enhanced safety of a Li battery. It is important to derive out

a mathematical model to understand the how the cation concentration gradient change over the time and the length of the batteries during the acoustic streaming and the electrochmemistry process. Furthermore, this model can be further refined into a prediction model to describe the influence of an acoustic device to a battery. Moreover, the effect of the high frequency sound wave to the micro and nano-scale particles from the electrodes is another topic to study. This together with the previous mathematical model can have a insight to understand the acoustic streaming effect to a battery. On the other hand, Li is not only the battery chemistry that suffers from heterogeneous Li deposition and slow cation diffusion rate issues. Other battery chemistries, such as Zinc, has similar issues. It is interesting to see how the acoustic wave can affect the other ions deposition to the other electrochemistry system to broaden the benefit of from this efforts. Finally, the fluid transportation in the porous media and is accelerated by a SAW device is a new approach. This is a new direction to the paper-based microfludics devices as with a SAW device, it may enhance the fluid and particle transportation rate and improve the detection sensitivity.

Bibliography

[1] Haiyan Li, James R Friend, and Leslie Y Yeo. Surface acoustic wave concentration of particle and bioparticle suspensions. *Biomedical Microdevices*, 9(5):647–656, 2007.

[2] Ghulam Destgeer, Byunghang Ha, Jinsoo Park, and Hyung Jin Sung. Lamb wave-based acoustic radiation force-driven particle ring formation inside a sessile droplet. *Analytical chemistry*, 88(7):3976–3981, 2016.

[3] Priscilla R Rogers, James R Friend, and Leslie Y Yeo. Exploitation of surface acoustic waves to drive size-dependent microparticle concentration within a droplet. *Lab on a Chip*, 10(21):2979–2985, 2010.

[4] Weiwei Cui, Hao Zhang, Hongxiang Zhang, Yang Yang, Meihang He, Hemi Qu, Wei Pang, Daihua Zhang, and Xuexin Duan. Localized ultrahigh frequency acoustic fields induced micro-vortices for submilliseconds microfluidic mixing. *Applied Physics Letters*, 109(25):253503, 2016.

[5] Atetegeb Meazah Haregewoin, Aselefech Sorsa Wotango, and Bing-Joe Hwang. Electrolyte additives for lithium ion battery electrodes: progress and perspectives. *Energy & Environmental Science*, 9(6):1955–1988, 2016.

[6] Thi Thu Dieu Nguyen, Sara Abada, Amandine Lecocq, Julien Bernard, Martin Petit, Guy Marlair, Sylvie Grugeon, and Stéphane Laruelle. Understanding the thermal runaway of ni-rich lithium-ion batteries. *World Electric Vehicle Journal*, 10(4):79, 2019.

[7] Mukul D Tikekar, Snehashis Choudhury, Zhengyuan Tu, and Lynden A Archer. Design principles for electrolytes and interfaces for stable lithium-metal batteries. *Nature Energy*, 1(9):1–7, 2016.

[8] Thomas Waldmann, Björn-Ingo Hogg, Michael Kasper, Sébastien Grolleau, César Gutiérrez Couceiro, Khiem Trad, Bramy Pilipili Matadi, and Margret Wohlfahrt-Mehrens. Interplay of operational parameters on lithium deposition in lithium-ion cells: systematic measurements with reconstructed 3-electrode pouch full cells. *Journal of The Electrochemical Society*, 163(7):A1232, 2016.

[9] Jiantie Xu, Shixue Dou, Huakun Liu, and Liming Dai. Cathode materials for next generation lithium ion batteries. *Nano Energy*, 2(4):439–442, 2013.

[10] Press release: The nobel prize in chemistry 2019.

[11] Greenhouse gases equivalencies calculator - calculations and references, 2019.

[12] Carbon dioxide emissions from energy consumption in the transportation sector in the u.s. from 1975 to 2019, 2020.

[13] Gasoline is the main u.s. transportation fuel, 2020.

[14] JC Burns, DA Stevens, and JR Dahn. In-situ detection of lithium plating using high precision coulometry. *Journal of the Electrochemical Society*, 162(6):A959, 2015.

[15] James Friend and Leslie Y Yeo. Microscale acoustofluidics: Microfluidics driven via acoustics and ultrasonics. *Reviews of Modern Physics*, 83(2):647, 2011.

[16] James Friend and Leslie Y Yeo. Microscale acoustofluidics: Microfluidics driven via acoustics and ultrasonics. *Reviews of Modern Physics*, 83(2):647, 2011.

[17] Nam-Trung Nguyen, Steven T Wereley, and Seyed Ali Mousavi Shaegh. *Fundamentals and applications of microfluidics*. Artech house, 2019.

[18] Xiaoyun Ding, Peng Li, Sz-Chin Steven Lin, Zackary S Stratton, Nitesh Nama, Feng Guo, Daniel Slotcavage, Xiaole Mao, Jinjie Shi, Francesco Costanzo, and Tony Huang. Surface acoustic wave microfluidics. *Lab on a Chip*, 13(18):3626–3649, 2013.

[19] George M Whitesides. The origins and the future of microfluidics. *Nature*, 442(7101):368–373, 2006.

[20] Jun Zhang, Sheng Yan, Dan Yuan, Gursel Alici, Nam-Trung Nguyen, Majid Ebrahimi Warkiani, and Weihua Li. Fundamentals and applications of inertial microfluidics: a review. *Lab on a Chip*, 16(1):10–34, 2016.

[21] Adolf Fick. Ueber diffusion. *Annalen der Physik*, 170(1):59–86, 1855.

[22] Xin Liu, Sondre K Schnell, Jean-Marc Simon, Dick Bedeaux, Signe Kjelstrup, André Bardow, and Thijs JH Vlugt. Fick diffusion coefficients of liquid mixtures directly obtained from equilibrium molecular dynamics. *The Journal of Physical Chemistry B*, 115(44):12921–12929, 2011.

[23] Na-Rae Kim and Chan-Byoung Chae. Novel modulation techniques using isomers as messenger molecules for nano communication networks via diffusion. *IEEE Journal on Selected Areas in Communications*, 31(12):847–856, 2013.

[24] Chia-Yen Lee, Wen-Teng Wang, Chan-Chiung Liu, and Lung-Ming Fu. Passive mixers in microfluidic systems: A review. *Chemical Engineering Journal*, 288:146–160, 2016.

[25] Liang-Hsuan Lu, Kee Suk Ryu, and Chang Liu. A magnetic microstirrer and array for microfluidic mixing. *Journal of microelectromechanical systems*, 11(5):462–469, 2002.

[26] Wenming Li, Xiaopeng Qu, Tamanna Alam, Fanghao Yang, Wei Chang, Jamil Khan, and Chen Li. Enhanced flow boiling in microchannels through integrating multiple micro-nozzles and reentry microcavities. *Applied Physics Letters*, 110(1):014104, 2017.

[27] Leslie Y Yeo and James R Friend. Ultrafast microfluidics using surface acoustic waves. *Biomicrofluidics*, 3(1):012002, 2009.

[28] Peiran Zhang, Hunter Bachman, Adem Ozcelik, and Tony Jun Huang. Acoustic microfluidics. *Annual Review of Analytical Chemistry*, 13:17–43, 2020.

[29] Zhen Yang, Hiroshi Goto, Mikio Matsumoto, and Ryutaro Maeda. Active micromixer for microfluidic systems using lead-zirconate-titanate (pzt)-generated ultrasonic vibration. *ELECTROPHORESIS: An International Journal*, 21(1):116–119, 2000.

[30] Zhen Yang, Sohei Matsumoto, Hiroshi Goto, Mikio Matsumoto, and Ryutaro Maeda. Ultrasonic micromixer for microfluidic systems. *Sensors and Actuators A: Physical*, 93(3):266–272, 2001.

[31] PK Panda and B Sahoo. Pzt to lead free piezo ceramics: a review. *Ferroelectrics*, 474(1):128–143, 2015.

[32] Iñigo Bretos, Ricardo Jiménez, Javier Garcïa-López, Lorena Pardo, and M Lourdes Calzada. Photochemical solution deposition of lead-based ferroelectric films: avoiding the pbo-excess addition at last. *Chemistry of Materials*, 20(18):5731–5733, 2008.

[33] Ting Zheng, Yang Zhang, Qingqing Ke, Haijun Wu, Liew Weng Heng, Dingquan Xiao, Jianguo Zhu, Stephen J Pennycook, Kui Yao, and Jiagang Wu. High-performance potassium sodium niobate piezoceramics for ultrasonic transducer. *Nano Energy*, 70:104559, 2020.

[34] Jie Xing, Laiming Jiang, Chunlin Zhao, Zhi Tan, Qian Xu, Jiagang Wu, Qiang Chen, Dingquan Xiao, and Jianguo Zhu. Potassium sodium niobate based lead-free ceramic for high-frequency ultrasound transducer applications. *Journal of Materiomics*, 2020.

[35] RM White and FW Voltmer. Direct piezoelectric coupling to surface elastic waves. *Applied Pphysics Letters*, 7(12):314–316, 1965.

[36] Julius Koskela, Jouni V Knuuttila, Tapani Makkonen, Victor P Plessky, and Martti M Salomaa. Acoustic loss mechanisms in leaky saw resonators on lithium tantalate. *ieee transactions on ultrasonics, ferroelectrics, and frequency control*, 48(6):1517–1526, 2001.

[37] Thomas W Grudkowski, Gary K Montress, Meyer Gilden, and James F Black. Integrated circuit compatible surface acoustic wave devices on gallium arsenide. *IEEE Transactions on Microwave Theory and Techniques*, 29(12):1348–1356, 1981.

[38] Henry A Wilson and Russell W Frazier. Crystal cutting saw, April 22 1958. US Patent 2,831,476.

[39] S Bensmaine, L Le Brizoual, O Elmazria, JJ Fundenberger, M Belmahi, and B Benyoucef. Saw devices based on zno inclined c-axis on diamond. *Diamond and related materials*, 17(7-10):1420–1423, 2008.

[40] RW Whatmore, NM Shorrocks, C O'hara, FW Ainger, and IM Young. Lithium tetraborate: a new temperature-compensated saw substrate material. *Electronics Letters*, 17(1):11–12, 1981.

[41] Clemens CW Ruppel, Roland Dill, Alice Fischerauer, Gerhard Fischerauer, Waldemar Gawlik, Jürgen Machui, Folkhard Muller, Leonhard Reindl, Werner Ruile, Gerd Scholl, Isidor Schropp, and Wagner Karl. Saw devices for consumer communication applications. *IEEE transactions on ultrasonics, ferroelectrics, and frequency control*, 40(5):438–452, 1993.

[42] A Takayanagi, K Yamanouchi, and K Shibayama. Piezoelectric leaky surface wave in linbo3. *Applied Physics Letters*, 17(5):225–227, 1970.

[43] AJ Slobodnik and ED Conway. New high-frequency high-coupling low-beam-steering cut for acoustic surface waves on linbo3. *Electronics Letters*, 6(6):171–173, 1970.

[44] Leslie Y Yeo and James R Friend. Surface acoustic wave microfluidics. *Annual review of fluid mechanics*, 46:379–406, 2014.

[45] KIMIO Shibayama, KAZUHIKO Yamanouchi, HIROAKI Sato, and TOSHIYASU Meguro. Optimum cut for rotated y-cut linbo 3 crystal used as the substrate of acoustic-surface-wave filters. *Proceedings of the IEEE*, 64(5):595–597, 1976.

[46] Colin K Campbell. Applications of surface acoustic and shallow bulk acoustic wave devices. *Proceedings of the IEEE*, 77(10):1453–1484, 1989.

[47] Fred S Hickernell. -3-surface acoustic wave technology macrosuccess through microseisms. In *Physical Acoustics*, volume 24, pages 135–207. Elsevier, 1999.

[48] Goksen G Yaralioglu, Arif Sanli Ergun, Baris Bayram, Edward Haeggstrom, and Butrus T Khuri-Yakub. Calculation and measurement of electromechanical coupling coefficient of capacitive micromachined ultrasonic transducers. *IEEE transactions on ultrasonics, ferroelectrics, and frequency control*, 50(4):449–456, 2003.

[49] Masakazu Mimura, Daisuke Ajima, and Chihiro Konoma. Sh-type spurious response free tc-saw resonators using low acoustic velocity rayleigh saw on linbo 3 substrate. In *2018 IEEE International Ultrasonics Symposium (IUS)*, pages 1–9. IEEE, 2018.

[50] Colin Campbell. *Surface Acoustic Wave Devices for Mobile and Wireless Communications*. Academic Press, Inc., 1998.

[51] William Connacher, Naiqing Zhang, An Huang, Jiyang Mei, Shuai Zhang, Tilvawala Gopesh, and James Friend. Micro/nano acoustofluidics: materials, phenomena, design, devices, and applications. *Lab on a Chip*, 18(14):1952–1996, 2018.

[52] Michael B Dentry, Leslie Y Yeo, and James R Friend. Frequency effects on the scale and behavior of acoustic streaming. *Physical Review E*, 89(1):013203, 2014.

[53] Martin Wiklund, Roy Green, and Mathias Ohlin. Acoustofluidics 14: Applications of acoustic streaming in microfluidic devices. *Lab on a Chip*, 12(14):2438–2451, 2012.

[54] Graham Woan. *The Cambridge handbook of physics formulas*. Cambridge University Press, 2000.

[55] Hank Wohltjen. Mechanism of operation and design considerations for surface acoustic wave device vapour sensors. *Sensors and Actuators*, 5(4):307–325, 1984.

[56] Yongbeom Lee and Keekeun Lee. Effective light beam modulation by chirp idt on a suspended linbo3 membrane for 3d holographic displays. *Sensors*, 20(4):1218, 2020.

[57] XY Du, ME Swanwick, Yong Qing Fu, JK Luo, AJ Flewitt, Dae-Sik Lee, Sunglyul Maeng, and WI Milne. Surface acoustic wave induced streaming and pumping in 128 y-cut linbo3 for microfluidic applications. *Journal of Micromechanics and Microengineering*, 19(3):035016, 2009.

[58] Liqiang Ren, Shujie Yang, Peiran Zhang, Zhiguo Qu, Zhangming Mao, Po-Hsun Huang, Yuchao Chen, Mengxi Wu, Lin Wang, Peng Li, and Tony Huang. Standing surface acoustic wave (ssaw)-based fluorescence-activated cell sorter. *Small*, 14(40):1801996, 2018.

[59] RM Arzt, E Salzmann, and K Dransfeld. Elastic surface waves in quartz at 316 mhz. *Applied Physics Letters*, 10(5):165–167, 1967.

[60] James Lighthill. Acoustic streaming. *Journal of sound and vibration*, 61(3):391–418, 1978.

[61] Michael Baudoin, Philippe Brunet, Olivier Bou Matar, and Etienne Herth. Low power sessile droplets actuation via modulated surface acoustic waves. *Applied Physics Letters*, 100(15):154102, 2012.

[62] A Bussonnière, Michael Baudoin, Philippe Brunet, and O Bou Matar. Dynamics of sessile and pendant drops excited by surface acoustic waves: Gravity effects and correlation between oscillatory and translational motions. *Physical Review E*, 93(5):053106, 2016.

[63] Sean Collignon, James Friend, and Leslie Yeo. Planar microfluidic drop splitting and merging. *Lab on a Chip*, 15(8):1942–1951, 2015.

[64] Aisha Qi, James R Friend, Leslie Y Yeo, David AV Morton, Michelle P McIntosh, and Leone Spiccia. Miniature inhalation therapy platform using surface acoustic wave microfluidic atomization. *Lab on a Chip*, 9(15):2184–2193, 2009.

[65] Ming K Tan, James R Friend, and Leslie Y Yeo. Interfacial jetting phenomena induced by focused surface vibrations. *Physical Review Letters*, 103(2):024501, 2009.

[66] Louis Vessot King. On the acoustic radiation pressure on spheres. *Proceedings of the Royal Society of London. Series A-Mathematical and Physical Sciences*, 147(861):212–240, 1934.

[67] Ming K Tan, Leslie Y Yeo, and James R Friend. Unique flow transitions and particle collection switching phenomena in a microchannel induced by surface acoustic waves. *Applied Physics Letters*, 97(23):234106, 2010.

[68] David J Collins, Zhichao Ma, Jongyoon Han, and Ye Ai. Continuous micro-vortex-based nanoparticle manipulation via focused surface acoustic waves. *Lab on a Chip*, 17(1):91–103, 2017.

[69] Morteza Miansari and James R Friend. Acoustic nanofluidics via room-temperature lithium niobate bonding: A platform for actuation and manipulation of nanoconfined fluids and particles. *Advanced Functional Materials*, 26(43):7861–7872, 2016.

[70] Junbo Hou, Yuyan Shao, Michael W Ellis, Robert B Moore, and Baolian Yi. Graphene-based electrochemical energy conversion and storage: fuel cells, supercapacitors and lithium ion batteries. *Physical Chemistry Chemical Physics*, 13(34):15384–15402, 2011.

[71] Haryo S Oktaviano, Koichi Yamada, and Keiko Waki. Nano-drilled multiwalled carbon nanotubes: characterizations and application for lib anode materials. *Journal of Materials Chemistry*, 22(48):25167–25173, 2012.

[72] Brian J Landi, Matthew J Ganter, Cory D Cress, Roberta A DiLeo, and Ryne P Raffaelle. Carbon nanotubes for lithium ion batteries. *Energy & Environmental Science*, 2(6):638–654, 2009.

[73] Jun Liu, Zhenan Bao, Yi Cui, Eric J Dufek, John B Goodenough, Peter Khalifah, Qiuyan Li, Bor Yann Liaw, Ping Liu, and Arumugam Manthiram. Pathways for practical high-energy long-cycling lithium metal batteries. *Nature Energy*, 4:180–186, 2019.

[74] Michael J Zachman, Zhengyuan Tu, Snehashis Choudhury, Lynden A Archer, and Lena F Kourkoutis. Cryo-STEM mapping of solid–liquid interfaces and dendrites in lithium-metal batteries. *Nature*, 560(7718):345–349, 2018.

[75] Paul Albertus, Susan Babinec, Scott Litzelman, and Aron Newman. Status and challenges in enabling the lithium metal electrode for high-energy and low-cost rechargeable batteries. *Nature Energy*, 3(1):16–21, 2018.

[76] J.M. Tarascon and Michel Armand. Issues and challenges facing rechargeable lithium batteries. *Nature*, 414(6861):359–367, 2001.

[77] Dingchang Lin, Yayuan Liu, and Yi Cui. Reviving the lithium metal anode for high-energy batteries. *Nature Nanotechnology*, 12(3):194–206, 2017.

[78] D Aurbach, E Zinigrad, H Teller, and P Dan. Factors which limit the cycle life of rechargeable lithium (metal) batteries. *Journal of the Electrochemical Society*, 147(4):1274–1279, 2000.

[79] Richard Schmuch, Ralf Wagner, Gerhard Hörpel, Tobias Placke, and Martin Winter. Performance and cost of materials for lithium-based rechargeable automotive batteries. *Nature Energy*, 3(4):267–278, 2018.

[80] J-N Chazalviel. Electrochemical aspects of the generation of ramified metallic electrodeposits. *Physical Review A*, 42(12):7355–7367, 1990.

[81] Xue Qiang Zhang, Xin Bing Cheng, Xiang Chen, Chong Yan, and Qiang Zhang. Fluoroethylene carbonate additives to render uniform li deposits in lithium metal batteries. *Advanced Functional Materials*, 27(10):1605989, 2017.

[82] David Rehnlund, Charlotte Ihrfors, Julia Maibach, and Leif Nyholm. Dendrite-free lithium electrode cycling via controlled nucleation in low $lipf_6$ concentration electrolytes. *Materials Today*, 21(10):1010–1018, 2018.

[83] JC Burns, R Petibon, KJ Nelson, NN Sinha, Adil Kassam, BM Way, and JR Dahn. Studies of the effect of varying vinylene carbonate (vc) content in lithium ion cells on cycling performance and cell impedance. *Journal of the Electrochemical Society*, 160(10):A1668–A1674, 2013.

[84] Chong Yan, Xin-Bing Cheng, Yang Tian, Xiang Chen, Xue-Qiang Zhang, Wen-Jun Li, Jia-Qi Huang, and Qiang Zhang. Dual-layered film protected lithium metal anode to enable dendrite-free lithium deposition. *Advanced Materials*, 30(25):1707629, 2018.

[85] Shuru Chen, Jianming Zheng, Donghai Mei, Kee Sung Han, Mark H Engelhard, Wengao Zhao, Wu Xu, Jun Liu, and Ji-Guang Zhang. High-voltage lithium-metal batteries enabled by localized high-concentration electrolytes. *Advanced Materials*, 30(21):1706102, 2018.

[86] Fei Ding, Wu Xu, Gordon L Graff, Jian Zhang, Maria L Sushko, Xilin Chen, Yuyan Shao, Mark H Engelhard, Zimin Nie, and Jie Xiao. Dendrite-free lithium deposition via self-healing electrostatic shield mechanism. *Journal of the American Chemical Society*, 135(11):4450–4456, 2013.

[87] Haodong Liu, Hongyao Zhou, Byoung-Sun Lee, Xing Xing, Matthew Gonzalez, and Ping Liu. Suppressing lithium dendrite growth with a single-component coating. *ACS Applied Materials & Interfaces*, 9(36):30635–30642, 2017.

[88] Haodong Liu, Xuefeng Wang, Hongyao Zhou, Hee-Dae Lim, Xing Xing, Qizhang Yan, Ying Shirley Meng, and Ping Liu. Structure and solution dynamics of lithium methyl carbonate as a protective layer for lithium metal. *ACS Applied Energy Materials*, 1(5):1864–1869, 2018.

[89] Yayuan Liu, Dingchang Lin, Zheng Liang, Jie Zhao, Kai Yan, and Yi Cui. Lithium-coated polymeric matrix as a minimum volume-change and dendrite-free lithium metal anode. *Nature Communications*, 7:10992, 2016.

[90] Haodong Liu, Xiujun Yue, Xing Xing, Qizhang Yan, Jason Huang, Victoria Petrova, Hongyao Zhou, and Ping Liu. A scalable 3d lithium metal anode. *Energy Storage Materials*, 16:505–511, 2019.

[91] Chun-Peng Yang, Ya-Xia Yin, Shuai-Feng Zhang, Nian-Wu Li, and Yu-Guo Guo. Accommodating lithium into 3d current collectors with a submicron skeleton towards long-life lithium metal anodes. *Nature communications*, 6:8058, 2015.

[92] Ziyang Lu, Qinghua Liang, Bo Wang, Ying Tao, Yufeng Zhao, Wei Lv, Donghai Liu, Chen Zhang, Zhe Weng, Jiachen Liang, Huan Li, and Quan-Hong Yang. Graphitic carbon nitride induced micro-electric field for dendrite-free lithium metal anodes. *Advanced Energy Materials*, 9(7):1803186, 2019.

[93] Doron Aurbach, Ella Zinigrad, Yaron Cohen, and Hanan Teller. A short review of failure mechanisms of lithium metal and lithiated graphite anodes in liquid electrolyte solutions. *Solid state ionics*, 148(3-4):405–416, 2002.

[94] M Rosso, J-N Chazalviel, and E Chassaing. Calculation of the space charge in electrodeposition from a binary electrolyte. *Journal of Electroanalytical Chemistry*, 587(2):323–328, 2006.

[95] Thomas Waldmann, Michael Kasper, and Margret Wohlfahrt-Mehrens. Optimization of charging strategy by prevention of lithium deposition on anodes in high-energy

lithium-ion batteries–electrochemical experiments. *Electrochimica Acta*, 178:525–532, 2015.

[96] Marc Doyle, Thomas F Fuller, and John Newman. The importance of the lithium ion transference number in lithium/polymer cells. *Electrochimica Acta*, 39(13):2073–2081, 1994.

[97] Kevin G Gallagher, Stephen E Trask, Christoph Bauer, Thomas Woehrle, Simon F Lux, Matthias Tschech, Peter Lamp, Bryant J Polzin, Seungbum Ha, Brandon Long, Qungliu Wu, Wenquan Lu, Dennis Dees, and Andrew Jansen. Optimizing areal capacities through understanding the limitations of lithium-ion electrodes. *Journal of The Electrochemical Society*, 163(2):A138, 2015.

[98] Andrew M Colclasure, Tanvir R Tanim, Andrew N Jansen, Stephen E Trask, Alison R Dunlop, Bryant J Polzin, Ira Bloom, Dave Robertson, LeRoy Flores, Michael Evans, Eric Dufek, and Kandler Smith. Electrode scale and electrolyte transport effects on extreme fast charging of lithium-ion cells. *Electrochimica Acta*, 337:135854, 2020.

[99] Xianhui Zhang, Lianfeng Zou, Yaobin Xu, Xia Cao, Mark H Engelhard, Bethany E Matthews, Lirong Zhong, Haiping Wu, Hao Jia, Xiaodi Ren, Peiyuan Gao, Zonghai Chen, Yan Qin, Christopher Kompella, Bruce Arey, Jun Li, Deyu Want, Chongmin Wang, Ji-Guang Zhang, and Wu Xu. Advanced electrolytes for fast-charging high-voltage lithium-ion batteries in wide-temperature range. *Advanced Energy Materials*, page 2000368, 2020.

[100] ER Logan and JR Dahn. Electrolyte design for fast-charging li-ion batteries. *Trends in Chemistry*, 2020.

[101] R Petibon, J Harlow, DB Le, and JR Dahn. The use of ethyl acetate and methyl propanoate in combination with vinylene carbonate as ethylene carbonate-free solvent blends for electrolytes in li-ion batteries. *Electrochimica Acta*, 154:227–234, 2015.

[102] Xianyang Wu, Tianyi Liu, Yaocai Bai, Xu Feng, Muhammad Mominur Rahman, Cheng-Jun Sun, Feng Lin, Kejie Zhao, and Zhijia Du. Effects of solvent formulations in electrolytes on fast charging of li-ion cells. *Electrochimica Acta*, page 136453, 2020.

[103] Ilya A Shkrob, James F Wishart, and Daniel P Abraham. What makes fluoroethylene carbonate different. *The Journal of Physical Chemistry C*, 119(27):14954–14964, 2015.

[104] Anna Lee, Márton Vörös, Wesley M Dose, Jens Niklas, Oleg Poluektov, Richard D Schaller, Hakim Iddir, Victor A Maroni, Eungje Lee, Brian Ingram, Larry Curtiss, and Christopher Johnson. Photo-accelerated fast charging of lithium-ion batteries. *Nature communications*, 10(1):1–7, 2019.

[105] Shizhi Qian and Haim H. Bau. Magneto-hydrodynamics based microfluidics. *Mechanics Research Communications*, 36(1):10–21, 2009.

[106] T Nagaura. Lithium ion rechargeable battery. *Progress in Batteries & Solar Cells*, 9:209, 1990.

[107] J-M Tarascon and Michel Armand. Issues and challenges facing rechargeable lithium batteries. In *Materials for sustainable energy: a collection of peer-reviewed research and review articles from Nature Publishing Group*, pages 171–179. World Scientific, 2011.

[108] Naoki Nitta, Feixiang Wu, Jung Tae Lee, and Gleb Yushin. Li-ion battery materials: present and future. *Materials today*, 18(5):252–264, 2015.

[109] Johannes Betz, Georg Bieker, Paul Meister, Tobias Placke, Martin Winter, and Richard Schmuch. Theoretical versus practical energy: a plea for more transparency in the energy calculation of different rechargeable battery systems. *Advanced Energy Materials*, 9(6):1803170, 2019.

[110] Guangyuan Wesley Zheng and Tang Wei. Batteries: Just a spoonful of $lipf_6$. *Nature Energy*, 2(3):17029, 2017.

[111] Subrahmanyam Goriparti, Ermanno Miele, Francesco De Angelis, Enzo Di Fabrizio, Remo Proietti Zaccaria, and Claudio Capiglia. Review on recent progress of nanostructured anode materials for li-ion batteries. *Journal of power sources*, 257:421–443, 2014.

[112] Xin Bing Cheng, Rui Zhang, Chen Zi Zhao, and Qiang Zhang. Toward safe lithium metal anode in rechargeable batteries: a review. *Chemical Reviews*, 117(15):10403–10473, 2017.

[113] Kang Shen, Zeng Wang, Xuanxuan Bi, Yao Ying, Duo Zhang, Chengbin Jin, Guangya Hou, Huazhen Cao, Liankui Wu, Guoqu Zheng, Yiping Tang, Xinyong Tao, and Jun Lu. Magnetic field–suppressed lithium dendrite growth for stable lithium-metal batteries. *Advanced Energy Materials*, page 1900260, 2019.

[114] H.C. Lai. Method for using ultrasound for assisting forming conductive layers on semiconductor devices, Dec. 2000. US Patent 6,159,853.

[115] High-density and high-precision printed circuit board copper electroplating process, May 21 2014. CN Patent App. CN 201,210,444,599.

[116] Richard Shilton, Ming K Tan, Leslie Y Yeo, and James R Friend. Particle concentration and mixing in microdrops driven by focused surface acoustic waves. *Journal of Applied Physics*, 104(1):014910, 2008.

[117] An Huang, Morteza Miansari, and James Friend. Driving useful morphological changes in magnetic nanoparticle structures through the application of acoustic waves and magnetic fields. *Applied Physics Letters*, 113(3):034103, 2018.

[118] Jianming Zheng, Mark H Engelhard, Donghai Mei, Shuhong Jiao, Bryant J Polzin, Ji-Guang Zhang, and Wu Xu. Electrolyte additive enabled fast charging and stable cycling lithium metal batteries. *Nature Energy*, 2(3):17012, 2017.

[119] Yayuan Liu, Dingchang Lin, Zheng Liang, Jie Zhao, Kai Yan, and Yi Cui. Lithium-coated polymeric matrix as a minimum volume-change and dendrite-free lithium metal anode. *Nature communications*, 7:10992, 2016.

[120] Kai Yan, Zhenda Lu, Hyun-Wook Lee, Feng Xiong, Po-Chun Hsu, Yuzhang Li, Jie Zhao, Steven Chu, and Yi Cui. Selective deposition and stable encapsulation of lithium through heterogeneous seeded growth. *Nature Energy*, 1(3):16010, 2016.

[121] Xu Wang, Wei Zeng, Liang Hong, Wenwen Xu, Haokai Yang, Fan Wang, Huigao Duan, Ming Tang, and Hanqing Jiang. Stress-driven lithium dendrite growth mechanism and dendrite mitigation by electroplating on soft substrates. *Nature Energy*, 3(3):227, 2018.

[122] Chengcheng Fang, Xuefeng Wang, and Ying Shirley Meng. Key issues hindering a practical lithium-metal anode. *Trends in Chemistry*, 2019.

[123] Rohan Akolkar. Mathematical model of the dendritic growth during lithium electrodeposition. *Journal of Power Sources*, 232:23–28, 2013.

[124] Charles Monroe and John Newman. Dendrite growth in lithium/polymer systems a propagation model for liquid electrolytes under galvanostatic conditions. *Journal of the Electrochemical Society*, 150(10):A1377–A1384, 2003.

[125] Daniel M. Tartakovsky and Dongbin Xiu. Stochastic analysis of transport in tubes with rough walls. *Journal of Computational Physics*, 217(1):248–259, 2006.

[126] J Jorne, Y J Lii, and K E Yee. Suppression of dendrites and roughness during electrodeposition by impinging flow. *Journal of the Electrochemical Society*, 134(6):1399–1402, June 1987.

[127] Andreas Ehrl, Johannes Landesfeind, Wolfgang A Wall, and Hubert A Gasteiger. Determination of transport parameters in liquid binary lithium ion battery electrolytes i. diffusion coefficient. *Journal of The Electrochemical Society*, 164(4):A826–A836, 2017.

[128] Wendy Zhang, Howard A Stone, and JD Sherwood. Mass transfer at a microelectrode in channel flow. *The Journal of Physical Chemistry*, 100(22):9462–9464, 1996.

[129] Michael B. Dentry, Leslie Y. Yeo, and James R. Friend. Frequency effects on the scale and behavior of acoustic streaming. *Physical Review E*, 89:013203, 2014.

[130] Lars Ole Valoen and Jan N Reimers. Transport properties of lipf$_6$-based li-ion battery electrolytes. *Journal of the Electrochemical Society*, 152(5):A882, 2005.

[131] JW Diggle, AR Despic, and JO'M Bockris. The mechanism of the dendritic electrocrystallization of zinc. *Journal of the Electrochemical Society*, 116(11):1503–1514, 1969.

[132] Shabbir Ahmed, Ira Bloom, Andrew N Jansen, Tanvir Tanim, Eric J Dufek, Ahmad Pesaran, Andrew Burnham, Richard B Carlson, Fernando Dias, Keith Hardy, Matthew Keyser, Cory Kreuzer, Anthony Markel, Andrew Meintz, Christopher Michelbacher, Manish Mohanpurkar, Paul Nelson, David Robertson, Don Scoffield, Matthew Shirk, Ram Vijayagopal, and Zhang Jiucai. Enabling fast charging–a battery technology gap assessment. *Journal of Power Sources*, 367:250–262, 2017.

[133] Hasan Mehrjerdi and Reza Hemmati. Electric vehicle charging station with multilevel charging infrastructure and hybrid solar-battery-diesel generation incorporating comfort of drivers. *Journal of Energy Storage*, 26:100924, 2019.

[134] Jürgen Wenig, Mariya Sodenkamp, and Thorsten Staake. Battery versus infrastructure: Tradeoffs between battery capacity and charging infrastructure for plug-in hybrid electric vehicles. *Applied Energy*, 255:113787, 2019.

[135] AA Hakeem Akinlabi and Davut Solyali. Configuration, design, and optimization of air-cooled battery thermal management system for electric vehicles: A review. *Renewable and Sustainable Energy Reviews*, 125:109815, 2020.

[136] Yiran Zheng, Yu Shi, and Yunhui Huang. Optimisation with adiabatic interlayers for liquid-dominated cooling system on fast charging battery packs. *Applied Thermal Engineering*, 147:636–646, 2019.

[137] Yayuan Liu, Yangying Zhu, and Yi Cui. Challenges and opportunities towards fast-charging battery materials. *Nature Energy*, 4(7):540–550, 2019.

[138] Anna Tomaszewska, Zhengyu Chu, Xuning Feng, Simon O'Kane, Xinhua Liu, Jingyi Chen, Chenzhen Ji, Elizabeth Endler, Ruihe Li, Lishuo Liu, Yalun Li, Siqi Zheng, Sebastian Vetterlein, Ming Gao, Jiuyu Du, Michael Parkes, Minggao Ouyang, Monica Marinescu, Gregory Offer, and Billy Wu. Lithium-ion battery fast charging: a review. *ETransportation*, 1:100011, 2019.

[139] Dongping Lu, Yuyan Shao, Terence Lozano, Wendy D Bennett, Gordon L Graff, Bryant Polzin, Jiguang Zhang, Mark H Engelhard, Natalio T Saenz, Wesley A Henderson, Priyanka Bhattacharya, Jun Liu, and Jie Xiao. Failure mechanism for fast-charged lithium metal batteries with liquid electrolytes. *Advanced Energy Materials*, 5(3):1400993, 2015.

[140] Purim Ladpli, Fotis Kopsaftopoulos, and Fu-Kuo Chang. Estimating state of charge and health of lithium-ion batteries with guided waves using built-in piezoelectric sensors/actuators. *Journal of Power Sources*, 384:342–354, 2018.

[141] Lukas Gold, Tobias Bach, Wolfgang Virsik, Angelika Schmitt, Jana Müller, Torsten EM Staab, and Gerhard Sextl. Probing lithium-ion batteries' state-of-charge using ultrasonic transmission–concept and laboratory testing. *Journal of Power Sources*, 343:536–544, 2017.

[142] Clement Bommier, Wesley Chang, Yufang Lu, Justin Yeung, Greg Davies, Robert Mohr, Mateo Williams, and Daniel Steingart. In operando acoustic detection of lithium metal plating in commercial licoo2/graphite pouch cells. *Cell Reports Physical Science*, page 100035, 2020.

[143] An Huang, Haodong Liu, Ofer Manor, Ping Liu, and James Friend. Enabling rapid charging lithium metal batteries via surface acoustic wave-driven electrolyte flow. *Advanced Materials*, 32(14):1907516, 2020.

[144] Matthew B Pinson and Martin Z Bazant. Theory of sei formation in rechargeable batteries: capacity fade, accelerated aging and lifetime prediction. *Journal of the Electrochemical Society*, 160(2):A243, 2012.

[145] Alexander Missyul, Ivan Bolshakov, and Roman Shpanchenko. Xrd study of phase transformations in lithiated graphite anodes by rietveld method. *Powder Diffraction*, 32:S56, 2017.

[146] Hae-Kyung Jeong, Yun Pyo Lee, Rob JWE Lahaye, Min-Ho Park, Kay Hyeok An, Ick Jun Kim, Cheol-Woong Yang, Chong Yun Park, Rodney S Ruoff, and Young Hee Lee. Evidence of graphitic ab stacking order of graphite oxides. *Journal of the American Chemical Society*, 130(4):1362–1366, 2008.

[147] Achim Wixforth. Acoustically driven planar microfluidics. *Superlattices and Microstructures*, 33(5-6):389–396, 2003.

[148] Anushi Rajapaksa, Aisha Qi, Leslie Y Yeo, Ross Coppel, and James R Friend. Enabling practical surface acoustic wave nebulizer drug delivery via amplitude modulation. *Lab on a Chip*, 14(11):1858–1865, 2014.

[149] Hunter Bachman, Po-Hsun Huang, Shuaigeo Zhao, Shujie Yang, Peiran Zhang, Hai Fu, and Tony Huang. Acoustofluidic devices controlled by cell phones. *Lab on a Chip*, 18(3):433–441, 2018.

[150] Hunter Bachman, Hai Fu, Po-Hsun Huang, Zhenhua Tian, Jonah Embry-Seckler, Joseph Rufo, Zhemiao Xie, Jessica H Hartman, Shuaiguo Zhao, Shujie Yang, Joel Meyer, and Tony Huang. Open source acoustofluidics. *Lab on a Chip*, 19(14):2404–2414, 2019.

[151] James R. Friend and Leslie Y. Yeo. Microscale acoustofluidics: Microfluidics driven via acoustics and ultrasonics. *Reviews of Modern Physics*, 83:647–704, 2011.

[152] Haiyan Li, James Friend, Leslie Yeo, Ayan Dasvarma, and Kathy Traianedes. Effect of surface acoustic waves on the viability, proliferation and differentiation of primary osteoblast-like cells. *Biomicrofluidics*, 3(3):034102, 2009.

[153] Yuchao Chen, Sixing Li, Yeyi Gu, Peng Li, Xiaoyun Ding, Lin Wang, J Philip McCoy, Stewart J Levine, and Tony Jun Huang. Continuous enrichment of low-abundance cell samples using standing surface acoustic waves (ssaw). *Lab on a Chip*, 14(5):924–930, 2014.

[154] Michael N Topp. Ultrasonic atomization-a photographic study of the mechanism of disintegration. *Journal of Aerosol Science*, 4(1):17–25, 1973.

[155] Thomas Frommelt, Marcin Kostur, Melanie Wenzel-Schäfer, Peter Talkner, Peter Hänggi, and Achim Wixforth. Microfluidic mixing via acoustically driven chaotic advection. *Physical Review Letters*, 100(3):034502, 2008.

[156] K Sritharan, CJ Strobl, MF Schneider, Achim Wixforth, and Zeno von Guttenberg. Acoustic mixing at low reynold's numbers. *Applied Physics Letters*, 88(5):054102, 2006.

[157] Sascha Meyer dos Santos, Anita Zorn, Zeno Guttenberg, Bettina Picard-Willems, Christina Kläffling, Karen Nelson, Ute Klinkhardt, and Sebastian Harder. A novel μ-fluidic whole blood coagulation assay based on rayleigh surface-acoustic waves as a point-of-care method to detect anticoagulants. *Biomicrofluidics*, 7(5):056502, 2013.

[158] Liangfei Tian, Nicolas Martin, Philip G Bassindale, Avinash J Patil, Mei Li, Adrian Barnes, Bruce W Drinkwater, and Stephen Mann. Spontaneous assembly of chemically encoded two-dimensional coacervate droplet arrays by acoustic wave patterning. *Nature communications*, 7(1):1–10, 2016.

[159] Xiaoyun Ding, Sz-Chin Steven Lin, Brian Kiraly, Hongjun Yue, Sixing Li, I-Kao Chiang, Jinjie Shi, Stephen J Benkovic, and Tony Jun Huang. On-chip manipulation of single microparticles, cells, and organisms using surface acoustic waves. *Proceedings of the National Academy of Sciences*, 109(28):11105–11109, 2012.

[160] Mengxi Wu, Yingshi Ouyang, Zeyu Wang, Rui Zhang, Po-Hsun Huang, Chuyi Chen, Hui Li, Peng Li, David Quinn, Ming Dao, Subra Suresh, Yoel Sadovsky, and Tony Huang. Isolation of exosomes from whole blood by integrating acoustics and microfluidics. *Proceedings of the National Academy of Sciences*, 114(40):10584–10589, 2017.

[161] Anushi E Rajapaksa, Jenny J Ho, Aisha Qi, Rob Bischof, Tri-Hung Nguyen, Michelle Tate, David Piedrafita, Michelle P McIntosh, Leslie Y Yeo, Els Meeusen, Ross Coppel, and James Friend. Effective pulmonary delivery of an aerosolized plasmid dna vaccine via surface acoustic wave nebulization. *Respiratory Research*, 15(1):60, 2014.

[162] Christina Cortez-Jugo, Aisha Qi, Anushi Rajapaksa, James R Friend, and Leslie Y Yeo. Pulmonary monoclonal antibody delivery via a portable microfluidic nebulization platform. *Biomicrofluidics*, 9(5):052603, 2015.

[163] Anushi E Rajapaksa, Lien Anh Ha Do, Darren Suryawijaya Ong, Magdy Sourial, Duncan Veysey, Richard Beare, William Hughes, William Yang, Robert J Bischof, Amarin McDonnell, Peter Eu, Leslie Yeo, Paul Licciardi, and Edward Mulholland. Pulmonary deposition of radionucleotide-labeled palivizumab: Proof-of-concept study. *Frontiers in Pharmacology*, 11:1291, 2020.

[164] Adem Ozcelik, Joseph Rufo, Feng Guo, Yuyang Gu, Peng Li, James Lata, and Tony Jun Huang. Acoustic tweezers for the life sciences. *Nature Methods*, 15(12):1021–1028, 2018.

[165] Ghulam Destgeer and Hyung Jin Sung. Recent advances in microfluidic actuation and micro-object manipulation via surface acoustic waves. *Lab on a Chip*, 15(13):2722–2738, 2015.

[166] A Winkler, R Brünig, C Faust, R Weser, and H Schmidt. Towards efficient surface acoustic wave (saw)-based microfluidic actuators. *Sensors and Actuators A: Physical*, 247:259–268, 2016.

[167] Min Gon Kim, Sangpil Yoon, Hyung Ham Kim, and K Kirk Shung. Impedance matching network for high frequency ultrasonic transducer for cellular applications. *Ultrasonics*, 65:258–267, 2016.

[168] Vivek T Rathod. A review of electric impedance matching techniques for piezoelectric sensors, actuators and transducers. *Electronics*, 8(2):169, 2019.

[169] Mar Alvarez, James Friend, and Leslie Y Yeo. Rapid generation of protein aerosols and nanoparticles via surface acoustic wave atomization. *Nanotechnology*, 19(45):455103, 2008.

[170] Aisha Qi, Leslie Yeo, James Friend, and Jenny Ho. The extraction of liquid, protein molecules and yeast cells from paper through surface acoustic wave atomization. *Lab on a Chip*, 10(4):470–476, 2010.

[171] JC Waldrep and R Dhand. Advanced nebulizer designs employing vibrating mesh/aperture plate technologies for aerosol generation. *Current Drug Delivery*, 5(2):114–119, 2008.

[172] Kyung Hwa Chang, Sang-Hyub Moon, Jin Young Oh, Young-Soon Yoon, Namyi Gu, Chi-Yeon Lim, Bong Joo Park, and Ki Chang Nam. Comparison of salbutamol delivery efficiency for jet versus mesh nebulizer using mice. *Pharmaceutics*, 11(4):192, 2019.

[173] AV Aver'yanov, AG Konoplyannikov, NS Antonov, GL Osipova, OS Vasil'eva, MG Sakharova, AR Tatarskii, and VI Kobylyansky. Survival of mesenchymal stem cells in different methods of nebulization. *Bulletin of Experimental Biology and Medicine*, 164(4):576–578, 2018.

[174] Ariel Astudillo, Sharon Shui Yee Leung, Elizabeth Kutter, Sandra Morales, and Hak-Kim Chan. Nebulization effects on structural stability of bacteriophage pev 44. *European Journal of Pharmaceutics and Biopharmaceutics*, 125:124–130, 2018.

[175] Sean Collignon, Ofer Manor, and James Friend. Improving and predicting fluid atomization via hysteresis-free thickness vibration of lithium niobate. *Advanced Functional Materials*, 28(8):1704359, 2018.

[176] Gennady Altshuler and Ofer Manor. Spreading dynamics of a partially wetting water film atop a mhz substrate vibration. *Physics of Fluids*, 27(10):102103, 2015.

[177] A Winkler, S Harazim, DJ Collins, R Brünig, H Schmidt, and SB Menzel. Compact saw aerosol generator. *Biomedical Microdevices*, 19(1):9, 2017.

[178] George Whitesides. The lab finally comes to the chip! *Lab on a Chip*, 14(17):3125–3126, 2014.

[179] Richie J Shilton, Leslie Y Yeo, and James R Friend. Quantification of surface acoustic wave induced chaotic mixing-flows in microfluidic wells. *Sensors and Actuators B: Chemical*, 160(1):1565–1572, 2011.

[180] Ghulam Destgeer, Hyunjun Cho, Byung Hang Ha, Jin Ho Jung, Jinsoo Park, and Hyung Jin Sung. Acoustofluidic particle manipulation inside a sessile droplet: Four distinct regimes of particle concentration. *Lab on a Chip*, 16(4):660–667, 2016.

[181] Naiqing Zhang, Jiyang Mei, Tilvawala Gopesh, and James Friend. Optimized, omnidirectional surface acoustic wave source: 152 degree y-rotated cut of lithium niobate for acoustofluidics. *IEEE Transactions on Ultrasonics, Ferroelectrics, and Frequency Control*, pages 2176–2186, 2020.

[182] AA Doinikov. Acoustic radiation pressure on a rigid sphere in a viscous fluid. *Proceedings of the Royal Society of London. Series A: Mathematical and Physical Sciences*, 447(1931):447–466, 1994.

[183] François Nadal and Eric Lauga. Asymmetric steady streaming as a mechanism for acoustic propulsion of rigid bodies. *Physics of Fluids*, 26(8):082001, 2014.

[184] James P Lata, Feng Guo, Jinshan Guo, Po-Hsun Huang, Jian Yang, and Tony Jun Huang. Surface acoustic waves grant superior spatial control of cells embedded in hydrogel fibers. *Advanced Materials*, 28(39):8632–8638, 2016.

[185] Kejie Chen, Mengxi Wu, Feng Guo, Peng Li, Chung Yu Chan, Zhangming Mao, Sixing Li, Liqiang Ren, Rui Zhang, and Tony Jun Huang. Rapid formation of size-controllable multicellular spheroids via 3d acoustic tweezers. *Lab on a Chip*, 16(14):2636–2643, 2016.

[186] Ofer Manor, Leslie Y. Yeo, and James R. Friend. The appearance of boundary layers and drift flows due to high frequency surface waves. *Journal of Fluid Mechanics*, 707:482–495, 2012.

[187] Jinjie Shi, Daniel Ahmed, Xiaole Mao, Sz-Chin Steven Lin, Aitan Lawit, and Tony Jun Huang. Acoustic tweezers: patterning cells and microparticles using standing surface acoustic waves (ssaw). *Lab on a Chip*, 9(20):2890–2895, 2009.

[188] George M Whitesides and Bartosz Grzybowski. Self-assembly at all scales. *Science*, 295(5564):2418–2421, 2002.

[189] Lin Jiang, Xiaodong Chen, Nan Lu, and Lifeng Chi. Spatially confined assembly of nanoparticles. *Accounts of Chemical Research*, 47(10):3009–3017, 2014.

[190] Erez Braun, Yoav Eichen, Uri Sivan, and Gdalyahu Ben-Yoseph. Dna-templated assembly and electrode attachment of a conducting silver wire. *Nature*, 391(6669):775–778, 1998.

[191] Ken Takazawa, Yasutaka Kitahama, Yasuyuki Kimura, and Giyuu Kido. Optical waveguide self-assembled from organic dye molecules in solution. *Nano Letters*, 5(7):1293–1296, 2005.

[192] Xiyou Li, Louise E Sinks, Boris Rybtchinski, and Michael R Wasielewski. Ultrafast aggregate-to-aggregate energy transfer within self-assembled light-harvesting columns of zinc phthalocyanine tetrakis (perylenediimide). *Journal of the American Chemical Society*, 126(35):10810–10811, 2004.

[193] Nirmalya Chaki and K Vijayamohanan. Self-assembled monolayers as a tunable platform for biosensor applications. *Biosensors and Bioelectronics*, 17(1):1–12, 2002.

[194] Monty Liong, Jie Lu, Michael Kovochich, Tian Xia, Stefan G Ruehm, Nel andre E, Fuyuhiko Tamanoi, and Jeffrey I Zink. Multifunctional inorganic nanoparticles for imaging, targeting and drug delivery. *ACS Nano*, 2(5):889, 2008.

[195] Alexander Edrington, Augustine Urbas, Peter DeRege, Cinti Chen, Timothy Swager, Nikos Hadjichristidis, Maria Xenidou, Lewis Fetters, John Joannopoulos, and Yoel Fink. Polymer-based photonic crystals. *Advanced Materials*, 13(6):421–425, 2001.

[196] Y Sahoo, M Cheon, S Wang, H Luo, EP Furlani, and PN Prasad. Field-directed self-assembly of magnetic nanoparticles. *The Journal of Physical Chemistry B*, 108(11):3380–3383, 2004.

[197] Susumu Soeya, Jun Hayakawa, Hiromasa Takahashi, Kenchi Ito, Chisato Yamamoto, Ayumu Kida, Hidefumi Asano, and Masaaki Matsui. Development of half-metallic ultrathin fe3o4 films for spin-transport devices. *Applied physics letters*, 80(5):823–825, 2002.

[198] David Coey, AE Berkowitz, Ll Balcells, FF Putris, and A Barry. Magnetoresistance of chromium dioxide powder compacts. *Physical Review Letters*, 80(17):3815, 1998.

[199] Shouheng Sun and Hao Zeng. Size-controlled synthesis of magnetite nanoparticles. *Journal of the American Chemical Society*, 124(28):8204–8205, 2002.

[200] Samuel Levine, Bruce D Bowen, and Susan J Partridge. Stabilization of emulsions by fine particles i. partitioning of particles between continuous phase and oil/water interface. *Colloids and Surfaces*, 38(2):325–343, 1989.

[201] CE Bradley. Acoustic streaming field structure: The influence of the radiator. *The Journal of the Acoustical Society of America*, 100(3):1399–1408, 1996.

[202] M Tanase, DM Silevitch, A Hultgren, LA Bauer, PC Searson, GJ Meyer, and DH Reich. Magnetic trapping and self-assembly of multicomponent nanowires. *Journal of Applied Physics*, 91(10):8549–8551, 2002.

[203] Jun Wang, Qianwang Chen, Chuan Zeng, and Binyang Hou. Magnetic-field-induced growth of single-crystalline fe3o4 nanowires. *Advanced Materials*, 16(2):137–140, 2004.

[204] Mingzai Wu, Ying Xiong, Yaoshun Jia, Helin Niu, Haiping Qi, Jing Ye, and Qianwang Chen. Magnetic field-assisted hydrothermal growth of chain-like nanostructure of magnetite. *Chemical Physics Letters*, 401(4):374–379, 2005.

[205] Daen Choi, Se Jang, Hyung Yu, and Seung Yang. Two-dimensional polymer nanopattern by using particle-assisted soft lithography. *Chemistry of Materials*, 16(18):3410–3413, 2004.

[206] Satoru Shoji and Satoshi Kawata. Photofabrication of three-dimensional photonic crystals by multibeam laser interference into a photopolymerizable resin. *Applied Physics Letters*, 76(19):2668–2670, 2000.

[207] Shouhu Xuan, Feng Wang, Josie M. Y. Lai, Kathy W. Y. Sham, Yi-Xiang J. Wang, Siu-Fung Lee, Jimmy C. Yu, Christopher H. K. Cheng, and Ken Cham-Fai Leung. Synthesis of biocompatible, mesoporous fe3o4 nano/microspheres with large surface area for magnetic resonance imaging and therapeutic applications. *ACS Applied Materials & Interfaces*, 3(2):237–244, 2011.

[208] Shuang Zhang, Michelle Regulacio, and Ming Han. Self-assembly of colloidal one-dimensional nanocrystals. *Chemical Society Reviews*, 43(7):2301–2323, 2014.

[209] Shouheng Sun, Simone Anders, Hendrik F Hamann, Jan-U Thiele, JEE Baglin, Thomas Thomson, Eric E Fullerton, CB Murray, and Bruce D Terris. Polymer mediated self-assembly of magnetic nanoparticles. *Journal of the American Chemical Society*, 124(12):2884–2885, 2002.

[210] Helin Niu, Qianwang Chen, Hongfei Zhu, Yushun Lin, and Xing Zhang. Magnetic field-induced growth and self-assembly of cobalt nanocrystallites. *Journal of Materials Chemistry*, 13(7):1803–1805, 2003.

[211] Randall Erb, Hui Son, Bappaditya Samanta, Vincent Rotello, and Benjamin Yellen. Magnetic assembly of colloidal superstructures with multipole symmetry. *Nature*, 457(7232):999–1002, 2009.

[212] A Reenen, A Jong, and M Prins. Transportation, dispersion and ordering of dense colloidal assemblies by magnetic interfacial rotaphoresis. *Lab on a chip*, 15(13):2864–2871, 2015.

[213] Karen Butter, PHH Bomans, PM Frederik, GJ Vroege, and AP Philipse. Direct observation of dipolar chains in iron ferrofluids by cryogenic electron microscopy. *Nature Materials*, 2(2):88–91, 2003.

[214] Srikanth Singamaneni, Valery N Bliznyuk, Christian Binek, and Evgeny Y Tsymbal. Magnetic nanoparticles: recent advances in synthesis, self-assembly and applications. *Journal of Materials Chemistry*, 21(42):16819–16845, 2011.

[215] Sibani Biswal and Alice Gast. Rotational dynamics of semiflexible paramagnetic particle chains. *Physical Review E*, 69(4):041406, 2004.

[216] JK Armstrong, RB Wenby, HJ Meiselman, and TC Fisher. The hydrodynamic radii of macromolecules and their effect on red blood cell aggregation. *Biophysical Journal*, 87(6):4259–4270, 2004.

[217] Jian Li, Qian Du, and Caixin Sun. An improved box-counting method for image fractal dimension estimation. *Pattern Recognition*, 42(11):2460 – 2469, 2009.

[218] Ming K Tan, James R Friend, and Leslie Yeo. Microparticle collection and concentration via a miniature surface acoustic wave device. *Lab on a Chip*, 7(5):618–625, 2007.

[219] Majid Hejazian, Weihua Li, and Nam Nguyen. Lab on a chip for continuous-flow magnetic cell separation. *Lab on a Chip*, 15(4):959–970, 2015.

[220] Ayyoub Mehdizadeh, Renwei Mei, James F Klausner, and Nima Rahmatian. Interaction forces between soft magnetic particles in uniform and non-uniform magnetic fields. *Acta Mechanica Sinica*, 26(6):921–929, 2010.

[221] Myung Kim and Zydney andrew. Effect of electrostatic, hydrodynamic and brownian forces on particle trajectories and sieving in normal flow filtration. *Journal of Colloid and Interface Science*, 269(2):425–431, 2004.

[222] Kristian Berland, Valentino Cooper, Kyuho Lee, Elsebeth Schröder, T Thonhauser, Per Hyldgaard, and Bengt Lundqvist. van der waals forces in density functional theory: a review of the vdw-df method. *Reports on Progress in Physics*, 78(6):066501, 2015.

[223] Peter Kralchevsky and Kuniaki Nagayama. Capillary forces between colloidal particles. *Langmuir*, 10(1):23–36, 1994.

[224] François Nadal and Eric Lauga. Small acoustically forced symmetric bodies in viscous fluids. *The Journal of the Acoustical Society of America*, 139(3):1081–1092, 2016.

[225] Morteza Miansari, Aisha Qi, Leslie Yeo, and James R Friend. Vibration-induced deagglomeration and shear-induced alignment of carbon nanotubes in air. *Advanced Functional Materials*, 25(7):1014–1023, 2015.

[226] Thomas Laurell, Filip Petersson, and Nilsson andreas. Chip integrated strategies for acoustic separation and manipulation of cells and particles. *Chemical Society Reviews*, 36(3):492–506, 2007.

[227] Jacob N Israelachvili. *Intermolecular and surface forces: revised third edition*. Academic Press, 2011.

[228] Bertrand Faure, German Salazar-Alvarez, and Lennart Bergström. Hamaker constants of iron oxide nanoparticles. *Langmuir*, 27(14):8659–8664, 2011.

[229] Hugo Christiaan Hamaker. The london—van der waals attraction between spherical particles. *Physica*, 4(10):1058–1072, 1937.

[230] Hiroyuki Shinto, Daisuke Komiyama, and Ko Higashitani. Lateral capillary forces between solid bodies on liquid surface: a lattice boltzmann study. *Langmuir*, 22(5):2058–2064, 2006.

[231] Peter A Kralchevsky and Nikolai D Denkov. Capillary forces and structuring in layers of colloid particles. *Current Opinion in Colloid and Interface Science*, 6(4):383–401, 2001.

[232] Constantine Balanis. *Advanced engineering electromagnetics*. John Wiley & Sons, 2012.

[233] François Nadal and Eric Lauga. Small acoustically forced symmetric bodies in viscous fluids. *The Journal of the Acoustical Society of America*, 139(3):1081–1092, 2016.

[234] Daniel Reeves and John Weaver. Simulations of magnetic nanoparticle brownian motion. *Journal of Applied Physics*, 112(12):124311, 2012.

[235] Younjin Min, Mustafa Akbulut, Kai Kristiansen, Yuval Golan, and Jacob Israelachvili. The role of interparticle and external forces in nanoparticle assembly. *Nature Materials*, 7(7):527–538, 2008.

[236] Katherine Ferrara, Rachel Pollard, and Mark Borden. Ultrasound microbubble contrast agents: Fundamentals and application to gene and drug delivery. *Annu. Rev. Biomed. Eng.*, 9:415–447, 2007.

[237] E Stride and N Saffari. Microbubble ultrasound contrast agents: a review. *Proceedings of the Institution of Mechanical Engineers, Part H: Journal of Engineering in Medicine*, 217(6):429–447, 2003.

[238] Ashutosh Agarwal, Wun Jern Ng, and Yu Liu. Principle and applications of microbubble and nanobubble technology for water treatment. *Chemosphere*, 84(9):1175–1180, 2011.

[239] Hai-Dong Liang, J Alison Noble, and Peter NT Wells. Recent advances in biomedical ultrasonic imaging techniques. *Interface Focus*, pages 475–476, 2011.

[240] Sofie Snipstad, Einar Sulheim, Catharina de Lange Davies, Chrit Moonen, Gert Storm, Fabian Kiessling, Ruth Schmid, and Twan Lammers. Sonopermeation to improve drug delivery to tumors: from fundamental understanding to clinical translation. *Expert Opinion on Drug Delivery*, (just-accepted), 2018.

[241] Wen Bin Cai, Heng Li Yang, Jian Zhang, Ji Kai Yin, Yi Lin Yang, Li Jun Yuan, Li Zhang, and Yun You Duan. The optimized fabrication of nanobubbles as ultrasound contrast agents for tumor imaging. *Scientific Reports*, 5:13725, 2015.

[242] Tinghui Yin, Ping Wang, Rongqin Zheng, Bowen Zheng, Du Cheng, Xinling Zhang, and Xintao Shuai. Nanobubbles for enhanced ultrasound imaging of tumors. *International Journal of Nanomedicine*, 7:895, 2012.

[243] Nico De Jong, Ayache Bouakaz, and Peter Frinking. Basic acoustic properties of microbubbles. *Echocardiography*, 19(3):229–240, 2002.

[244] Tae-Hong Kim and Ho-Young Kim. Disruptive bubble behaviour leading to microstructure damage in an ultrasonic field. *Journal of Fluid Mechanics*, 750:355–371, 2014.

[245] Mikhail G Shapiro, Patrick W Goodwill, Arkosnato Neogy, Melissa Yin, F Stuart Foster, David V Schaffer, and Steven M Conolly. Biogenic gas nanostructures as ultrasonic molecular reporters. *Nature Nanotechnology*, 9(4):311–316, 2014.

[246] Chi-Ming Yam, Claire-Marie Pradier, Michele Salmain, Philippe Marcus, and Gérard Jaouen. Binding of biotin to gold surfaces functionalized by self-assembled monolayers of cystamine and cysteamine: Combined ft-irras and xps characterization. *Journal of Colloid and Interface Science*, 235(1):183–189, 2001.

[247] George J Lu, Arash Farhadi, Arnab Mukherjee, and Mikhail G Shapiro. Proteins, air and water: reporter genes for ultrasound and magnetic resonance imaging. *Current Opinion in Chemical Biology*, 45:57–63, 2018.

[248] ANTHONY E Walsby. Gas vesicles. *Microbiological Reviews*, 58(1):94–144, 1994.

[249] George J Lu, Arash Farhadi, Jerzy O Szablowski, Audrey Lee-Gosselin, Samuel R Barnes, Anupama Lakshmanan, Raymond W Bourdeau, and Mikhail G Shapiro. Acoustically modulated magnetic resonance imaging of gas-filled protein nanostructures. *Nature Materials*, 17(5):456, 2018.

[250] Arash Farhadi, Gabrielle H Ho, Daniel P Sawyer, Raymond W Bourdeau, and Mikhail G Shapiro. Ultrasound imaging of gene expression in mammalian cells. *bioRxiv*, page 580647, 2019.

[251] Jerzy O Szablowski, Avinoam Bar-Zion, and Mikhail G Shapiro. Achieving spatial and molecular specificity with ultrasound-targeted biomolecular nanotherapeutics. *Accounts of chemical research*, 52(9):2427–2434, 2019.

[252] Raymond W Bourdeau, Audrey Lee-Gosselin, Anupama Lakshmanan, Arash Farhadi, Sripriya Ravindra Kumar, Suchita P Nety, and Mikhail G Shapiro. Acoustic reporter genes for noninvasive imaging of microorganisms in mammalian hosts. *Nature*, 553(7686):86, 2018.

[253] Anupama Lakshmanan, Arash Farhadi, Suchita P Nety, Audrey Lee-Gosselin, Raymond W Bourdeau, David Maresca, and Mikhail G Shapiro. Molecular engineering of acoustic protein nanostructures. *ACS Nano*, 10(8):7314–7322, 2016.

[254] David Maresca, Anupama Lakshmanan, Mohamad Abedi, Avinoam Bar-Zion, Arash Farhadi, George J Lu, Jerzy O Szablowski, Di Wu, Sangjin Yoo, and Mikhail G Shapiro. Biomolecular ultrasound and sonogenetics. *Annual Review of Chemical and Biomolecular Engineering*, 9:229–252, 2018.

[255] William G Pitt, Ghaleb A Husseini, and Bryant J Staples. Ultrasonic drug delivery–a general review. *Expert Opinion on Drug Delivery*, 1(1):37–56, 2004.

[256] Paul A Dayton, Karen E Morgan, Alexander L Klibanov, Gary H Brandenburger, and Kathy W Ferrara. Optical and acoustical observations of the effects of ultrasound on contrast agents. *IEEE Transactions on Ultrasonics, Ferroelectrics, and Frequency Control*, 46(1):220–232, 1999.

[257] Ayache Bouakaz, Michel Versluis, and Nico de Jong. High-speed optical observations of contrast agent destruction. *Ultrasound in Medicine and Biology*, 31(3):391–399, 2005.

[258] Michel Versluis. High-speed imaging in fluids. *Experiments in Fluids*, 54(2):1458, 2013.

[259] Jeroen Sijl, Emmanuel Gaud, Peter JA Frinking, Marcel Arditi, Nico de Jong, Detlef Lohse, and Michel Versluis. Acoustic characterization of single ultrasound contrast agent microbubbles. *The Journal of the Acoustical Society of America*, 124(6):4091–4097, 2008.

[260] TG Leighton, DG Ramble, AD Phelps, CL Morfey, and PP Harris. Acoustic detection of gas bubbles in a pipe. *Acta Acustica United with Acustica*, 84(5):801–814, 1998.

[261] Daisuke Koyama, Hironori Kotera, Natsuko Kitazawa, Kenji Yoshida, Kentaro Nakamura, and Yoshiaki Watanabe. Vibration of a single microcapsule with a hard plastic shell in an acoustic standing wave field. *IEEE Transactions on Ultrasonics, Ferroelectrics, and Frequency Control*, 58(4):737–743, 2011.

[262] Hironori Kotera, Daisuke Koyama, Natsuko Kitazawa, Kenji Yoshida, Kentaro Nakamura, and Yoshiaki Watanabe. A simultaneous observation system for microbubble vibration in an acoustic field by using a high-speed camera and an ldv. *Proc. ICA 2010*, page 23, 2010.

[263] David Maresca, Anupama Lakshmanan, Audrey Lee-Gosselin, Johan M Melis, Yu-Li Ni, Raymond W Bourdeau, Dennis M Kochmann, and Mikhail G Shapiro. Nonlinear ultrasound imaging of nanoscale acoustic biomolecules. *Applied Physics Letters*, 110(7):073704, 2017.

[264] Anupama Lakshmanan, George J Lu, Arash Farhadi, Suchita P Nety, Martin Kunth, Audrey Lee-Gosselin, David Maresca, Raymond W Bourdeau, Melissa Yin, and Judy Yan. Preparation of biogenic gas vesicle nanostructures for use as contrast agents for ultrasound and mri. *Nature protocols*, 12(10):2050–2080, 2017.

[265] Emmanuel Cherin, Johan M Melis, Raymond W Bourdeau, Melissa Yin, Dennis M Kochmann, F Stuart Foster, and Mikhail G Shapiro. Acoustic behavior of halobacterium salinarum gas vesicles in the high-frequency range: experiments and modeling. *Ultrasound in Medicine and Biology*, 43(5):1016–1030, 2017.

[266] Philippe Marmottant, Sander van der Meer, Marcia Emmer, Michel Versluis, Nico de Jong, Sascha Hilgenfeldt, and Detlef Lohse. A model for large amplitude oscillations of coated bubbles accounting for buckling and rupture. *The Journal of the Acoustical Society of America*, 118(6):3499–3505, 2005.

[267] PC Weber, DH Ohlendorf, JJ Wendoloski, and FR Salemme. Structural origins of high-affinity biotin binding to streptavidin. *Science*, 243(4887):85–88, 1989.

[268] H Medwin. Counting bubbles acoustically: a review. *Ultrasonics*, 15(1):7–13, 1977.

[269] John E Sader, Morteza Yousefi, and James R Friend. Uncertainty in least-squares fits to the thermal noise spectra of nanomechanical resonators with applications to the atomic force microscope. *Review of Scientific Instruments*, 85(2):025104, 2014.

[270] Charles Devin Jr. Survey of thermal, radiation, and viscous damping of pulsating air bubbles in water. *The Journal of the Acoustical Society of America*, 31(12):1654–1667, 1959.

[271] J Gregory McDaniel, Iskander Akhatov, and R Glynn Holt. Inviscid dynamics of a wet foam drop with monodisperse bubble size distribution. *Physics of Fluids*, 14(6):1886–1894, 2002.

[272] Milton S Plesset and Andrea Prosperetti. Bubble dynamics and cavitation. *Annual Review of Fluid Mechanics*, 9(1):145–185, 1977.

[273] Lord Rayleigh. Viii. on the pressure developed in a liquid during the collapse of a spherical cavity. *The London, Edinburgh, and Dublin Philosophical Magazine and Journal of Science*, 34(200):94–98, 1917.

[274] Philippe Marmottant, Ayache Bouakaz, Nico de Jong, and Catherine Quilliet. Buckling resistance of solid shell bubbles under ultrasound. *The Journal of the Acoustical Society of America*, 129(3):1231–1239, 2011.